Shedding light on living cells and mineralised tissues using Raman spectroscopy

By

Kristy Lee Cloyd

A thesis submitted to Imperial College London

For the award of PhD and the

Diploma of Imperial College

Department of Materials

Imperial College London

September 2013

London, England

Declaration of Originality

This thesis is submitted for the degree of Doctor of Philosophy at Imperial College London. It describes research carried out in the Department of Materials, Institute of Bioengineering and Department of Bioengineering between October 2008 and September 2013 under the supervision of Professor Molly M. Stevens. Except where appropriately referenced, this work is original and has not been the result of collaboration. No part of this work has been submitted for any other degree, diploma or any other qualification. It does not exceed 60,000 words in length.

Copyright Declaration

Abstract

Raman micro-spectroscopy presents a highly sensitive, non-invasive, and rapid way to collect biochemical information from cells and tissues. The resulting Raman spectrum is a chemical 'fingerprint' containing a wealth of molecular level information which has been used to characterize, monitor, compare and confirm biological processes from the cellular to tissue levels. The work presented in this thesis utilizes Raman spectroscopy to test live *in vitro* cellular models, classify human tissues of interest, and determine the biomolecular differences in tissue samples which are diseased or undergoing therapeutic treatment. Additionally new ways of visualizing and interpreting multivariate analytical results are proposed and demonstrated to ease the determination of the biomolecular features which are most important when comparing sample groups.

A persistent challenge in the interpretation of information rich biological Raman spectra includes the multitude of signals from lipids, proteins, carbohydrates, nucleic acids, and minerals found in a limited spectral range and in some instances overlapping significantly. Partial Least Squares – Discriminant Analysis (PLS-DA) Variable Importance Projection (VIP) scores were presented as heat maps overlaying difference spectra to ease the visualization of significant biochemical bond changes between sample groups and their trends. The advantages of applying PLS-DA VIP scores in this way are demonstrated in well studied and known system including a cultured cellular model incorporating fixation methods and a human tissue comparison between healthy and osteoporotic bone. PLS-DA VIP score plots were additionally utilized to characterize and compare the biolomecular environments surrounding the recently described microscopic mineral inclusions in human aortic valves and aortae. The PLS-DA VIP score plots exposed the chemical differences in these systems through highlighting the corresponding spectral bands in an easy to read and interpret way.

Raman micro-spectroscopy was also applied to investigate an *in vitro* 'calcified' porcine aortic valvular interstitial cell model. This model system was probed for the first time using the combination of Raman micro-spectroscopy and complimentary gold standard biological techniques to determine the protein and potential mineral content within these nodular, cellular systems. The 'calcified' porcine aortic valvular

cell nodules showed no evidence of mineral inclusion. These nodules did exhibit a heavy extracellular matrix production including the production of collagen I.
The porcine aortic valvular cell nodules acting as a model system for diseased aortic valve tissue requires not only the characterization of the cell nodule *in vitro* but also the characterization of the human disease spectrum which the model is suggested to replicate. The discovery and characterisation of microscopic mineral spherical inclusions (50nm-200μm) located in both valvular and vascular tissues leads to an interesting question on the introduction and role of microscopic mineral deposits in cardiovascular disease. Here Raman micro-spectroscopy was utilized to investigate the organic matrix surrounding these microscopic mineral deposits to determine if any colocalised protein changes exist. Protein and specifically collagen changes are demonstrated between tissues with and without the spherical mineral deposits despite being macroscopically indistinguishable.

Raman spectroscopy was also utilized to provide direct insights into tissue constituent and structural changes on the molecular level in heat-induced tissue fusion via radio-frequency (RF) energy. This type of tissue fusion has gained wide acceptance clinically and is presented here as the first optical-Raman-spectroscopy study on tissue fusion samples *in vitro*. This study exposed spectroscopic evidence for the loss of distinct collagen fibres rich tissue layers as well as the denaturing and restructuring of collagen crosslinks post RF fusion.

Raman spectroscopy is a demonstrated, powerful, biomolecular imaging technique which benefits from advancements in mathematical analytical techniques as well as its own application in biological investigations. This thesis explores the application of Raman spectroscopy in combination with powerful analytical techniques to further characterize and compare biological systems of interest.

Preface

Some of the work presented in this thesis has been published and presented in various conferences and journal articles or is being prepared for publication. In each chapter any collaborator's contributions will be fully disclosed in the methods and materials sections where appropriate.

Journal publications

Cloyd KL, El-Hamamsy I, Boonrungsiman S, Hedegaard MAB, Gentleman E, Sarathchandra P, Colazzo F, Gentleman MM, Yacoub MH, Chester AH, Stevens MM. Characterization of Porcine Aortic Valvular Interstitial Cell 'Calcified' Nodules. PLoS ONE. 2012;7:e48154.

Bertazzo S, Gentleman E, Cloyd KL, Yacoub MH, Chester AH, Stevens MM. Nano-analytical electron microscopy reveals fundamental insights into human cardiovascular tissue calcification. NATURE MATERIALS. 2013;12:576-83.

Su L*, Cloyd KL*, Shobhit A, Hedegaard MAB, Steele J, Elson DS, Stevens MM, Hanna GB. Raman Spectroscopic Evidences of Tissue Restructuring in Heat-Induced Tissue Fusion. Journal of BIOPHOTONICS, *co-first author

Articles submitted or in preparation

Cloyd KL, Bertazzo S, Hedegaard MAB, Yacoub MH, Chester AH, Stevens MM. Biomolecular environments surrounding microscopic cardiovascular calcification. *in preparation.*

Hedegaard MAB, Cloyd KL, Horejs CM, Stevens MM. Improving spectral interpretation of differences in Raman spectra of Cells and Tissue Using PLS-DA VIP scores. *submitted.*

Conference contributions

Oral Presentations:
- SPEC 2010 - Jun. 2010
- 2010 Biomedical Engineering Society Annual Meeting - Oct. 2010
- Renishaw's Inside Raman Seminar programme - Sept. 2011
- British Heart Foundation Research Excellence Symposium - Oct. 2011
2x Oral - SPIE Biophotonics West 2012 -Jan. 2012
- British Heart Foundation Research Excellence Symposium - Oct. 2012
- 4th Biennial Heart Valve Biology and Tissue Engineering Meeting - Mar. 2010

Poster Presentations:
- 10th Inter. Conference - Chemistry & Biology of Mineralized Tissues - Nov. 2010
- Imperial College Department of Materials Postgraduate Research Day - Mar. 2011
- UKGSEPS Research Students' Research Symposium 2011 - Jul. 2011
- Young Researchers Meeting IChemE BESG, ESACT-UK -Sept. 2011
- FT-IR Spectroscopy in Microbiological and Medical Diagnostics - Oct. 2011
- Rosetrees Trust Symposium, Focus on Medical Research - Oct. 2012

Acknowledgements

First and foremost I want to thank my parents, John David and Hsiu Hua Lee Cloyd for their love and support during the pursuit of this PhD.

I would like to thank the British Heart Foundation and the Whitaker International Fellowship program for their generous funding and access to a range of resources.

Professor Molly M. Stevens has been an exceptional supervisor and mentor. Additionally Professor Stevens has assembled and cultured an incredible research team with a contagious passion for science and limitless talent. It has been a privilege to work with Professor Stevens and the Stevens' group and I look forward to their future discoveries and innovations. I would especially like to thank Dr. Eileen Gentleman, Dr. Gavin Jell, Dr. Sergio Bertazzo, and Dr. Martin Hedegaard. Also I am thankful to my wonderful collaborators including Dr. Lei Su and Professor Molly Gentleman.

I would like to thank my co-supervisor Dr. Adrian Chester and Professor Magdi Yacoub and Dr. Ismail El-Hamamsy for sharing their expertise, ideas and scientific insights.

I am very grateful to Professor D. L. Hawkins Jr., Professor C.J. Chuong, Professor L. Tang, and Professor R. C. Eberhart for their wonderful guidance during my undergraduate and master's degree programs.

I would also like to thank Dr. Jonnathan Warwick and the Warwick family for their love and support.

There remains a long list of people and organizations which have inspired, supported and propelled me during these past four years. A flood of names come to mind and I am eternally grateful and fortunate to have been surrounded by so many incredible individuals. I look forward to working with all these exceptional people in the years to come and am confident I will be saying 'thank you' in person.

Table of Contents

List of Figures

List of Tables

Acronyms and Symbols

ARS	Alizarin Red S
αSMA	smooth muscle alpha actin
aVICs	activated valvular interstitial cells
BGLAP	bone gamma-carboxyglutamate protein
BP	burst pressure
BSA	bovine serum albumin
Ca	Calcium
C-C	Carbon Carbon single bond
CCD	charged coupled device
C	Carbon
cm	centimeter
COL1A1	type 1 collagen
CP	compression pressure
Ct	cycle threshold
CTL	basal
DAPI	4',6-diamidino-2-phenylindole
dH_2O	distilled water
DMEM	Dulbecco's Modified Eagles Medium
DNA	Deoxyribonucleic acid
E	Energy (state, level)
E_a	Energy state before an incident
E_b	Energy state after an incident
ECM	extracellular matrix
EDS / EDX	energy-dispersive X-ray spectroscopy
EMSC	extended multiplicative scatter correction
eVICs	embryonic progenitor cells
FA	formaldehyde
FBS	fetal bovine serum
FWHM	full width half maximum
H&E	haematoxylin and eosin
HeLa	cell line derived from cervical cancer cells originally isolated in 1951
HNF	holographic notch filter
iPLS-DA	interval Partial Least Squares Discriminant Analysis

kHz	kilohertz
LDA	Linear Discriminant Analysis
LV1/2/3	Latent Variable
Mg	Milligram
Mm	Millimeter
mmHg	Millimeter of mercury
mmol	millimole
MMPa	matrix metalloproteinases
MOBs	mineralizing murine calvarial osteoblasts
MPa	megapascal
mW	milli-Watts
n	number of
NA	numerical aperture
N-FINDR	automated end-member detection and un-mixing algorithm
nm	nanometers
obVICs	Osteoblastic valvular interstitial cells
OCT	optimal cutting temperature
OST	osteogenic
PAVIC	porcine aortic valvular interstitial cell
PBS	phosphate buffered saline
PC	principal component
PC	personal computer
PCA	principal component analysis
PCR	polymerase chain reaction
Phe	phenylalanine
PLS	Partial Least Squares
PLS-DA	Partial Least Squares Discriminant Analysis
Pro	In favor of
p-values	likelihood of random inspiration for the resulting events
pVICs	circulating endothelial cell precursors
qVICs	quiescent valvular interstitial cells
RF	radio-frequency
RNA	ribonucleic acid
RT	reverse transcription
RT-PCR	reverse transcription polymerase chain reaction
SEM	scanning electron microscopy

SMA	smooth muscle actin
SNR	signal to noise ratio
TEM	transmission electron microscopy
TGF-β1	transforming growth factor beta 1
Trp	tryptophan
Tyr	tyrosine
VICs	valvular interstitial cells
VIP	variable importance projection
v/v	volume per volume
w/v	weight per volume
µm	micron

1 Introduction

Medical science research continues to strive to understand, unravel, alter, mimic, utilize, replicate, control, repair, and/or completely replace biological systems of interest. For these complex investigations a wide variety of techniques have been developed and applied to explore these intricate systems, each with its advantages and disadvantages. From the atomic to the tissue level, each contributing viewpoint is aiding our understanding of biological systems.

1.1.1 Aims

The focus of this thesis is to interrogate biological systems of interest at the molecular level to furnish new information on these systems. This effort incorporates utilizing Raman micro-spectroscopy and complimentary techniques to unearth bio-molecular information from relevant samples as well as exploring analytical tools to aid the biological interpretation of such data. The exploration and demonstration of analytical tools which both takes advantage of sophisticated statistical techniques yet allows for an 'easy to read' visualization of spectral ranges of interest is one of the aims in this thesis. For this purpose Partial Least Squares – Discriminant Analysis (PLS-DA) Variable Importance Projection (VIP) score plots were presented as heat maps overlaying difference spectra distinguishing spectral ranges of interest. These spectral ranges can then be further investigated to help determine the molecular changes distinguishing sample groups. These PLS-DA VIP plots were incorporated in several studies in this thesis to demonstrate the potential for this technique and to utilize this tool for studies at the cellular and tissue level.

A central aim in this work includes the interrogation of cardiovascular calcification with some focus on aortic valve calcification. Here an *in vitro* 'calcified' porcine aortic valvular interstitial cell system was probed to determine the presence (if any) of the calcified content, the nature of this calcification and further expose the molecular components of the nodules this cellular system forms.

Human cardiovascular tissue was also examined in a variety of states along the calcification spectrum to explore the molecular differences between tissues with and without calcification present. Following the discovery and characterization of microscopic spherical mineral inclusions located in both valvular and vascular tissues

we aimed to determine if any changes in the organic matrix surrounding these microscopic mineral inclusions were occurring and if so aimed to identify some of these changes.

Finally heat induced tissue fusion via radio-frequency energy for use in surgical procedures was investigated to determine the changes within the molecular constituents of fused tissue which provide the strong seal associated with this technique. Specifically the molecular bond changes which occur during tissue fusion were of interest in hopes to further characterize the changes in fused tissue as well as identify, if possible, any changes associated with the tissue fusion.

This introduction chapter details the fundamentals of Raman spectroscopy, its incorporation into the study of the biological systems and the analytical techniques applied in this thesis. Additionally presented is an introduction into cardiovascular calcification, and specifically aortic valve calcification, as cardiovascular pathology was a central focus for chapters 3 and 4.

1.2 Raman Spectroscopy

1.2.1 Characteristics of the Raman Process

Vibrational Raman spectroscopy is an optical scattering process based on the interaction of light and matter as first experimentally discovered and described by C.V. Raman in 1928 [1]. Motivated by Arthur Compton's observation that X-rays could lose energy when scattered in-elastically by electrons (also known as the 'Compton effect'), Raman and Krishnan hypothesized that a similar energy transfer should take place when 'normal' light is scattered by atoms or molecules. The experimental evidence and discovery of this effect that bears his name along with his research on the diffusion of gases won Sir C.V. Raman the noble prize in physics in 1930 [2].

When a beam of monochromatic light (e.g. a laser beam) illuminates a substance the majority of this light is transmitted, some is absorbed and a small percentage is scattered. An isolated atom scatters light due to the electric field of the incident light forcing the electrons in the atom to oscillate back and forth about their equilibrium position. The laws of electromagnetism then state when a charge changes its velocity it emits radiation and this emission is uniform in all directions in the plane perpendicular to the oscillation with a decreasing amplitude as the viewing angle

shifts away from the oscillation plane. Of this scattered light the majority is Rayleigh scattering (also known as elastic scattering) meaning the photons experience a directional change only and are essentially of the same frequency. Inelastic scattering occurs when the light emitted not only changes direction but also wavelength and is called Raman scattering.

Moving to polyatomic systems, the vibrational scattering process is often described as a two-photon process where the illuminated molecule goes through a process from an initial quantum state to an intermediate 'virtual' state and lastly to a final quantum state and emits a photon. The virtual state is not a stable, stationary energy state of the molecule but rather a distortion of the electron distribution of the chemical bond. Due to the instability of the virtual state the molecule immediately relaxes back to an electronic state by emitting a photon. For the majority of these interactions the molecule relaxes back to its initial quantum state and the emitted photon is equivalent in energy to the incident photon. This elastic interaction is again called Rayleigh scattering. For a minority of these interactions an energy transfer occurs and some of incident light energy is transferred to the molecule (or vice versa) during the electronic oscillation process. This means the emitted photon is now of a shifted energy level and the amount of the energy transferred corresponds to the specific vibrational energy of the chemical bonds in the molecule. In summary, in this two photon process, if the molecule excited did not gain or lose energy Rayleigh scattering occurred. If the molecule gained or lost energy, Raman scattering occurred. If the molecule gained energy Stokes Raman scattering occurred and if the molecule lost energy, anti-Stokes Raman scatter occurred. These processes are shown below, where E_a is the energy level of the molecular bond before the interaction with the incident photon and E_b is the energy level of the bond after the secondary photon is emitted. This effect is often summarized using energy level diagrams as displayed in Figure 1-1.

The energy of a photon is expressed as $E = hv$, where E is the energy of a photon, h is planck's constant and v is the frequency of the radiation.

$E_a = E_b \rightarrow$ Rayleigh scattering

(excitation: $\Delta E_i = hv_o$ relaxation: $\Delta E_f = -hv_o$)

$E_a < E_b \rightarrow$ Stokes Raman scattering

(excitation: $\Delta E_i = hv_o$ relaxation: $\Delta E_f = -h(v_o - v_v)$ scattered energy: $\Delta E_v = hv_v$)

$E_a > E_b \rightarrow$ Anti-Stokes Raman scattering

(excitation: $\Delta E_i = h\nu_o$ relaxation: $\Delta E_f = -h(\nu_o + \nu_v)$ scattered energy: $\Delta E_v = h\nu_v$)

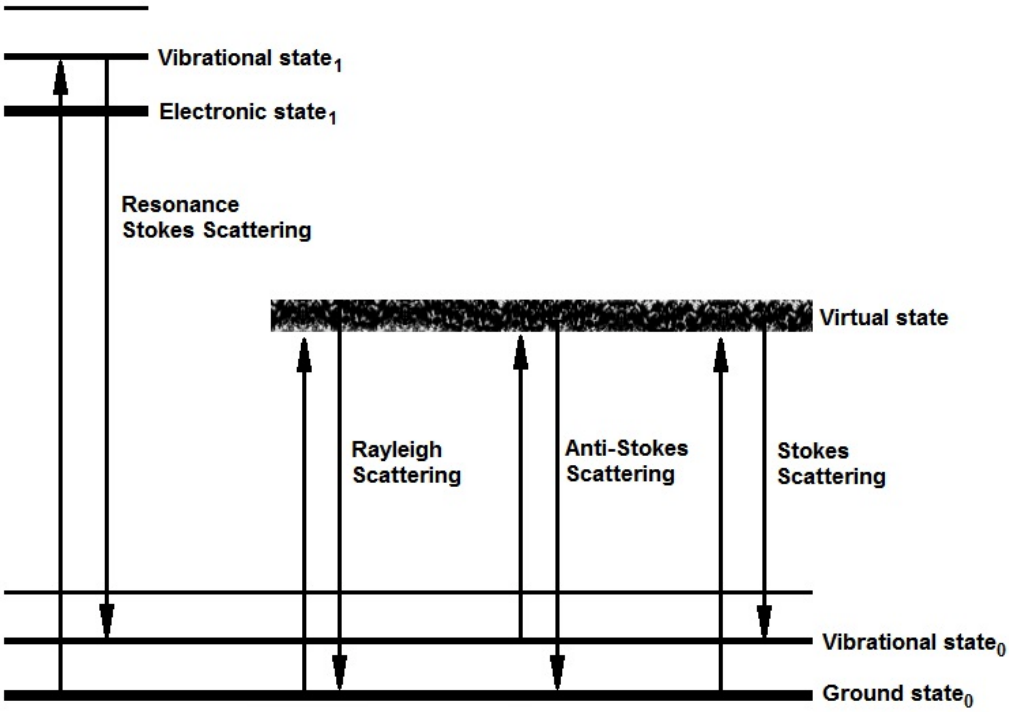

Figure 1-1 Energy level diagram showing Rayleigh, Stokes, and anti-Stokes Raman scattering. The arrows represent the shift in energy levels during excitation (arrows pointing upward) to relaxation and emission of the secondary photon (downward pointing arrow).

Raman inactive or forbidden molecular vibrations will not generate Raman scattering. Molecular vibrations which do generate Raman scattering are called Raman active or allowed and require a change in the polarizability of the stimulated bond during a vibration. Generally speaking, when the excitation of the molecular vibration produces a change in the polarizability of the electron cloud of the molecule, this vibration will be Raman active. When looking at poly atomic systems the total number of vibrational modes found in a poly atomic molecular systems of 'N' atoms is equal to 3N-1.

The work presented in this thesis is based on observations of Stokes Raman scattering and specifically non-resonance Stokes Raman scattering. The distinction being the excitation energy used in these investigations were typically much smaller than the energy of the first electronic state of the molecule thus the molecule has not jumped electronic states due to its interaction with the incident photon (shown in the left most example of Figure 1-1). For resonance stokes scattering the intensity of the

Raman scatter light may be much larger however the selection rules are different. Although this is a very interesting tool and area of research, it is outside the scope of this work.

Raman micro-spectroscopy was utilized in the following chapters to investigate polyatomic molecular systems, where each bond is characterized as a band of frequencies due to the variable modes of oscillation caused by the influence of the surrounding environment on the bond's energy absorption. Raman spectra are shown as a plot of scattered intensity (arbitrary units often abbreviated as 'arb units') as a function of the energy difference between the incident and scattered photons (often shown in this thesis as 'Raman Shift (cm^{-1})'). Frequencies contributed from the multiple bonds within the samples construct the vibrational spectrum presenting a chemical fingerprint of the sample. With micro-spectroscopy the composition was characterized under a microscopic sampling region through a microscope objective in a system described further in this chapter [3].

Specifically the work in this thesis utilizes spontaneous, non-resonate, CCD-based, dispersive Raman micro-spectroscopy. This form of Raman spectroscopy benefits from using relatively inexpensive excitation lasers, compactness, robustness, mobility and a lower technical complexity. There are many other forms of Raman spectroscopy which are briefly described here however are not further detailed as they are independently large areas of research and outside the scope of this work. Resonance Raman scattering (RRS) gives a greater specificity than normal spontaneous Raman scattering however as visible or ultraviolet excitation is required to achieve resonance, the fluorescence interference and spectral degradation of the same hinders RRS in biological studies [4]. Surface-enhanced Raman spectroscopy (SERS) demonstrates an increase in the Raman scattering cross section by the presence of metal colloids (often Au, Ag, or Cu) or a roughened metal surface. The chemical and electromagnetic effects contributing to SERS is not yet fully understood and the inclusion metal colloids or a roughened surface makes it an invasive or contact technique [5,6]. Coherent anti-Stokes Raman scattering (CARS) is a nonlinear optical process using multiple lasers to excite scattering from higher order vibrational modes and produces a significant signal enhancement. The limitation of CARS includes a much increased technical complexity and a somewhat limited spectral and chemical resolution [7,8]. FT-Raman spectroscopy provides a Fourier transform of the time-domain interferogram to produce a frequency-domain Raman spectrum and

ultimately provides signal enhancement through suppression of any fluorescence background encountered with visible wavelength excitation. The limitations of FT-Raman include a typically longer collection time which greatly affects live cell or tissue studies. The advantages and disadvantages of these systems are evolving with technological and analytical developments which are not discussed further in this text; however advancements in each separate family of Raman spectroscopy may translate into the type of Raman spectroscopy utilized here and vice versa.

1.2.2 Raman Spectroscopy of Biological Samples

Raman spectroscopy is applicable for hydrated samples as (polar) water molecules scatter Raman signals weakly, thereby making it useful for gaining bio-molecular insight into cellular systems. Additionally the Raman spectral peaks are sharp and relatively distinct for several bonds of interest in cellular, extracellular matrix (ECM), and mineral environments. The Raman spectra are so intensely information rich that it is also difficult to differentiate each component fully due to overlapping vibrations. Thus the band assignments of individual vibrations must be done with great care. The use of peak assignment tables consisting of the most common and well defined vibrations in biological Raman spectra is essential. Looking further than individual band assignments, the focus of the following investigations were not of one particular molecule but rather an entire cell or tissue region and thus a collection of changes in the Raman spectra were of interest and the trends in these changes. This leads to the use of multivariate statistics which takes into consideration multiple bands and their discrepancies. This is described in more detail below in the Data Collection and Analysis section and in chapter 2.

Raman spectroscopy is extremely versatile in nature and this enables it to be used in a variety of configurations, ranging from fiber optical probes to microscope-based measurements**.** This allows the user to tailor measurement collection parameters to the constraints of each system of interest. Examples include *in vitro* studies of cell culture systems to *in vivo* studies using high throughput fiber optic probes to capture a wealth of biomolecular information rapidly [9-18]. The main system used in this thesis is fully described in this chapter and its configuration remained relatively conserved for more accurate cross comparisons of spectra collected. Each modification to the Raman system may introduce spectral changes that may be adjusted for in spectral pre-processing (described further in this chapter). For the investigations presented in this thesis the Raman spectroscopy instrumental system

was only maintained and not modified during the course of a study, any alterations to the instrument occurred in-between studies as necessary.

1.2.3 Raman Spectroscopy of Soft Tissues

Raman spectroscopy and in particular micro-Raman spectroscopy has been applied to multiple biological investigations ranging from single cells to whole tissue mapping and found significant importance in the fields of medicine, pharmacology and biology. There are several novel biomedical applications of optical spectroscopy, such as fluorescence, reflectance and Raman spectroscopy with Raman spectroscopy providing the most detailed information about the chemical composition of the tissue under study [19,20]. Since progression of diseases are accompanied by a chemical change, Raman spectroscopy has been found valuable in providing information on low level biochemical changes that occur at the cellular or extracellular level including detailed information on proteins, DNA, and lipids.

In 1970 Lord and Yu reported one of the first structurally interpretable laser excited Raman spectrum of a native protein, specifically from a lysosome[21]. Numerous studies have taken advantage of laser excitement and biological compatibility of Raman spectroscopy showcasing it's ability for not only protein but also phospholipids [22] and DNA [23] investigations. Through these studies a large database of molecular fingerprint spectral assignments has accumulated and the reader is referred to Movasaghi et al.'s summary of the most widely used peak frequencies and their assignments [24]. In the following chapters the Raman peaks of interest to that particular study will be introduced and defined including the peak's assignments details within each chapter. A list of Raman spectroscopic peaks used to identify various tissue environments in this thesis can be found in appendix A along with some references reporting those peak assignments. There have been many studies establishing and utilizing the peaks listed in appendix A and the references are some of and not all of the studies which have been used to support them.

1.2.4 Raman Spectroscopy of Mineralized Tissues

Raman spectroscopy has been used to investigate the formation and mineralization of bone nodules *in vitro* previously and has distinct spectral regions correlating to both the organic and inorganic components of bone tissue as shown in Figure 1-2. It is has evolved into a powerful tool for analyzing the inorganic mineral structures in biological tissues due to the high sensitivity to changes in the crystallinity and

molecular substitution of biological apatite [12,25-28]. The spectral bands predominantly used in the investigation of mineralization in this thesis are shown in Table 1-1 with their corresponding bond assignments and Raman peak intensity as described.

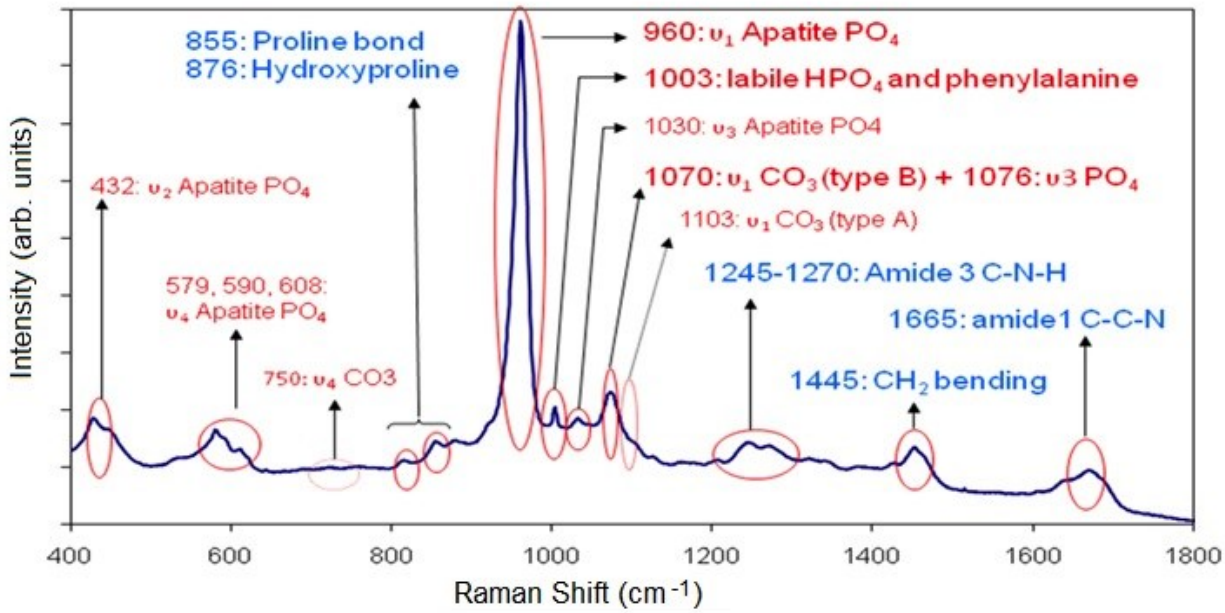

Figure 1-2 Raman spectrum collected from a bone sample with inorganic (mineral) peaks labeled in red and organic (protein) peaks labeled in blue. Some information reproduced from [29].

Table 1-1 Bone mineral and protein Raman spectral peaks and/or bands and assignments. Some information reproduced from [25,29,30]

Band (cm^{-1})	Assignment (bond) [Raman peak intensity]
957 – 962	PO_4^{3-} ν_1 (P-O symmetric stretch) [**VS**]
1065 - 1072	CO_3^{2-} ν_1 (C-O in plane stretch) [**M**]
1243 - 1269	Amide III (C-N-H stretch, C=O stretch) [**M**]
1447 – 1452	CH_2 Wag [**M**]
1595 – 1720	Amide I (C-C-N stretch) [**M**]
[Raman peak intensity]: VS – *very strong,* **M** – *medium,* **W** – *weak*	

These bands have been previously used to investigate the molecular content in bone and revealed information on the crystallinity (related to the full width half maximum (FWHM) of apatite phosphate peak), type-B carbonate substitution (ratio of type-B carbonate area/ apatite phosphate area), and degree of mineralization of the collagen matrix (ratio of apatite phosphate peak area to amide I area) in mineralized studies [28,31,32]. Due to the overlapping peaks and the parameter preferences of various research groups the assignment and measurement of mineral components such as carbonate is not always agreed upon. The methods used in this thesis are detailed in each chapter and when possible are performed in the manner which provided a close approximation to known weight contributions in samples. An example is the approximation of carbonate and a study by Awonusi et al. who compared a series of apatites with known varying carbonate levels to the Raman spectra and univariate analysis of those samples [33].

In addition to the information gained from the univariate analysis of Raman spectral bands and peaks of interest, multivariate analysis is available to determine the main components contributing to the differences between each experimental groups [12]. The multivariate statistical techniques used in this thesis are described in detail later in this chapter.

1.2.5 Raman Spectroscopy System Used

A Raman spectrometer allows for the observation of Raman scattered light. The key components of a Raman spectrometer include an excitation source, sampling

apparatus, filter(s) to reject elastically scattered light, a dispersion element and a detector. The Raman system used predominately in the following chapters was a modified Renishaw InVia system (Renishaw, U.K.). A schematic of this system is presented in Figure 1-3.

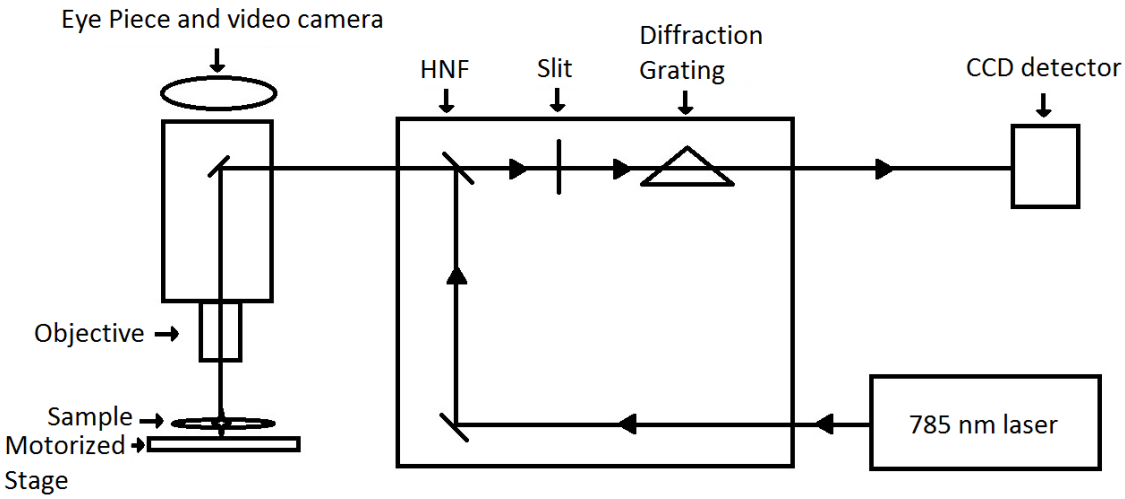

Figure 1-3 Schematic diagram of the modified Renishaw InVia, CCD-based Raman micro-spectroscopy system used in this thesis with the main system components as labeled.

The excitation source was a Renishaw 785 nm (near infrared) diode line focus laser (Renishaw, U.K.) with a ~300 mW power and approximately ~120mW power at the sample. For sampling microscopic regions of interest, the spectrometer was connected to a Leica DM-LM (Leica, Germany) microscope fitted with a heated motorized stage (Prior Scientific, U.K.). Various objectives were used for different applications and specifics on the types of objects will detail in the individual chapters. The collection optics includes a holographic notch filter (HNF) which is a laser rejection filter used to filter out Rayleigh scatter light. The remaining predominately Raman scattered light is then passed focused through a 50μm spectrometer entrance slit to a diffraction grating (1200 lines/mm). This light is then detected by a multichannel (e.g. 1040 x 256 pixels) thermo-electrically (Peltier cooled to -70°C), deep depletion, charged coupled device (CCD). The detected photons are then displayed as a spectrum on the integrated computer as (arbitrary) counts plotted against their shift from the incident irradiation (thus the Raman shift).

1.3 Data Collection and Analysis

For each investigation minor modification to the system may have been incorporated and will be described in the methods section of that chapter. All experiments were performed on an anti-vibrational optics table in a cool, dark, access limited room.

Prior to data collection the wavelength axis was calibrated to the strong and sharp silicon peak at 520.5 cm^{-1} using a sample supplied by Renishaw.

Raman spectroscopy measurement factors which were considered in every investigation were the Raman shift range, energy and power of the incident beam, signal integration time per accumulation and the number of accumulations per spectrum. Typically Raman spectra were collected over the biological finger print region (~500 cm^{-1} – 1900 cm^{-1}). In hydrated samples and living cells in culture, typically the maximum laser power was utilized (~300 mW at source, ~120 at sample) as near infrared radiation at this wavelength (785 nm), power and beam geometry (line laser with elliptical focal spot size ~10 x 20 x 40 μm axial resolution, depending on the objective used) have been previously shown to not disrupt the sample and produce information rich spectra. With dehydrated samples a power reduction was sometimes applied to reduce any risk of burning. Signal integration time per accumulation and the number of accumulations per collected spectrum depended greatly on the experimental conditions and samples. With each biological sample particular constraints were considered (temporal, spatial, thermal, and sensitivity considerations) to ensure a non-invasive invigoration of the sample while yielding a high enough signal to noise Raman spectrum for data analysis. Details of the selected measurement parameters are found in each chapter.

1.3.1 Chemometrics

Each collected Raman spectrum is a signature containing chemical signatures describing the normal vibrational molecular modes within the sampled region. Translation of the collected Raman spectra into chemical information and further to biologically relevant chemical information requires multiples stages of analysis. The analytical process includes signal processing (synonymous with preprocessing), the comparison of specific peaks (univariate analysis), and the semi-quantitative and qualitative multivariate analysis of more than one peak of interest (and often the entire spectrum). The high dimension and complexity of the Raman spectral dataset

collected in biological investigations requires a diverse range of high power analytical techniques to enable identification of key trends. The preprocessing is often required to ensure robust and reliable multivariate analysis by removing unwanted parts of the signal (noise, background, cosmic rays, etc.) and to correct spectra for instrumental or experimental errors. Thus the combination of preprocessing methods may differ in each investigation as do the univariate and multivariate analysis. Within each study however the preprocessing methods are held constant as to generate a standardized data set in which the individual spectra are then directly comparable.

In each of the following chapters the preprocessing and applied analytical technics are further specified. For the preprocessing of the Raman spectra however the following techniques were often utilized and are described further here.

1.3.2 Baseline and Background Correction

Background correction greatly improves the qualitative interpretation of spectral data through the removal of Raman spectral features what are not informative on the sample of interest. These spectral features are often appear from the luminescence process (such as fluorescence), contamination light (e.g. sunlight, monitors, blackbody radiation, chemiluminescence), and/or the Raman scattering from the laser lights interaction with substrates, optics, and/or impurities within the sample. All background subtracted implemented in this thesis is automated rather than using user-defined curves.

The predominant background and baseline correction techniques utilized include application of a Savitsky-Golay filter to compute 2^{nd} derivative Raman spectra [34], polynomial baseline correction, and extended multiplicative scatter correction (EMSC). The polynomial baseline correction was based on a modpoly algorithm described by Lieber and Mahadevan-Jansen and modeled the broad-band signal with a 4^{th} or 5^{th} order polynomial (with 1000 iterations) to eliminate background effects[35]. EMSC is a development of multiplicative scatter correction which is based on the assumption that the wavelength of the scatter light is different to the absorption of the sample and EMSC further considers the non-linearity of the scattering signals [36].

1.3.3 Smoothing

The signal to noise ratio (SNR) can be variable due to the Raman scattering being a low occurring phenomenon and the added constraints of imaging biological systems

and their relatively low scattering cross sections. To correct for some of the noise a Savitsky-Golay polynomial smoothing function was utilized in some of the studies presented here.

1.3.4 Normalisation

Raman spectral intensity can vary based on factors independent of the sample. These variations are introduced via changes in the irradiation laser power, optical component aging and degradation, sample fluorescence variance between sample groups, optical property variation between sample groups and treatments (opacity, absorptivity, refractive index, etc.). Background and baseline correction relieve some of these intensity variations however further normalization techniques are required before further analytical techniques are applied. Normalisation techniques applied in this thesis include.

1.3.5 Univariate Analysis

Univariate analysis is the selection, characterisation and comparison of individual peaks of interest in the collected Raman spectrum. Often these are vibrational modes of a molecule of interest which is either strong, sharp and with relatively little overlap as in the case with the 960 cm^{-1} peak (as seen in Figure 1-1), or the characterisation of the peak has shown to be reflective of the compound of interest despite its location with overlapping peaks as was shown for the 1070 cm^{-1} carbonate peak with its peak height and area strongly correlating with the weight percent carbonate found in apatite[33].

To characterise molecular species of interest through univariate peak analysis two predominate techniques were used. The first was a curve fitting tool found in the WiRE 3.2 software (Renishaw, U.K.) and includes a user interface where the user selects the start and end wavenumbers of the curve (or curves) of interest and selecting the height on the selected spectrum. A mixed 50% Lorentzian-Gaussian curve will show as a default and the width is then adjustable. After a fit is determined where the ratio of Lorentzian-Gaussian fit is adjusted to best fit the signal selected the included option of baseline correction with a straight line passing through the end points of the Raman shift range of interest is available. As described here, this is a very individually intensive process and may be highly subjective. This technique was used for initial analysis during spectral collection and when multiple peaks of interest occur in the same Raman shift range. With the ability to fit multiple curves, of mixed

Lorentzian-Gaussian fits in a selected range to best fit the signal, the level of input may allow for a better extraction of a singular peak of interest rather than an automated method. When a peak of interest is sharp and less sensitive to overlapping peaks, an automated method (in house written script) was used where the Raman shift range was selected and all the spectra any selected data set were then subjected to a integral function over that selected range to determine the peak area and the full width half maximum (FWHM) could also be determined.

1.3.6 Multivariate Analysis

Multivariate analysis is critical for the understanding of molecular trends in high-dimensional spectral data. Raman spectra are information rich and often the determination of multiple peak changes, and their relationship to each other are essential to gaining a full picture of the different molecular environments of experimental groups. These techniques include unsupervised and supervised techniques. Supervised techniques allow for the inclusion of labeled sample groups in the analysis.

1.3.7 Principal Component Analysis

Principal component analysis (PCA) is an unsupervised linear mathematical transform which enables the classification of datasets into distinct classes. The multivariate data collected is transformed into a smaller subset of derived variables so that each spectrum is a linear combination of orthogonal basis functions, called principal components (PC). These new variables represent the important variations found in the entire dataset in a more compact way. PCA analysis provides PCs and scores. The PCs contain spectral features showing the main molecular variation found between spectra in the dataset and the scores show the contribution of the PCs to the original dataset. PC1 captures the greatest variance, followed by PC2, etc. This also allows for dimensionality reduction by expressing the data in terms of a smaller number of PCs and compression can be achieved by retaining only the PCS of interest and discarding the PCs accounting for noise (higher order PCs).

PCA scores are often plotted against one another to produce PC-score plots and may be analysed to indicate if spectra are related. The grouping or clustering of spectra may suggest systematic differences between sample groups of interest. If grouping occurs, the examination of the PCs which are responsible for the grouping and

discrimination between sample groups often elude to the biochemical species of importance in sample segregation.

1.3.8 Partial Least Squares Discriminant Analysis (PLS-DA)

In many of the investigations presented in this thesis, PCA was used initially to determine if any grouping occurred using the unsupervised technique. Although some rough grouping emerged, PCA was not sufficient for identification of important spectral variables in the investigations presented in this thesis and thus only used as noise reduction technique. Due to PCA's rotational freedom which always expresses the greatest variance, the differences interesting to the investigation are sometime not the greatest differences. An easy and efficient way to maximize variation between samples is to use Partial Least Squares Discriminant Analysis (PLS-DA). Partial least squares regression has become a standard tool in chemometrics and used in chemistry and engineering and more fully described by Wold et. al [37]. PLS-DA is a predicative technique and allows for use of a priori knowledge to provide bioinformatics clues for the identification of spectral variables most effective in discriminating between different experimental groups. PLS as a discrimination tool was explored by Barker and Rayens in which they exposed it was preferable over PCA when discrimination was the goal and dimension reduction was needed [38]. This method of supervised classification has given very good results for relatively complex problems sets including spectra which were very similar in studies including discriminating isogenic cancer cells with different metastatic properties [39] as well as other Raman based problems [40,41]. PLS-DA also has the advantage of dealing with challenges biological datasets often confront in multivariate statistical modeling such multicollinearity [42] however consideration must be taken to avoid data over fitting.

'With four parameters I can fit an elephant, and with five I can make him wiggle his trunk.' – John von Neumann

Data over fitting causes a statistical model too closely fits a limited set of data points and starts to describe random error or noise instead of the fundamental underlying relationships. Data over fitting often occurs in models which are complex and much greater number of predictors (parameters) relative to the number of observations. This can ultimately cause a poor predictive performance as the model will exaggerate minor fluctuations in the data.

Multicollinearity occurs when high correlations among the independent/predictor variables are strong. As a result multiple predictors often convey the same information (redundant) and can skew their significance leading to unreliable and unstable estimates of regression coefficients. Multicollinearity can misleadingly inflate the standard errors making some variables statistically insignificant when they are significant.

1.3.9 N-FINDR

Spectral un-mixing methods are a relatively new addition to the micro spectroscopic imaging. This analytical approach originates from the area of remote sensing and mainly developed for usage in arial reflection spectroscopy. Spectral un-mixing was applied to Raman data by the Diem group [43] in 2008 and previously used in FT-IR imaging. The N-FINDR spectral un-mixing algorithm searches the original input spectra, from the non-dimension reduced input matrix, for the most extreme spectra present and exposes these as endmembers. These endmembers are then identified based on their spectral features as pure contributing component of the tissue and can be used to build maps with each map pixel (a spectrum) being comprised of the endmembers selected. A more detailed description of N-FINDR and its comparative advantages to both clustering and other spectral un-mixing methods can be found in a paper by Hedegaard et al. [44] and is presented in chapter 5.

1.3.10 Computational Considerations

All of the Raman data preprocessing and analysis was performed in the Matlab environment (The Mathworks, USA) using in house written scripts and the multivariate statistical analysis toolbox, PLS-toolbox (Eigenvector Research Inc., USA) unless otherwise stated. Many of the techniques described here and in further chapters were initially developed for analytical chemistry applications in various other sciences. Their adaptation to and constrains within use here are best described in various other texts.

1.4 Cardiovascular Calcification

Cardiovascular disease is a global concern involving several diseases which combined are responsible for taking more than 17 million lives in 2008 [45]. Cardiovascular calcification refers to the pathological deposition of calcium phosphate in blood vessels, myocardium, and cardiac valves [46]. Initially cardiovascular calcification was

thought of as a passive, degenerative and inevitable process with precipitation of calcium in microenvironments of high phosphate. Additionally calcification was thought to be uncommon in the coronary arteries until in the 1990's the understanding of the mechanisms behind and the frequencies of calcification in the cardiovascular system changed dramatically. Calcification was found to be occurring in a vast majority of significant cardiovascular lesions and in 90% of patients with coronary artery diseases. Osteogenic morphogens were found in calcifying blood vessels and subsequent work showed the presence of bone matrix in cardiovascular tissue in a subset of patients with severe aortic valve stenosis. This information and other findings combined established the 'osteogenic hypothesis' of cardiovascular tissue [47-50]. The 'osteogenic hypothesis' suggests valvular and vascular calcification is an active, regulated process with similarities to bone mineralization. Recently our group reported a presence of spherical particles in cardiovascular disease lesions which are composed of highly crystalline hydroxyapatite that crystallographically and structurally differs from bone mineral [51]. This raises an exciting new era for the field of cardiovascular calcification and is further discussed in chapter 4.

The importance of researching cardiovascular calcification grows as life expectancy continues to increase and age is strongly associated with increases in calcium accumulations in the aortic valve, coronary arteries and the aorta [49]. Initially the aim of these studies was to further understand the microenvironments in aortic valve calcification and an in-depth introduction can be found in the following sections. It is important to note however, the finding of a common mineral structure reported by our group may bridge current separation between vascular and aortic valve calcification [51] and thus chapter 4 investigates both.

1.4.1 Aortic Valve Calcification – Clinical Importance

The aortic valve maintains healthy heart function by ensuring unidirectional flow throughout the cardiac cycle. This thin tissue valve opens and closes approximately 40 million times a year and three billion over the average lifetime. Aortic Valve calcification, when causing aortic sclerosis, presents the second most common indication for cardiac surgery and carries an 80% 5-year risk of progression to heart failure, valve replacement or death [52,53]. With surgery being the prevailing treatment option for patients with moderate to severe aortic valve calcification [54] pharmaceutical alternatives are desperately needed yet remain elusive. With the aortic valve being relatively inaccessible and a poor candidate for *in vivo* monitoring,

the vast majority of human disease progression has been described from observations of the valves after removal from the patient.

Animal models are being used in research and potential *in vitro* models are being explored. Of all the potential options, *in vitro* models are the most attractive for investigating molecular mechanisms of disease onset and pharmaceutical treatment potential, however these model systems need to be carefully characterized and compared before utilization [54].

1.4.2 The Aortic Valve – Structure and Function

The typical aortic valve is tricuspid and responsible for mediating the unidirectional flow of blood from the left ventricle of the heart to the aorta for transport of oxygenated blood to the entire body (Figure 1-4 A). Coaptation of the three cusps ensures a complete closure of the valve during diastole and therefore prevents regurgitation of blood from the aorta to the left ventricle. During systole, the cusps open so they are parallel to the blood flow and are flexible enough to deform with little obstruction to the passing oxygenated blood (Figure 1-4 D). Thereby there is a great dependency on the valve tissue's mobility, pliability and structural integrity when performing its essential functions.

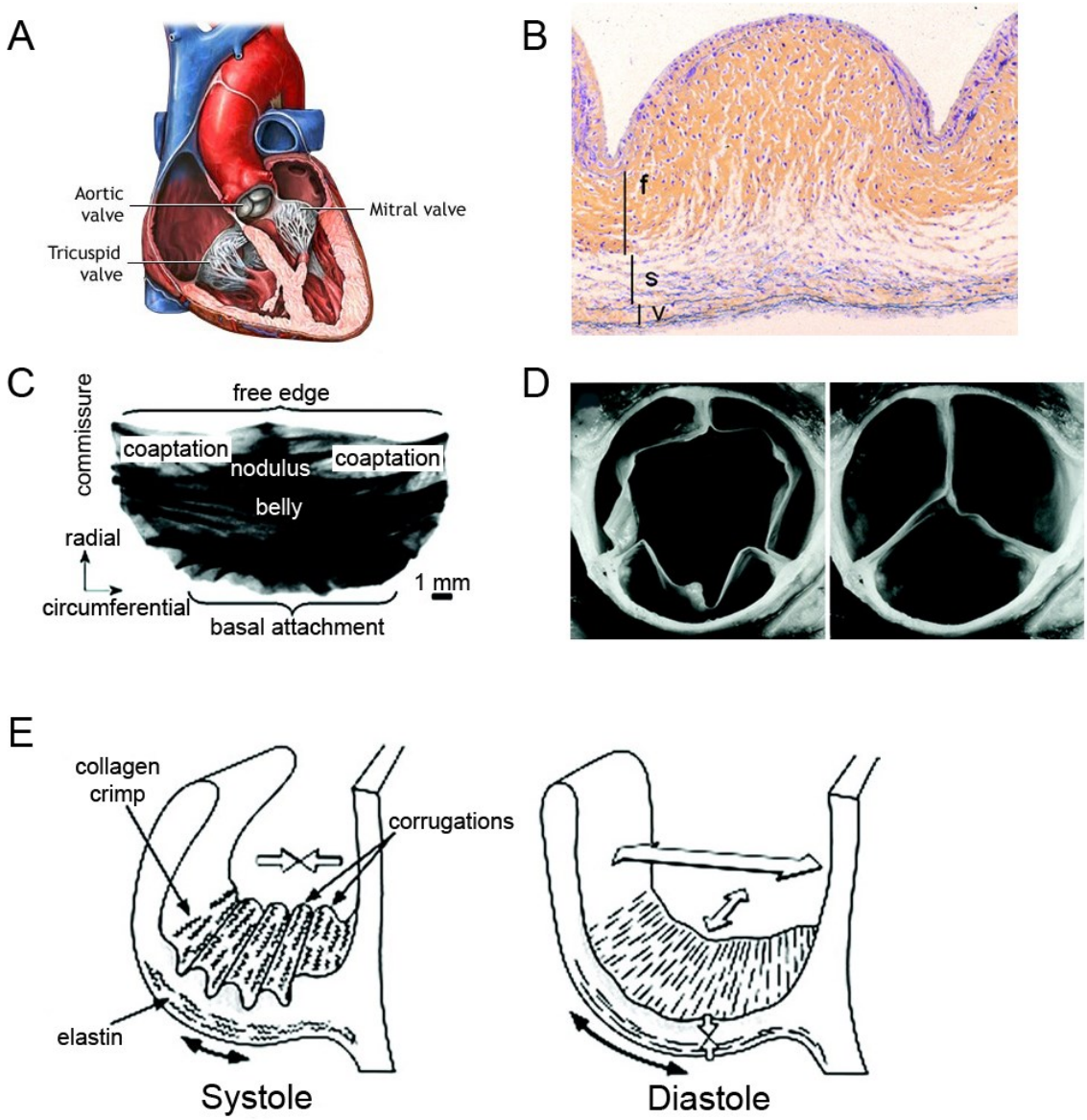

Figure 1-4 The human aortic valve and its cusps. A. Drawing of the human heart as a cross section cut in the coronal plane. The tricuspid aortic valve is highlighted with the three leaflets in white and the sinus directly above them with coronary artery exits also displayed. B. Histological cross section of an aortic valve cusp in typical systole configuration showing the three distinct layers, f- fibrosa, s- spongiosa, v – ventricularis using a Movat Pentachrome stain (collagen – yellow, elastin – black), 100x magnification. C. Diagram of cusps showing location of belly, commissure, nodulus, and regions of coaptation. D. Outflow perspective of aortic valve during systole (right) and diastole (left). E. Cross section of the valve leaflets showing the architecture and configuration of the collagen and elastin during systole (right) and diastole (left). Some information reproduced from [55-57]

Each cusp is attached to the aortic wall in a semilunar fashion, with adjacent cusps coming together at commissures at the aorta (Figure 1-4 C). The cusps individually descend into the basal attachment to the aortic wall and the adjacent aortic root is

shaped as a dilated pocket called the sinuses of Valsalva, which bulges with each ejection of blood. The middle of the free edge of each cusp contains a fibrous mound called the nodule of Arantius, (Figure 1-4 C). This fibrous mound is where each cusp meets in the center of the valve and it helps ensure the cusps can withstand the pressure gradient between the aorta and left ventricle. The cusps are described in relation to the coronary artery which extends from it or lack there-of, namely: left, right, and non -coronary cusps.

Aortic valve leaflets consist of four layers with varying, distinct extracellular matrices. They are the ventricularis (closest to the left ventricular chamber), spongiosa (middle), fibrosa (most apparent layer at the aortic side) and arterialis (at aortic surface below basement membrane and endothelial cells) (Figure 1-4 B). These layers vary in thickness as the valve extends from the annulus to the free margin of each cusp.

The ventricularis comprises of elastic collagenous fibers and elastin fibers aligned in the longitudinal direction (parallel to blood flow). This layer provides the tensile recoil necessary to retain the folded shape of the cusp. The spongiosa is located near the base of each cusp and is a very loose and watery connective tissue of varying thickness. This layer is mostly proteoglycans and water as to damper vibrations of the fibrosa when the leaflets close and this layer adds considerable plasticity. The spongiosa does contain some fibers and cells which are typically oriented radially. The fibrosa is a very dense series of parallel tendinous cords (more towards the free end of the leaflet) and in rigid sheets of tissue component collagenous fibers. These cords/fibers run circumferentially. This is the mechanically strongest part of the leaflet and provides the principle support of diastolic pressure. The arterialis is a thin layer at the aortic surface which consists of small elastic collagenous fibers which are relatively (in comparison to the fibrosa) loosely arranged.

The percentage of each type of collagen identified in the valve is ~74% collagen type I, ~24% type II, and ~2% type V. Collagen is principally responsible for structure and mechanical strength, while the elastin of the valves have been described as providing the extensibility. Human valves are approximately 11% elastin (Dry weight ratio) and together with collagen, these two comprise of approximately 80% of the total valvular protein. The glycosaminoglycans are the ground substance for which the other components are laid upon [58].

The two predominate types of cells which populate the aortic valve are endothelial cells and valvular interstitial cells (VICs). VICs are a mixed cell population which will be described in more detail later. The valve cusps are sufficiently thin to be nourished by diffusion from the blood bathing them however some valves may contain vasculature, especially towards the base, therefore smooth muscle cells may also be present in arterioles and venules and not just as subpopulations of VICs. The blood contacting surface of the valves is populated with endothelial cells which are continuous with the lining of the vessels and the sinuses and with the endocardium [58]. VICs populate the body of the leaflets in all the layers [58]. Additionally nerves have been identified within some valves [59], however their function role has not yet been clarified.

1.4.3 Valvular Disease Progression / Potential Initiating Factors

In diseased valves the normally efficient thin tissue transforms to become rigid, thickened and in some cases cusps fuse together. This disrupts the primary function of ensuring uni-directional flow and places an incredible burden on the left ventricular muscle. Clinically there are 4 stages in this progression, 1 – healthy, 2- moderate, 3 – mild and 4 - severe. Patients with severe aortic calcification, who do not undergo surgery, have a life expectancy of under 5 years [53]. Various mechanisms have been proposed to lead to aortic valve calcification, including osteogenic differentiation of VICs, cellular apoptosis related calcification and necrosis-related calcium deposition [60-63]. Different hypotheses also exist as to the specific biomolecular and/or mechanical initiating factors.

Wound repair is thought to be a critical step in initiating the pathogenesis of several valvular and vascular pathological conditions [58]. Injury may be mechanically induced during medical procedures or a more complex phenomenon with no external factors clearly defined. In any case this injury denudes the endothelial cells which results in a local area of VICs in a void of the potentially critical regulatory signals typically from the endothelium [63]. This instigates the initiation of the repair process. Artificial organ bath maintained tissue models suggest the removal of the endothelial cells causes elongated cells to close over the wound edge growing parallel to the edge and overlapping each other without reestablishment of the monolayer. These cells also continuously express proliferative proteins. A porcine mitral valve

study results suggested the VICs populating areas towards the ventricle were more proliferative than the VICs at the atrial side under the same stimulation [64].

Intrusive angiogenesis due to the down regulation of chondromodulin-I, an angiogenesis inhibitor protein found in the avasular tissues cartilage and the eyes [54] is another potential initiating culprit. Hakuno et al. [54] reveled expression of chondromodulin-I at the mRNA and protein levels in all four cardiac valves (aortic, mitral, pulmonary and tricuspid valves) indicating a VICs mediated regulation of angiogenesis. This indicates chondromodulin-I is secreted from cultured VICs to potentially inhibit vascular endothelial tube formation and migration.

Similar initial pathological ignitions may exist between atherosclerosis and aortic valve calcification. This relationship was suggested as observed similarities between the two emerged including local inflammation, lipid infiltration and phenotypic alterations progressing towards a more osteoblastic phenotype [65,66].

1.4.4 Current Treatment Options for Aortic Valve Calcifications

Current treatment options for aortic valve calcification are almost exclusively surgical. If the patient is a candidate for replacement, the surgeon and patient may choose between different replacement valves which generally fall into two categories: biological (sometimes referred to as tissue / bioprosthetic) and mechanical valves. The type of valve replacement has to be carefully selected as it is the patient's specific risk factors which will determine the best option. Advantages and disadvantages to available options are described in Table 1-2.

Table 1-2 Comparison of replacement heart valve options. Note: Subsets of each type including tissue types and design do exist beyond this simple classification. Reproduced with information from [67].

Type of replacement valve	Advantages	Disadvantages
Biological	No need for lifelong anticoagulation	Limited durability
	Better replication of natural flow	Potential for re-calcification
		Replacement means repeat open heart surgery
Mechanical	Practically unlimited durability	Lifelong anticoagulation
	For adult patients repeat operations less likely	Failure is catastrophic
		Flow conditions altered
		closure can be abrupt and damage cells in blood

Current surgical options are suitable for a majority of patients as conventional valve technology is very mature with a well-defined performance. As surgical approaches and techniques improve the surgical outcomes are as well. Very often the main consideration is durability, as the replacement should ideally outlive the patient as reoccurring surgeries are associated with higher complication risks. The population in the most need of a better replacement is pediatrics. Children are less tolerant of prosthetic devices and as a minority of the commercial market (less than 10% of the adult market) their commercial demand renders pediatric specific research less than viable [68].

1.4.5 Obstacles Facing Improved Options for Aortic Valve Calcification

The development of better treatment options, including pharmaceutical intervention at early stages, improved bioprosthetic valves, and ultimately the potential of a tissue engineered valve is highly dependent on the better understanding of the complex environment at the cellular level. The aortic valve is not accessible for non-invasive monitoring of pharmacological agents, animal models are expensive with their relevance questionable, and a proven *in vitro* model remains elusive. Understanding the basic nature of the cells which populate and maintain the valves is important for the development of new treatment or replacement options. Additionally the VICs'

ability to change phenotypes and begin the pathogenic process is still a mysterious phenomenon which creates a limiting step towards developing a trustworthy model.

1.4.6 Valvular Interstitial Cells – An Introduction

Valvular Interstitial Cells (VICs) are the prevalent cell type in the aortic valve which are believed to be critical in maintaining function [69] and have been proposed as the cells involved in the pathogenic calcification[58,70]. This mixed cell population contains myofibroblasts (when activated), fibroblasts, smooth muscle cells and a population of valvular progenitor cells. VICs heterogeneity in relation to different locations within the valve remains unknown.

Myofibroblasts are mesenchymal cells which possess the phenotypic markers of both muscle and non-muscle cells [71]. During the process of 'activation' in some tissues, fibroblasts respond to wound healing by trans-differentiating into myofibroblasts. The myocardium reportedly contains cells which undergo this activation and therefore might act as contributing source [72].

VICs are strongly attached to and synthesize the extracellular matrices [58]. They express matrix degrading enzymes and their inhibitors which exposes their ability to respond to and control the remodeling of the collagen and other matrix components [73]. VICs in healthy valves are predominately quiescent with low levels of α-smooth muscle actin (SMA) and low levels of matrix metalloproteinases (MMPs). These cells are however very plastic and readily respond to a number of stimuli (biomolecular and mechanical) by altering their phenotype. These changes may involve the necessary remodeling of the extracellular matrix, in response to injury or deviation into a pathological phenotype.

Activation and the variable responses of VICs has eluded to a spectrum of described VICs phenotypes [74]. The various types of VICs and some of their stimulatory mechanisms are expressed in Figure 1-5. These various VICs phenotypes are listed with their location and function in Table 1-3.

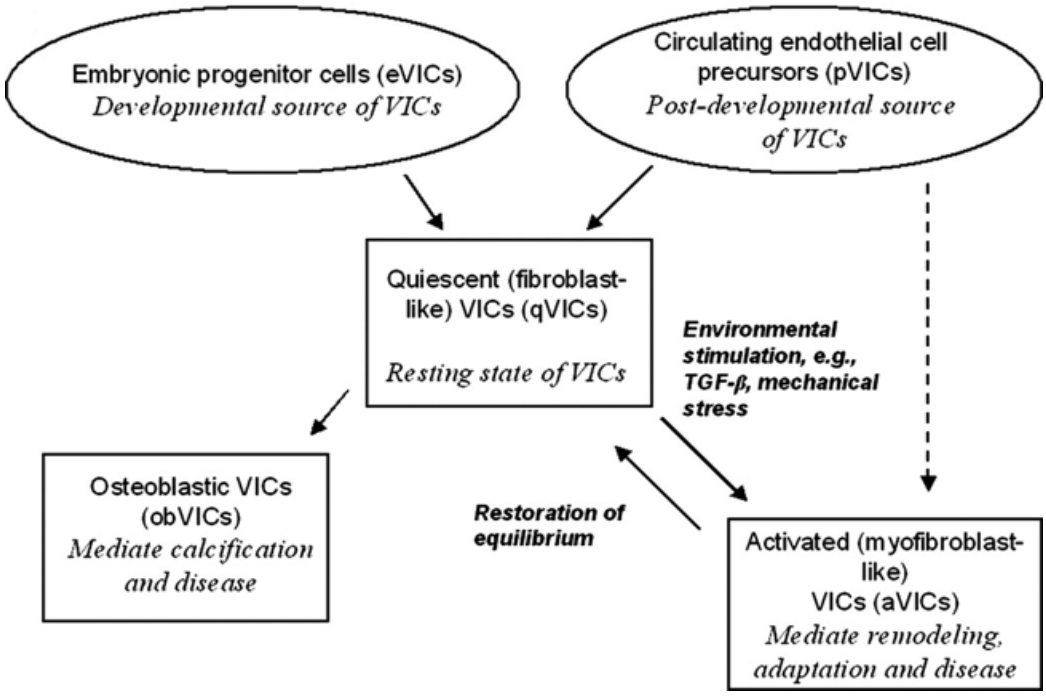

Figure 1-5 Heart valve interstitial cell phenotypes mapped into five variable classifications in which VICs transition between each due to external stimuli. Reproduced with information from [55,74].

Table 1-3 General categories of heart valve interstitial cells phenotypes, location within the body and function. Reproduced with information from [55,74].

Cell Type	Location	Function
eVICs	Embryonic cardiac cushions	Give rise to resident qVICs, possibly through an activated stage; EMT can be detected by the loss of endothelial markers and gain of mesenchymal markers
qVICs	Heart valve leaflet	Maintain physiological, normal valve structure and function and inhibit angiogenesis in the leaflets
pVICs	Bone marrow, circulation, and/or heart valve leaflet	Enter valve or are resident in valve to provide aVICs to repair the heart valve, may express CD34, CD133, and/or S100
aVICs	Heart valve leaflet	α-SMA containing VICs with activated cellular repair processes including proliferation, migration, and matrix remodeling; respond to valve injury caused by pathological conditions and abnormal hemodynamic/ mechanical forces
obVICs	Heart valve leaflet	Mediate calcification, chondrogenesis, and osteogenesis in the heart valve; secrete alkaline phosphatase, osteocalcin, osteopontin, bone sialoprotein

Valvular progenitor cells have been identified in adult human pulmonary valves [75] and in abundance in porcine valves [76]. This progenitor cell population has also demonstrated increased angiogenic activity in calcified aortic valves in comparison to healthy valves [77]. This population of cells presents a potential obstacle to efforts of controlling consistently primary VICs phenotype in culture as it is extremely responsive.

Porcine aortic valves are commonly used in efforts to unravel the molecular pathways leading to pathogenesis. The VICs isolated from them are readily available, inexpensive and robust when grown *in vitro*. They form 'calcified nodules' which have been heavily researched, including investigations on the pharmacological effects on nodule formation and growth being reported. However no direct information relating to, much less defining, the relationship between these nodules and human aortic

pathogenesis has been reported. Additionally, porcine aortic valves thicken *in vivo* however are not reported to calcify.

Porcine VICs possess the ability to contract when exposed to non-receptor mediated and receptor-mediated stimuli [72,78]. In these experiments porcine cusp tissues of all four valves were carefully removed from fresh hearts and maintained in an organ bath. One end of each tissue section was attached to a strain gauge and the other to a static steel rod and lengths of cotton string. After the tissue stabilized, it was preloaded with tension of 3mN and allowed to relax. The tissue was then challenged with 90 mmol/L KCL and increasing concentrations of endothelin-1. All cusp tissue demonstrated a contractile response to the KCl and an increasing response to endothelin-1 [74]. Previously tissue valves had been shown to be responsive to both adrenaline and angiotensin-II stimulation [79]. Cells from porcine aortic valves contracted in response to angiotensin II, bradykinin, potassium chloride, carbachol, adrenaline and endothelin. They were also shown to relax in response to isoproterenol [80].

Some recent studies have exposed areas in which complication may arise in efforts to replicate valve function *in vitro*. Isolated and cultured VICs proving unreliable as far as phenotypic expression is just one of those challenges. In culture there remains a limit to the ability to manipulate VICs into normal healthy function such as extracellular protein maintenance. For example, elastin has been described as the most difficult component of the valvular ECM to produce in an *in vitro* environment [81]. Knowing elastin has a critical role in the native valve has lead researchers to investigate systems which specifically produce elastin.

1.4.7 Valvular Interstitial Cells in Culture

In culture VICs are elongated and form an orthogonal pattern during overgrowth and closely resemble fibroblasts post confluence [82,83]. If culture continues cells will pile in ridges reminiscent of smooth muscle cells however lacking the 'hill and valley pattern' [82,84]. In about 20% of cultures of mitral valve VICs a selection of 'cobblestone-type' cells which are non-endothelial cell islands with a cuboidal morphology will spontaneously grow into confluence and stray distinctly from the fibroblastic morphology [85]. Cultured VICs showed serum dependent growth rates and are extremely responsive to media supplements [80]. VICs, both *in vitro* and *in vivo* have the ability to communicate to one another. Functional gap junctions and

adherens junctions have been identified indicating a communication and tight bonding respectively[58].

Some but not all aortic VICs in culture have previously stained positive for alpha smooth muscle actin (SMA) along the long axis of the cell and throughout the cellular processes [80]. In valve tissue sections the regions closest to the ventricular side of the leaflet stained the most prominently for SMA however SMA was seen throughout. This is an example of a myofibroblastic feature similar to smooth muscle cells [58].

Human VICs have been shown to express a variety of thin and thick filament contractile protein genes which are typical of both cardiac and skeletal muscle. Expression of the non-muscle transcripts appear to be favored in contrast to the muscle-specific isoforms associated with myocytes [72]. The same study results indicated myogenin regulates the expression of some or all the skeletal muscle contractile protein genes in the human heart.

VICs have been found to be very responsive and their quiescent state is described as a period in which the cells are awaiting signals for activation [58,69]. These responses in culture are thought to be indicative of a communication with the endothelium lining the valves which provide soluble growth factors that are mitogenic to the interstitial cells and between the VICs themselves. Additionally mechanical and flow stimuli are initiated responses and phenotypic changes.

Several attempts to inhibit nodule formation / osteogenic expression have been demonstrated by using *in vitro* models of calcification. Atrovastatin was shown to inhibit expression of alkaline phosphatase and osteocalcin in human VICs [60]. Additionally, *in vivo* studies have been discovered and used to research pharmacological intervention. In an *in vivo* study on hypercholesterolaemic rabbit aortic valves, atorvastatin treatment was associated with the reduction of calcification [86].

2 Improving Spectral Interpretation of Differences in Raman Spectra of Cells and Tissue Using PLS-DA VIP Scores

2.1 Abstract

In-vitro Raman spectroscopy used for non-invasive, non-destructive characterization of single cells and tissues have proven to be a powerful tool for understanding the complex biochemical processes within biological systems. It enables the comparison of a wide range of in-vitro model systems by discriminating experimental groups based on their biomolecular differences through the comparison of information rich spectra. However, one persistent challenge in Raman spectroscopy has been the highly complex structure of cell and tissue spectra, which comprise signals from lipids, proteins, carbohydrates and nucleic acids, and which may overlap significantly. This leads to difficulty in clearly identifying which molecular components are responsible for the changes seen between sample groups. To address this problem, Partial Least Squares – Discriminant Analysis (PLS-DA) Variable Importance Projection (VIP) scores as heat maps combined with group difference spectra were applied as a technique to highlight the significant biochemical changes between sample groups. To illustrate the advantages of this method we compared two biological systems. The first demonstrates the ability of Raman spectroscopy to analyze single cells involving cultured HeLa cells in their live, fixed, fixed and ethanol dehydrated, and fixed, dehydrated and rehydrated states. Fixation, ethanol dehydration and rehydration are known to induce molecular changes in the lipids and proteins within each cell and here the PLS-DA VIP scores plots expose these known differences. Secondly unaltered human tissues comparing healthy bone tissue to osteoporotic bone tissue was investigated. Osteoporotic bone is known to have subtle differences in the mineral and organic matrix composition when compared to healthy bone and again the differences are shown clearly in the PLS-DA VIP score plots. These two contrasting biological studies act as model systems for illustrating the use of VIP score heat maps to highlight statistically significant biochemical changes of the difference spectra and thus important changes between experimental groups of interest.

2.2 Introduction

Raman micro-spectroscopy has been utilized successfully to characterize and compare a wide variety of biological samples ranging from single cells to whole tissues both *in vitro* and *in vivo* [39,87-89]. Raman spectroscopy has proven to be an ideal tool for the non-invasive measurement of lipids, proteins, carbohydrates, nucleic acids, and mineral in both living and fixed systems [12,90,91], allowing for characterization and comparison of biologically interesting samples without altering them. A more complete description of the non-invasive advantages of Raman spectroscopy can be found in the introduction.

Previous studies have demonstrated the benefits of applying multivariate analysis methods for the analysis of Raman spectra taken from biological systems [12,44,92,93]. This allows for the comparison of changes on a whole spectrum basis, instead of individual peaks and their corresponding bonds. Examples include but are not limited to discriminating isogenic cancer cells [39], circulating tumor cells [90], the *in vitro* calcification of different cell types [12], cell activity studies [91], and cell differentiation [94]. Methods previously used for the classification of biological Raman spectra include unsupervised methods such as cluster analysis and principal component analysis (PCA). Additionally a wide range of supervised methods have been applied including Linear Discriminant Analysis (LDA), Partial Least Squares – Discriminant Analysis (PLS-DA), Support Vector Machines and Neural Networks [39,95-99]. These tools have also been used in other spectroscopy techniques including NMR and mass spectroscopy for the analysis of various data types including metabolomics data [100,101]. In order to fully utilize the power of these multivariate analytical techniques in biological systems, the experimental design must ensure the requirements for each technique are met and the interpretations of the results are translatable into biologically meaningful parameters.

Ultimately the analysis of the Raman spectra, whether simple or complex, often strives to reveal the molecular level differences between experimental groups of interest. Complications in both the analysis and interpretation may arise from multiple overlapping Raman bands found in the same spectral range. Despite Raman spectroscopy's relatively narrow spectral peaks and bands, overlapping Raman signals make it difficult to discern whether the differences between sample groups originate from changes in minerals, lipids, proteins, carbohydrates or nucleic acids, or

if there are combined effects which act together to discriminate the groups of interest. Thus a focal area of development for Raman spectroscopy entails combining sophisticated statistical techniques to better visualize and often simplify the spectral differences of interest and their possible combined meaning for the investigation.

To improve the interpretation of the resulting Raman spectra, we apply here PLS-DA Variable Importance Projection (VIP) scores to highlight the spectral and thus molecular changes which significantly discriminate between sample groups. Overlaying the difference spectrum between groups with a heat map defined by the VIP scores clearly highlights both the bands which contribute the most to the model's ability to distinguish between experimental groups and the trends of those changes. This also highlights the most statistically significant molecular changes between trial groups.

To illustrate the advantages of combining PLS-DA VIP score heat maps in conjunction with difference spectra to expose the critical molecular changes in biological systems, this method was applied to study single cell spectra of HeLa cells in their live, fixed, dehydrated and rehydrated state. In addition this method was used to compare spectra obtained from unaltered fresh human bone from two patients, one healthy and one suffering from osteoporosis.

2.3 Materials and Methods

2.3.1 HeLa Cell Culture

HeLa cells were cultured in DMEM Glutamax medium supplemented with 1% (v/v) antibiotic–antimycotic, 10% (v/v) fetal bovine serum (FBS) (all, Invitrogen, U.K.). All HeLa cells were cultured on MgF_2 glass slides (Global Optics, U.K.) and seeded at $1x10^4$ cells/cm^2. Prior to cell seeding, MgF_2 glass slides were incubated in 100% FBS (same as used for the culture medium) for six hours at 37 °C. Raman spectral collection was then performed after two days. All cells were maintained in 37 °C with 5% CO_2, and at 95% relative humidity.

2.3.2 Fixation, Dehydration, and Rehydration of HeLa Cells and Raman Imagining Conditions

Live HeLa cell Raman imaging was performed after two days in culture and for a maximum duration of 30 minutes after removal from the incubator. Live cells were

imaged at a maintained 37°C in PBS in with the cells on the MgF_2 glass slides contained in a glass petri dish. Post Raman imagining HeLa cultures were fixed in 3.7% (v/v) formaldehyde (FA) for 40 minutes at 4°C and rinsed three times in phosphate buffered saline (PBS) and kept in PBS at room temperature for subsequent Raman imaging of fixed cells.

Cells were then dehydrated in an increasing graded ethanol series from 25%, 50%, 70%, 90% and 100% (twice) (v/v) series for 5 minutes in each solution and subsequently placed in a desiccator. Raman spectra were then collected on the dried cells at room temperature (cells on the MgF_2 glass slides were imaged while placed onto a glass slide).

Lastly cells were re-hydrated by submerging the dried and fixed HeLa cells on MgF_2 substrates in PBS for 30 minutes before Raman imaging. Raman imaging was collected with the cells on their MgF_2 in PBS, in a glass petri dish, at room temperature.

2.3.3 Human Bone Tissue Isolation and Raman Imaging Conditions

Human bone tissue was obtained from Charing Cross Hospital (London, U.K.). Cortical bone from the femurs of two patients, one male (73 years old) and one female (72 years old) undergoing hip replacements are included in this study. The female patient was diagnosed with osteoporosis. Directly after removal from the patient the fresh bone tissue was placed into a sterile container and washed with PBS at room temperature before testing. Raman imaging started within one hour after removal from the patient and completed within five hours with sterile PBS washes at 30 minute intervals to help prevent drying and contamination.

2.3.4 Raman Spectroscopy

Raman spectra were measured with a Renishaw InVia (Renishaw, U.K.) spectrometer connected to a Leica (Leica, Germany) microscope as previously described in the introduction and previous publications [6]. Briefly, the spectrometer uses a high power 785 nm diode spot laser (~30 mW at sample; Renishaw, U.K.) with a focal size of approximately 10 x 20 x 40 μm for excitation. The laser was focused on individual cells by a 60× (NA = 1.0) long working distance (2 mm) water immersion objective (Nikon, U.K.) or a 100× (NA = 0.9) objective (Leica, U.K.). A heated stage was used to 37°C for live cell imaging (Linkam, U.K.).

For all samples the spectral range selected consisted of the biological fingerprint region (620–1720 cm^{-1}) recorded at a resolution of ~1–2 cm^{-1}, with 3 accumulations of spectra each with a 5 second integration time. One spectral collection was taken from each individual cell. Backscattered radiation was collected by the same objective then passed through a 785 nm edge filter to block Rayleigh scattering and reflected laser light, before being directed through a 50 μm slit into the spectrometer equipped with a 1200 lines/mm grating, and finally detected by a deep-depletion charge-coupled device detector.

A total of 2080 spectra were collected from single HeLa cells consisting of 384 from live cells, 714 from fixed cells, 338 from dehydrated cells and 644 from dehydrated cells. These cell spectra were collected from three independent batches of cultured HeLa cells. A total of 110 spectra were collected from fresh human bone with 59 spectra from the normal bone sample and 51 spectra from the osteoporotic bone sample.

2.4 Data Analysis

All data analysis was performed in MatLab R2011a (The Mathworks, Natick, MA, U.S.A.) with in house written scripts, many in courtesy of Dr. Martin AB Hedegaard, in combination with the PLS_toolbox 7.0 (Eigenvector Research, U.S.A.).
Spectra for the HeLa cell study were background corrected by subtracting the spectrum of PBS and substrate (collected in the same conditions) for the hydrated samples and the background of the substrate only from the dehydrated samples. All spectra were normalized using extended multiplicative signal correction (EMSC) [36,102]and smoothed using a Savitsky-Golay filter (five points, second-order polynomial) [34].

Spectra from the bone tissue samples were normalized using EMSC and used no background correction as all spectra were measured in comparable conditions and the tissue thickness was greater than the penetration depth of the focused radiation volume.

The peak labels found in the Raman spectra presented in this chapter are representative of the peaks found in literature and may be slightly shifted from the precise peak positions found in the spectral means displayed.

For classification we applied Partial Least Squares – Discriminant Analysis (PLS-DA). PLS-DA uses the properties of normal PLS regression to rotate a principal component analysis (PCA) model to best explain the differences between groups. Using the model to predict a matrix of zeros and ones depending on the experimental group allows for a rotation of a PCA model so it best discriminates based on group variances.
To highlight the variables which contribute the most to the discrimination, we calculate the Variable Importance Projection (VIP) score. The VIP score works as a summary of the importance of the projection when finding the latent variables [103-105]. Assuming a single response y and p predictors the PLS model can be expressed as

$$\mathrm{X} = \mathrm{T}P^{T} + E$$

$$y = Tb + f$$

Where X is an (n × p) matrix of predictors, T (n × h) is the projection of X (the X score), P (p × h) is an orthogonal loading matrix, and E (n × 1) n is an error term assumed to be independent identically distributed random normal variables (alias residuals). y (n × 1) is a single response array, b (h × 1) is the loadings response vector and regression coefficients for T, and f (n × 1) represents the residual.

Using this definition the VIP score for the j'th variable can be calculated as

$$VIP_j = \sqrt{p \sum_{k=1}^{h} (SS(b_k t_k)(w_{jk}/\| w_{jk} \|)^2) / \sum_{k=1}^{h} SS(b_k t_k)}$$

where w_{jk} is the j-th element of vector w_k and

$$SS(b_k\, t_k) = b_k^2 t_k^t t_k$$

Also described in more detail by Chong and Jun [103]. The VIP score of a predictor was first fully published in 1993 by Wold et al. [106].

A PLS-DA model including VIP scores was calculated for each of the following four comparison cases: live vs. fixed HeLa cells, fixed vs. dehydrated HeLa cells, dehydrated vs. rehydrated HeLa cells and normal bone vs. osteoporotic bone. Each model was cross validated using a leave out random subsets with 10 data splits. For each model the average and difference spectra were calculated to analyse the spectral differences. The difference spectra were then overlaid with a heat map of the VIP score for each model (method originally proposed by Dr. Martin AB Hedgaard).

2.5 Results

2.5.1 Case 1: HeLa Cells

Raman spectra were collected from HeLa cells after 2 days of culture on the MgF_2 substrates and were of the same morphology of previously reported HeLa cells. Single HeLa cells were selected for Raman imaging as the HeLa cells were not confluent at the time of testing. Figure 2-1 shows the mean Raman spectrum of a) live cells, b) fixed cells, c) dehydrated cells and d) rehydrated cells. All spectra contain bands expected from single cells including the RNA/DNA bands (669, 785, 811, 828, 1093, 1257, 1320, 1375 and 1575cm^{-1}), Amino Acids bands (Phe: 622, 1002, 1032, 1602 cm^{-1}, Tyr: 645, Trp: 760, 1554 cm^{-1}, Pro: 937cm^{-1}), lipid bands (877, 1095, 1124, 1255cm^{-1}) and the Amide III and Amide I bands at 1337 and 1655 cm^{-1} respectively (more detail on band assignments, peak strength and shape information, where appropriate, can be found in Appendix 1). There are significant visual differences in the average spectrum in the amino acid Phenylalanine (Phe) band at 1002 cm^{-1} for the dehydrated cells in Figure 2-1c and some changes in the shape of the Amide I band when compared to the three other HeLa cell experimental groups.

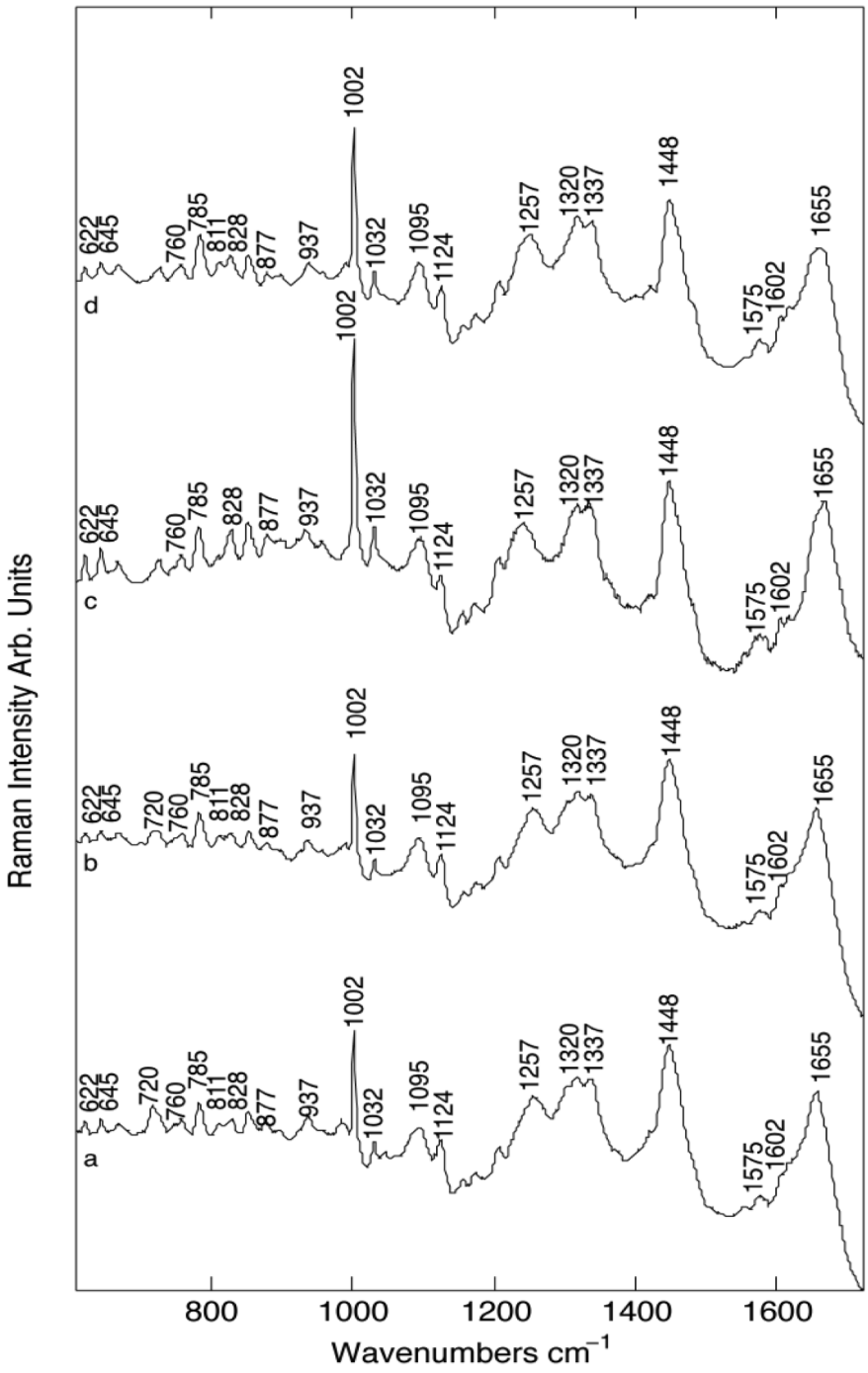

Figure 2-1 The mean spectrum of each HeLa cell sample groups: a) live, b) fixed, c) ethanol dehydrated, and d) rehydrated form. Visual changes can be seen in the Amide I band at 1655cm^{-1} and the intensity of the phenylalanine (Phe) band at 1002 cm^{-1}.

A PLS-DA model was employed to compare live vs. fixed, fixed vs. dehydrated and dehydrated vs. rehydrated HeLa cells with the resulting model details shown in Table 2-1. For each model the VIP scores were calculated and plotted as a heat map on the background of the difference spectra shown in Figure 2-2 showing the average difference spectra between a) live-fixed, b) fixed-dehydrated and c) dehydrated-rehydrated. The more intense the green band, the more significant the selected Raman spectral band range is in the PLS-DA model's ability to distinguish between the groups.

Table 2-1 PLS-DA model details from HeLa cell experimental group comparisons.

Model	Components	Sensitivity	Selectivity
Live vs. Fixed	3	0.911	0.959
Fixed vs. Dehydrated	2	1.00	1.00
Dehydrated vs. Rehydrated	2	1.00	1.00

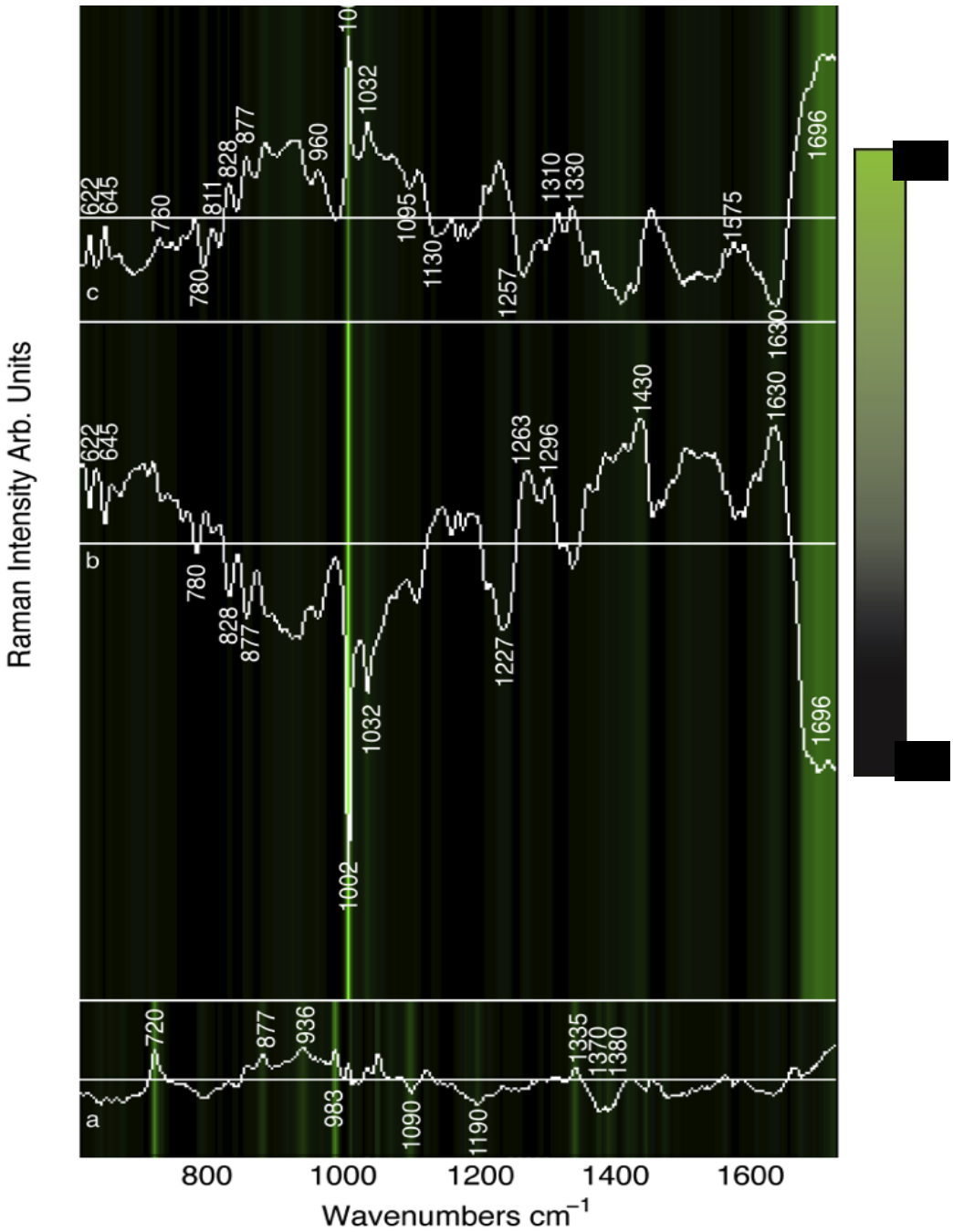

Figure 2-2 Difference spectra overlaid by VIP scores for a) live-fixed, b) fixed-dehydrated and c) dehydrated-rehydrated. The brightness of the green background indicates the value of the VIP scores with the greater the colour intensity corresponding to a higher VIP score and thereby a greater significance of those bands to the PLS-DA models as shown in Table 2-1.

Features highlighted in Figure 2-2a between live and fixed cells are mostly related to phospholipids (720, 1092cm^{-1}) and lipids (877, 935, 983, 1335 and 1370cm^{-1}). It is important to note that the most statistically significant changes highlighted by the VIP

scores are not necessarily the largest variations in the difference spectrum (this is further discussed in the discussion). Differences between fixed and ethanol dehydrated cells are also distinctly visible in Figure 2-2b with the most significant differences being related to unfolding of proteins, visible by the large shift in the Amide I band at 1630-1696cm^{-1} and the exposure of phenylalanine due to break up in α-helixes and β-sheets resulting in higher intensities of the 622, 645, 1002 and 1032cm^{-1} bands. In addition there are visible changes in DNA related vibrations at 780 and 828 cm^{-1} and a decrease in lipid content 877, 1227 and 1430cm^{-1}. Rehydrating the cells in PBS refolds the proteins to a certain degree reversing these changes as seen in Figure 2-2c, however this reversal does not return proteins to their fully native state and leaves visible changes in the live and fixed cell spectra.

2.5.2 Case 2: Bone Samples

The average spectra of the two sample groups are visible in Figure 2-3 with spectrum a) representing osteoporosis bone and spectrum b) representing normal bone. Raman bands observed in both average spectra include Amino Acids (Phe: 622, 645, 1002, 1032 cm^{-1}, Trp: 756 cm^{-1}, Pro: 815 cm^{-1}), Minerals (Hydroxyapatite-: 962 cm^{-1} carbonate ions CO_3: 1073 cm^{-1}) and the Amide III and Amide I at 1245-1305 and 1660 cm^{-1} respectively as well as CH_2 bending modes at 1453 cm^{-1}.

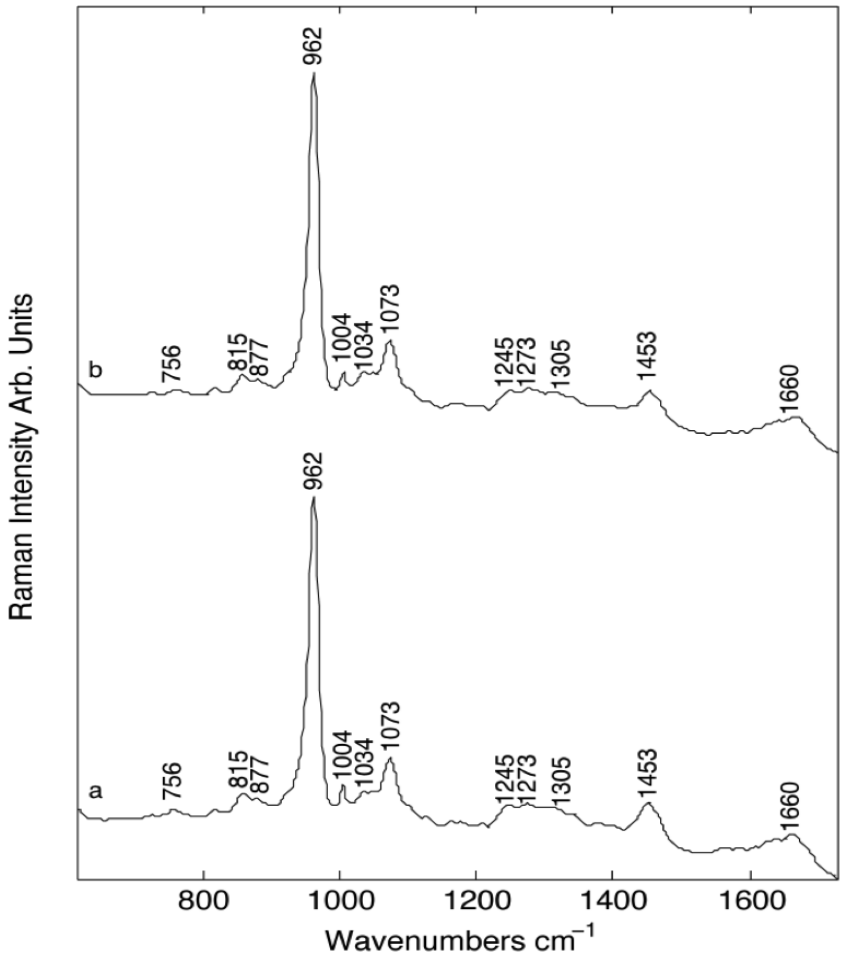

Figure 2-3 Mean Raman spectrum of a) human osteoporotic bone spectra and b) human normal bone spectra. The spectra show nearly no visible changes but are differences were distinguishable by the PLS-DA model as seen in Table 2-2.

Similar to the case of the HeLa cells, a PLS-DA model and its VIP scores were performed with the resulting model details presented in Table 2-2. The difference spectrum overlaid with the VIP scores can be seen in Figure 2-4.

Table 2-2 PLS-DA model information comparing osteoporotic bone and healthy bone

Model	Components	Sensitivity	Selectivity
Normal vs. Osteoporosis	5	0.941	0.983

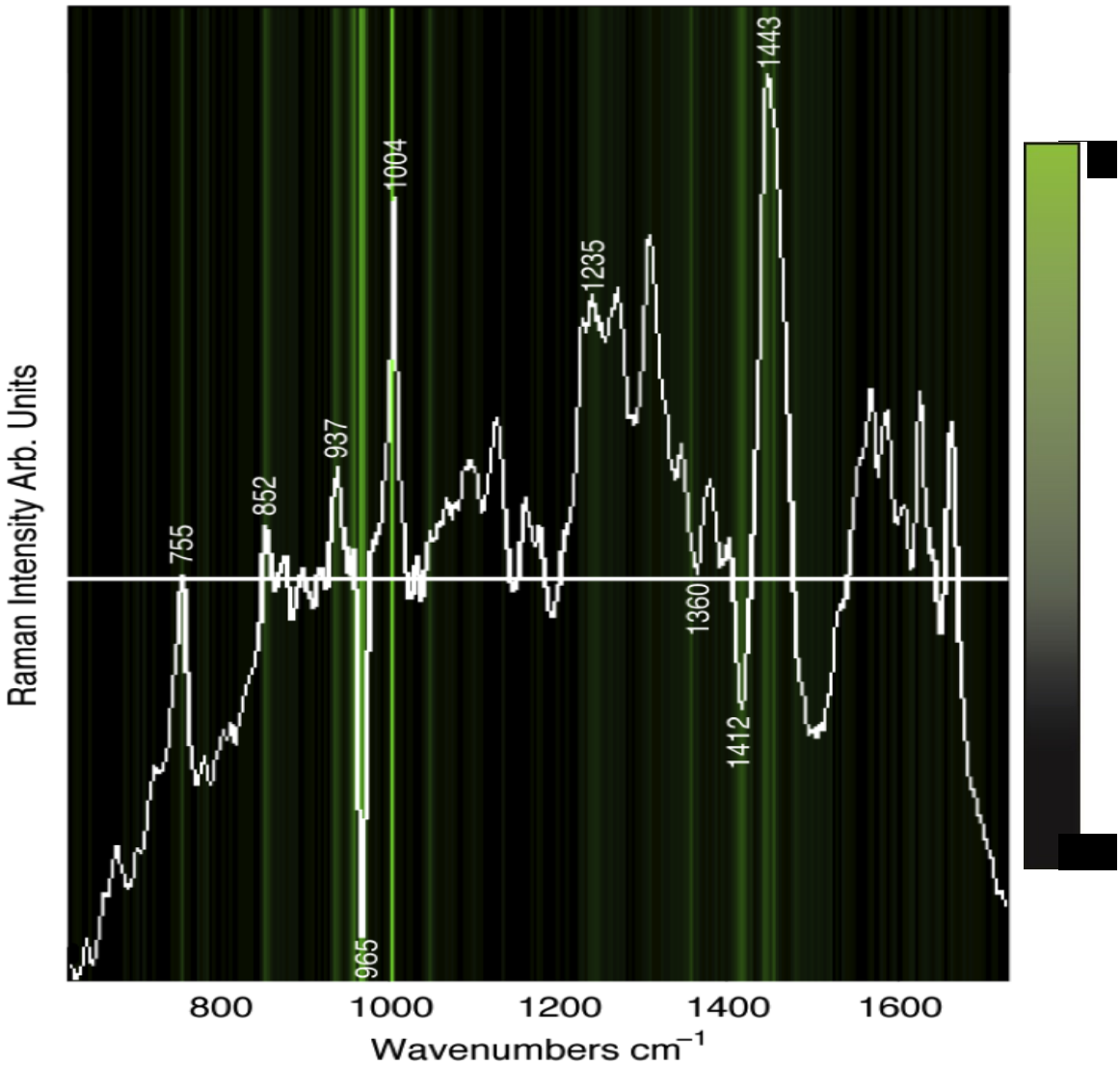

Figure 2-4 Difference spectra of osteoporotic and normal bone spectra overlaid with VIP scores. The brightness of the green background indicate the value of

the VIP scores and thereby the significance of those bands to the PLS-DA model given in Table 2-2.

Figure 2-4 highlights a number of bands that are statically important as determined by the PLS-DA model. The most significant change is in the band shape of the distinct mineral peak at 965 cm^{-1} followed by significant changes in lipid content highlighted by variance in the 1412 and 1443 cm^{-1} band.

In addition there are also visible changes in amino acid signals (Phe: 1004 cm^{-1}, Trp : 755, 1360 cm^{-1} Pro/Trp/Tyr: 852 cm^{-1}) and in the amide III region at 1235-1265 cm^{-1}. Again this example shows that the largest differences in the difference spectrum are not necessarily the most important in discriminating between sample groups.

2.6 Discussion

Unveiling the biological significance behind changes in information rich Raman spectra collected from biological samples can be challenging due to the complex nature of the molecular bonds identified by Raman spectroscopy. This translation however, is critical in applying this powerful non-invasive tool to biological investigations. Raman spectra collected from biological samples include signals from lipids, proteins, carbohydrates and minerals and details of their environmental influence on each other.

Introduced here is a novel way of using PLS-DA VIP scores to visually highlight the significant differences between biological Raman datasets. The usefulness of this analysis is presented using two very different biological systems, one comparing cultured HeLa single cells in their live, fixed, fixed and ethanol dehydrated and fixed, dehydrated and rehydrated forms, and the other comparing normal and osteoporotic human bone tissue.

The PLS-DA VIP scores highlighted Raman spectral ranges, which distinguished between HeLa cells depending on their experimental state. When comparing live HeLa cells to fixed HeLa cells, changes in spectral bands corresponding to differences in lipid composition (877, 935, 983, 1335 and 1370cm^{-1}) due to the crosslinking of phospholipids (720, 1092cm^{-1}) and however no significant change in protein structure was resolved by Raman spectroscopy. It is well reported in previous studies on formaldehyde fixation that proteins are well preserved in the fixation process and

lipids may be altered or lost [107,108]. In the cases of fixed HeLa cells vs. dehydrated HeLa cells and dehydrated HeLa cells vs. rehydrated HeLa cells, the main changes in the molecular structure are due to the unfolding and refolding of proteins resulting in exposure of phenylalanine and breaking and reformation of β-sheets and α-helices. Although fixation preserves protein structure, dehydration and rehydration do have an effect on protein structure as seen in our results. The VIP scores highlight the statistically important differences quickly and clearly identify specific bands and peaks of significance.

In the study comparing human osteoporotic bone vs. healthy bone, the changes observed when comparing these bone samples were mostly in the mineral composition where the osteoporotic bone shifts towards lower wavenumbers suggesting a slightly more amorphous structure, which may be due to both osteoporosis and a general trend of bone compositional differences between male and female patients [109]. In addition the most significant bands highlighted are related to protein composition with changes in Phe: 1004 cm^{-1}, Trp : 755, 1360 cm^{-1} Pro/Trp/Tyr: 852 cm^{-1}) and in the amide III region at 1235-1265 cm^{-1}. Protein changes observed in the distinction between osteoporotic bone and healthy bone may be due to the protein changes previously demonstrated to occur in osteoporotic bone microstructure. It has been shown that the quality of collagen within the bone matrix changes with age and osteoporosis. Oxlund et al. suggested a reduction of the concentration of collagen reducible cross-links in osteoporotic bone however not necessarily a change in the amount of collagen [109]. The model's ability to distinguish between the osteoporotic bone and healthy bone may not be exclusively caused by osteoporosis, as this could be due to multiple factors such as age, bone remodelling, and/or sex differences [110,111]. As these changes are well reported in literature, the comparison shown here is a proof of concept for the combination of PLS-DA VIP scores overlay on difference spectra and for the ability to apply this analysis in conjunction with the non-invasive imaging power of Raman spectroscopy. To fully distinguish molecular environments between osteoporotic and healthy bone samples in a Raman study, more samples, control measures and spectral pre-processing would ideally be incorporated.

In all cases the absolute intensity of the difference spectra is not necessarily indicative of the importance of those bands as a distinguishing factor between groups. Due to the semi-quantitative nature of Raman spectroscopy, the difference spectra are best

utilised as indicators of potential trends molecular distinction between sample groups describe peak shifts or band shape changes. Combined with PLS-DA VIP score plots, Raman spectral band ranges of interest are identified and the band shape or position changes eluded to by the difference spectrum exposes the nature of the change which differentiates trial groups.

2.7 Conclusions

In conclusion, PLS-DA VIP scores was applied to highlight significant chemical differences in biological spectra in two separate investigations, one comparing single cells tested in their live, fixed, fixed and dehydrated versus fixed, dehydrated and rehydrated forms respectively and the other comparing human osteoporotic bone and healthy bone. Applying PLS-DA VIP scores was critical and presented a visually accessible method to highlight the biomolecular bonds which distinguish one sample group from another in the *in vitro* cellular study and suggested the possibility of distinction between experimental groups in the human tissue study (more samples are required to confirm the differences highlighted). This visualisation helped in translating the changes observed to the biological differences between the sample groups. This new analytical tool may find great applications across a wide breath of future Raman spectroscopic studies of biosystems.

2.8 Future Work

The statistical algorithms used in this study have been applied to other biologically relevant studies which produce high dimensional data. Many of these studies include the 'omics-type data (genomics, proteomics, metabolomics, etc.) where a limited amount of samples are being analysed with thousands of features under consideration. This complicates analysis and gives rise to known issues such as data over-fitting and multicollinearity [42]. PLS regression is a predictive technique which allows for the modelling of multiples responses while dealing with multicollinearity. PLS VIP scores have been applied to studies where there are many more features than observations and the objective is to determine which variables are important. An example study can be found in Xia and Wishart's study providing comprehensive analysis of quantitative metabolomics data and ranking compound of interest based on their VIP scores [101]. It is advantageous to use these methods not only because they confront issues commonly found in biologically relevant studies, but also because the analysis is then interpretable to members of different disciplines. The VIP score heat map plots shown in this study introduce another way to visualise this

information providing an overview of all spectral regions and not just those with the highest VIP scores. In future studies with larger datasets it would be very interesting to see how the VIP scores evolve and which factors remain, gain, or lose importance.

This study applied PLS-DA VIP scores to two bio-spectroscopic datasets to highlight the possible advantages of both using the VIP scores and applying them displaying the variables highlighted in a heat map fashion. The tissue data used here was from two patients, one with osteoporosis and one without. The limited number of patients in this dataset leads to limitations in the confidence of these results. There are many factors which could alter the bone composition of one individual versus another and more patients would be hugely advantageous in confirming the application of these statistical techniques. In chapter 4 these techniques were used on cardiovascular tissue in a study incorporating more donors.

Further studies using larger datasets of live cells in vitro may allow for threshold limits to be set. Limits could be applied to determine if a peak or band is significantly changing in the system in relationship to the experimental factors or because the peaks/bands shift significantly independent of experimental factors. This study used experimental conditions with known consequences as fixation and dehydration of biological tissues and cells has been widely studied. In future further studies where the differences are not as widely reported, limits and thresholds could be very significant in determining analytical results.

Raman spectroscopy can expose critical differences in protein, DNA, lipids and biological mineralisation. The rich data collected from Raman gives it great potential with the obstacles of finding appropriate analytical techniques to harness the high dimensional datasets. Studies such as the one presented here offer tools to ease the translation of complex analysis into biologically relevant results and can be applied to many future investigations.

3 Characterization of Porcine Aortic Valvular Interstitial Cell 'Calcified' Nodules

3.1 Abstract

Valve interstitial cells populate aortic valve cusps and have been implicated in aortic valve calcification. This study focused on investigating a common in vitro model for aortic valve calcification by characterizing nodule formation in porcine aortic valve interstitial cells (PAVICs) cultured in osteogenic medium (OST) supplemented with transforming growth factor beta 1 (TGF-β1). Using a combination of materials science and biological techniques, the relevance of PAVICs nodules in modeling the mineralised material found in calcified aortic valve disease was studied. PAVICs were grown in OST medium supplemented with TGF-β1 (OST+TGF-β1) or basal (CTL) medium for up to 21 days. Murine calvarial osteoblasts (MOBs) were grown in OST medium for 28 days as a known in vitro mineralizing model for comparison. Cultured PAVICs grown in OST+TGF-β1 produced nodular structures staining positive for calcium content. Micro-Raman spectroscopy allowed live, non-invasive imaging that showed an absence of mineralized material within these nodules, which was readily identified in nodules formed by MOBs and in diseased human aortic valves. Gene expression analysis, immunostaining, and transmission electron microscopy imaging revealed that PAVICs grown in OST+TGF-β1 medium produced abundant collagen rich extracellular matrix via the up regulation of the gene for Type I Collagen. PAVICs, nevertheless, did not appear to further transdifferentiate to osteoblasts. 'Calcified' nodules formed from PAVICs do not mineralize after 21 days in culture. PAVICs nodules do however, express a myofibroblast-like phenotype and produce a collagen-rich extracellular matrix. This study clarifies further the role of PAVICs as a model of calcification of the human aortic valve highlighting a significant consideration when investigating the mineralizing stage of aortic valve calcification.

3.2 Introduction

The aortic valve performs a number of sophisticated functions including critical regulation of unidirectional oxygenated blood flow from the heart to the rest of the body [112,113]. The maintenance of these continuous functions is highly dependent on the unique structure of the valve at the tissue, cellular and molecular levels [114].

Aortic valve calcification, a disruption to the intricate structure of the valve through the accumulation of mineral deposits in the valve tissue cusps, leads to considerable morbidity and mortality globally. The disease increases in prevalence with age [115], and will continue to increase as the world's population ages [116]. Currently, there is no proven pharmacotherapy to prevent or manage aortic valve calcification progression. The treatment of choice for aortic valve calcification, therefore, is to surgically repair or replace valves with bioprosthetic or mechanical alternatives [117-119] and is associated with many complications including progressive calcification of the replacement valve. Pharmacotherapies that prevent native and prosthetic valve calcification remain elusive, partially due to a lack of understanding of the pathophysiological mechanisms that regulate disease progression and the lack of a proven *in vitro* disease model [114,120,121].

Valvular Interstitial Cells (VICs) are the most abundant cell type in the aortic valve and play a vital role in maintaining valve function [69]. VICs comprise of a heterogeneous population of cells consisting of embryonic progenitor, endothelial/mesenchymal, progenitor, quiescent (fibroblasts), activated (myofibroblasts) and osteoblastic phenotypes [58,69,74,79], which are thought to play a role, either alone or collectively, in the process of calcification [58,122]. Several studies have suggested that VICs may transdifferentiate to bone-forming cells and directly mediate the formation of calcified mineral deposits, in a process analogous to bone formation [115,117,123]. Additionally VICs have been implicated in a dystrophic calcification through VICs activation in combination with apoptotic events resulting in calcium salt deposition [124].

VICs derived from porcine tissue (PAVICs) are often used as a model for aortic valve research, as the fast-growing, relatively inexpensive and readily available cells can be cultured *in vitro* [82]. PAVICs have been reported to be a particularly valuable model in aortic valve calcification studies, as distinct cellular nodules spontaneously form in culture in the presence of control medium and osteogenic medium supplemented with transforming growth factor beta 1 (TGF-β1) [82,124]. TGF-β1 has been implicated in the pathobiology of aortic valve stenosis and shown to co-localize with calcification in diseased aortic tissue cusps [124,125]. Cellular nodules formed in the presence of TGF-β1 *in vitro* have been referred to in the literature as 'calcifying nodules' [124,126]. Nevertheless, a relationship between *in vitro* nodule formation and pathological aortic valve calcification has not been clearly established, and the cellular

composition and nature of the material that comprises these nodules has yet to be determined. The hard material that accumulates within human calcified valves has been identified as a mixture of calcium phosphate phases [127-129], thus similar mineral species should be identifiable in a cell-mediated model of aortic valve calcification. The calcified material found in diseased human valves has been suggested to be a result of an osteoblast like mineralization process and/or via a dystrophic calcification mechanism [48,123].

This chapter describes the characterisation of PAVICs *in vitro* nodules grown in osteogenic (OST) medium supplemented with TGF-β1 (OST+ TGF-β1) through a series of biological and materials-based characterization of the internally produced extracellular matrix (ECM). This information was used to compare these materials to those found within nodules formed by mineralizing murine calvarial osteoblasts (MOBs) and to PAVICs maintained in basal (CTL) medium. To do this, a myriad of techniques were utilized including a combination of gene expression, immunohistochemistry, histochemical staining, scanning electron microscopy (SEM), transmission electron microscopy (TEM), and live cell bio-molecular analysis with micro-Raman spectroscopy. Raman spectroscopy is a rapid, non-invasive technique based on light scattering which reveals the molecular fingerprint of a sample without dyes or labels. Micro-Raman spectroscopy additionally enables a more specific visualization of calcium salt deposition when compared to traditionally used Alizarin Red S and detects the presence of any calcium phosphate inclusion within the PAVICs nodules regardless of an osteoblast-like or dystrophic deposition [130,131]. The results presented in this chapter suggest that PAVIC nodules grown in OST+TGF-β1 for up to 21 days show no evidence of calcium phosphate formation and showed no indication of undergoing an osteoblastic differentiation, however these nodules do produce an abundant ECM which is predominately collagen including type I collagen.

3.3 Methods and Materials

This study was reviewed and approved by the North London Research Ethics Committee (reference # 10/H0724/18), registered with the Royal Brompton & Harefield NHS Foundation Trust and performed in accordance with the requirements of the research governance framework.

3.3.1 VICs Isolation

Whole hearts from 18 to 24 month old pigs were obtained from an abattoir (Cheale Meats, Essex, U.K.). Aortic valve cusps were removed within 12 hours of slaughter and PAVICs were isolated through two collagenase digestions as previously described [82]. Some PAVICs utilised were isolated by Ismail El-Hamamsy.

3.3.2 Cell Culture and Tissue Collection and Preparation

PAVICs were cultured in CTL medium consisting of high glucose Dulbecco's Modified Eagles Medium (DMEM) supplemented with 1% (v/v) antibiotic–antimycotic, 10% (v/v) fetal bovine serum (FBS), and 2 mM L-Glutamine (All Invitrogen). OST+TGF-β1 medium consisted of CTL medium supplemented with 10 mM β-glycerophosphate, 10^{-7}M dexamethasone, 10^{-6}M ascorbic acid, and 10 ng/mL TGF-β1 (all Sigma-Aldrich). Media was replenished every three days. CTL+TGF-β1 medium consisted of CTL medium supplemented with 10 ng/mL TGF-β1. OST medium consisted of CTL medium supplemented with 10 mM β-glycerophosphate, 10^{-7}M dexamethasone, and 10^{-6}M ascorbic acid. MgF_2 coverslips (micro-Raman spectroscopy), glass cover slips (histology) and tissue culture plastic were seeded with 5 x10^4 cells/cm^2 at passages four or five. Prior to cell seeding, MgF_2 and glass cover slips were incubated in FBS for 6 hours.

MOBs were enzymatically derived from the calvaria of neonatal mouse pups as previously described [132] and performed by Dr. Eileen Gentleman. To form mineralized nodules, cells were cultured in alpha minimum essential medium (Invitrogen) supplemented with 15% (v/v) FBS, 2mM L-glutamine, 10mM β-glycerophosphate, 50μg/ml ascorbic acid and 10^{-6} M dexamethasone from day 14. All MOBs were at passages two to four during testing.

Calcified human aortic valves were obtained from the Royal Brompton Hospital, London, U.K. A total of four patients were included in this investigation at ages 51, 55, 63 and 81 years old. After collection each cusp was isolated, fixed in 4% (w/v) formaldehyde (FA) for 48 hours at 4°C and then rinsed in phosphate buffered saline (PBS). The cusps were then dehydrated in a graded ethanol series and calcified tissue was isolated for testing. Raman spectra were collected from dry isolated human aortic valve cusp calcified tissue at room temperature with 3 accumulations of 5 second scans covering the Raman shifts range of 618-1728cm^{-1}.

3.3.3 PAVICs Nodule Cross Section Preparation for Histology

After 7, 14 and 21 days, cultures were fixed in 4% (w/v) formaldehyde (FA) for 20 minutes at room temperature and then rinsed in phosphate buffered saline (PBS). For histological sectioning, cells were carefully scraped from the culture surface using a rubber policeman and re-suspended in a 1% (w/v) agarose (Sigma) in PBS using the method described by Gruber *et al*. [133]. Agarose gels containing VICs were again fixed in 4% (w/v) FA for 1 hour, dehydrated in a graded ethanol series and embedded in paraffin. 5μm sections were collected on glass slides and prepared for staining.

3.3.4 Modified Verhoeff van Gieson for Detection of Collagen, Elastin, Muscle and Cell Nuclei

Samples were stained using an elastin stain kit (Sigma) which utilizes the modified Verhoeff van Gieson method to stain elastic fibres blue-black to black, collagen pink to red, muscle yellow and nuclei blue to purple. Sections from blood vessels of adult mice were used for a positive control.

3.3.5 Immunoperoxidase for Detection of Smooth Muscle Alpha Actin (aSMA)

Prior to immunoperoxidase staining, sections were dewaxed, rehydrated in nanopure distilled water (dH2O) and washed in PBS for 5 minutes. Slides were immersed in 0.1M citrate buffer (pH 6) and microwaved for 10 minutes before being immersed in peroxide (0.01% w/v) in PBS for 10 minutes. Sections were then washed 3 times for 5 minutes each in PBS and blocked with 3% (w/v) bovine serum albumin (BSA) in PBS for 30 minutes. Sections were incubated separately for 1 hour with primary antibodies (Sigma).

Sections were incubated with biotinylated goat anti-mouse immunoglobulins (GAM IgG-Vector laboratories) for 1 hour, washed 3 times in PBS and then incubated for 1 hour with Avidin-Biotin Complex (ABC-Vector laboratories). Reactivity was detected using diaminobenzidine tetrahydrochloride (DAB tablets- Sigma) (25mg/ml) and hydrogen peroxide (0.01% w/v). Sections were then counter stained with haematoxylin.

3.3.6 Immunostaining for aSMA and DNA

Sections were dewaxed and rehydrated in dH20. Antigen retrieval was carried out by immersing slides in 0.1M citrate buffer (pH 6), placing in a microwave for 10 minutes, incubating in citrate buffer for a further 20 minutes, and rinsing with tap water. To reduce non-specific binding, slides were incubated with 3% (w/v) BSA for 30 minutes. Specimens were then incubated with a smooth muscle alpha actin (αSMA) antibody (DAKO) for 1 hour at room temperature. Negative controls were incubated with 3% (w/v) BSA in PBS. After thorough washing, sections were incubated with goat anti mouse (IgG) Alexa Fluor 594 (Invitrogen) for 1 hour. After washing twice with PBS, cells were stained with DAPI and specimens mounted using Permafluor (Beckman Coulter).

3.3.7 Alizarin Red S Staining for Calcium Detection

Cultures were fixed in 2% (v/v) FA for 10 minutes, washed in dH20 and stained for 10 min in 2% (w/v) Alizarin Red S (ARS) (Sigma) in dH2O, rinsed again, air dried, mounted on glass slides using DPX mounting medium and viewed using bright field microscopy.

3.3.8 Gene Expression Analysis for Collagen I and BGLAP

Gene expression analysis was performed after 7, 14 and 21 days in culture by Francesca Colazzo. RNA was extracted using the QIAGEN Mini extraction kit according to the manufacturer's instructions. Reverse transcription (RT) and real-time polymerase chain reaction (PCR) was performed as described [126]. TaqMan assays were purchased for type 1 collagen (*COL1A1*) and bone gamma-carboxyglutamate protein (*BGLAP*) (Ss03373340_m1, Ss03373655_s1) respectively; (Applied Biosystems). Target gene data were normalized against 18S ribosomal RNA levels (Cat. No. 4310893E; Applied Biosystems) and analyzed using the comparative cycle threshold (Ct) method.

3.3.9 Scanning Electron Microscopy (SEM)

Cultures were fixed in 4% (v/v) FA in PBS for 45 minutes at 4°C and dehydrated in a graded ethanol series, followed by critical-point drying with hexamethyldisilazane (Sigma). Samples were sputter-coated with gold and viewed using a Leo 1525 Gemini scanning electron microscope with an EDX detector (Carl Zeiss SMT Ltd.) operated at 15 kV.

3.3.10 Transmission Electron Microscopy (TEM)

TEM sample preparation and imaging was performed by Suwimon Boonrungsiman. Cultures were fixed in 4% (v/v) glutaraldehyde in 0.1 M PIPES buffer (pH 7.4) at 4˚C for 2 hours and then fixed in 1% (w/v) osmium tetroxide in 0.1M PIPES buffer at room temperature for 1 hour. The samples were then dehydrated using a graded ethanol series from 50%, 70%, 90% and 100 % (v/v), followed by immersion in acetronitrile. The nodules were then progressively infiltrated with a Quetol based resin (12.6g Quetol, 15.5g Nonenyl succinic anhydride (NSA), 6.5g Methyl nadic anhydride (MNA) and 0.6g Benzyl dimethylamine (BDMA)) with ratio of 1:1, 3:1 (resin: acetonitrile) and pure resin for 2 hours, overnight and 4 days, respectively. Pure resin was changed every 24 hours. Embedded samples were polymerized at 60˚C for 24 hours. 70 nm thick sections were cut onto a water bath via ultramicrotomy. The sections were collected immediately on bare 300 mesh copper TEM grids; selected sections were post-stained with uranyl acetate and lead citrate. TEM was performed on the Joel 2000 operated at 120 kV.

3.3.11Raman Spectroscopy

Live cell spectra were collected with a 785nm laser, using a Renishaw InVia spectrometer connected to a Leica microscope as previously described [12]. Briefly, spectra were collected from live cell cultures maintained at 37°C in PBS supplemented with Mg and Ca. Spectra were collected over 5 accumulations of 3 second scans covering the Raman shifts range of 800-1800cm^{-1}. Samples were kept outside the incubator during testing for no longer than 30 minutes.

Raman spectra were pre-processed for background removal (baseline subtraction using weighted least squares) and multiplicative scattering correction [134,135]. Interval partial least squares discriminate analysis (iPLS-DA) was applied to determine if a model could distinguish between treatment groups [136]. This model was derived using 194 total spectra collected from PAVICs nodules grown for 21 days in CTL or OST+TGF-β1 media.

For mapping of PAVICs nodules, cultures were fixed in 4% (v/v) FA in PBS for 45 minutes at 4°C and dehydrated in a graded ethanol series. Raman spectra were collected using a 532nm laser, on a Renishaw InVia spectrometer connected to a Leica microscope using a 60x (NA=1.0) long working distance (2mm) water immersion

objective (Nikon, U.K.). Spectra were collected using 1 accumulation of 10 seconds covering the Raman shifts range of 670-1500cm^{-1}.

Raman spectra of human valves were processed and analysed with software developed internally, including scripts written by Dr. Martin AB Hedegaard, for use with Matlab (The Mathworks) environment and with the multivariate statistical analysis PLS toolbox (Eigenvector Research) as described in chapter 1. Raman spectra were intensity-corrected for instrument response; background signals were subtracted using the Modpoly algorithm (5th order polynomial, 1000 iterations) and lightly smoothed using a 5-point Savitsky-Golay filter (2nd order polynomial) as previously described [29].

3.3.12 Statistical Methods

All continuous data are presented as mean ± one standard deviation. For RT-PCR, all data were compared using the Mann-Whitney test for statistical significance. *p*-values < 0.05 were considered significant.

3.4 Results

3.4.1 PAVICs Grown in OST+TGF-β1 Media Form Nodular Structures and Stain Positive for ARS

VICs cultured in CTL and OST+TGF-β1 media for 21 days produced distinct, dense nodules approximately 50-200 μm in diameter (Figure 3-1A and D, respectively) with nodule formation occurring as early as day 4 in culture. Whilst nodules formed in CTL medium were visibly distinguishable from the surrounding monolayer, those formed in OST+TGF-β1 medium were more raised from the culture surface and appeared more compact. Nodules were similar in gross appearance to those formed from MOBs (Figure 3-1G). Nodules formed from PAVICs grown in OST+TGF-β1 media stained positively for ARS, a calcium stain, after 21 days in culture (Figure 3-1E). Nodules formed in CTL medium did not stain positively for ARS (Figure 3-1B), whilst MOBs nodules did (Figure 3-1H). SEM images demonstrated that nodules formed from PAVICs cultured in OST+TGF-β1 medium produced distinct three-dimensional morphologies (Figure 3-1F), whereas nodules formed in CTL medium appeared as dense areas of cell growth with a less raised profile from the cell monolayer (Figure

3-1C). Nodules formed from MOBs had similar three-dimensional morphologies to those observed in the PAVICs cultures grown in OST+TGF-β1 medium (Figure 3-1I).

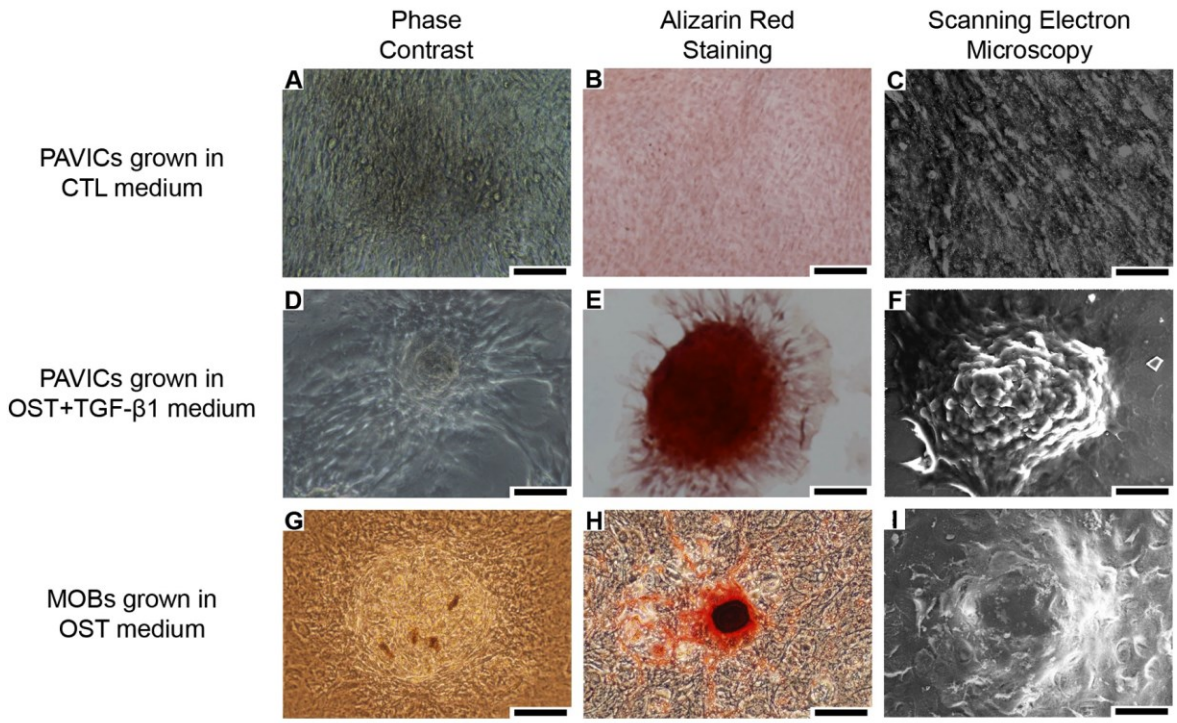

Figure 3-1 Phase contrast and SEM images of cultured PAVICs and MOBs. A,D,G - Phase contrast images of cultured PAVICs grown in CTL medium for 21 days, PAVICs grown in OST+TGF-β1 medium for 21 days, and MOBs grown in OST medium for 21 days respectively (scale = 100 μm). B,E,H - Alizarin Red S staining negative for PAVICs grown in CTL medium for 21 days, positive for PAVICs grown in OST+TGF-β1 medium for 21 days, and positive for MOBs grown in OST medium respectively (scale = 100 μm). C,F,I - SEM images of cultured PAVICs grown in CTL medium for 21 days, PAVICs grown in OST+TGF-β1 medium for 21 days, and MOBs grown in OST medium for 21 days respectively (scale = 50 μm).

3.4.2 PAVICs Grown in OST+TGF-β1 Medium Show an Increase in Type I Collagen Expression

PAVICs grown in OST+TGF-β1 media showed a significantly higher expression of collagen type I after 14 and 21 days in culture compared to the expression levels after 7 days (p<0.05) and to PAVICs cultured in CTL medium at the same time points (p<0.05, Figure 3-2a). PAVICs grown in CTL medium also showed no changes in type I collagen expression at any of the three time points examined.

*BGLAP (*osteocalcin) was stably expressed in PAVICs grown in OST+TGF- β1 or CTL media, however, its expression was significantly lower (p<0.05) in cells cultured in OST+TGF-β1 medium when compared to cells grown in CTL medium after 7, 14 and 21 days, (Figure 3-2B).

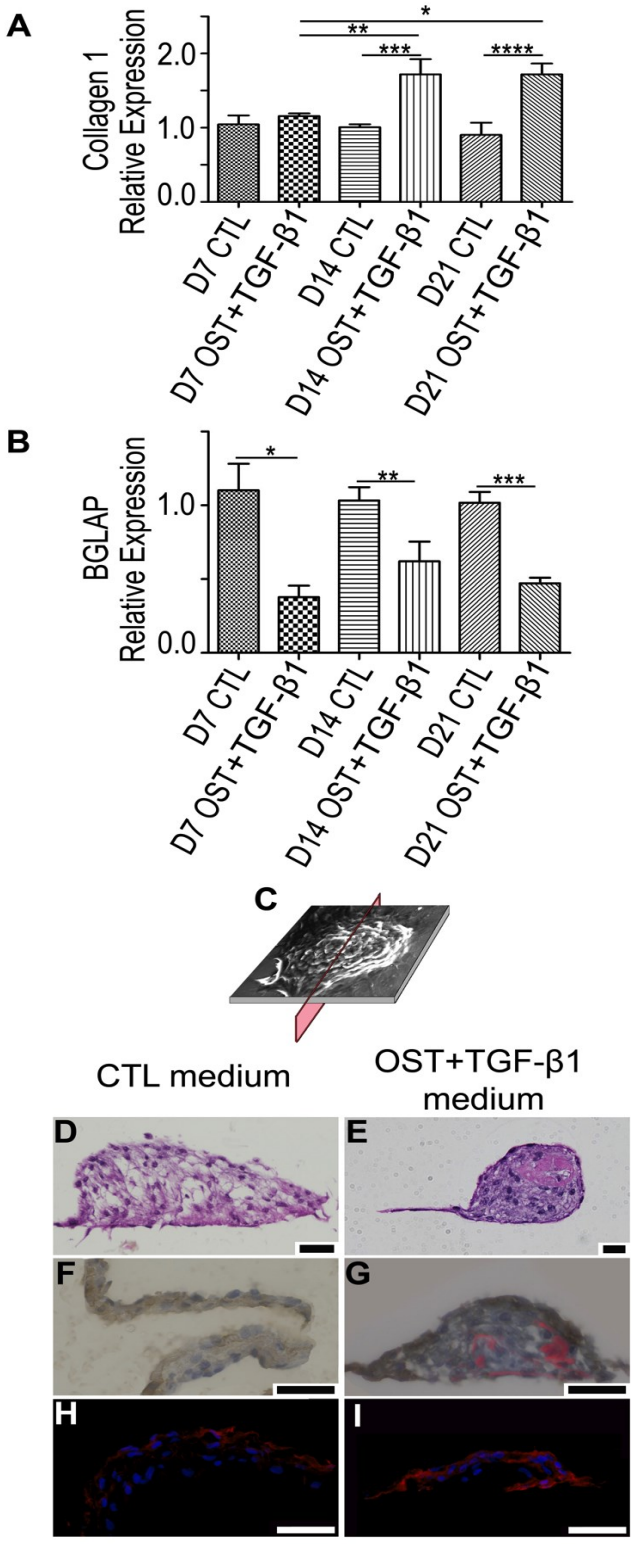

Figure 3-2 Gene expression and staining of PAVICs nodules. A - Gene expression of collagen I (* = p < 0.05, ** = p< 0.0001, *** = p< 0.05;** = p< 0.001) and B - Osteocalcin (bone gamma-carboxyglutamate protein (BGLAP)) (*= p < 0.05; ** = p< 0.001; *** = p< 0.0001) comparing PAVICs expression at day 7 (D7), day 14 (D14), and day 21 (D21) in both OST+TGF-β1 and CTL media. C – Cross sectional plane of cultured nodules used for the D,E,F,G,H, and I. D,E - Modified Verhoeff**

van Gieson stain [purple – cell nuclei, pink – collagen, black-elastin] of a cross section of PAVICs cultured in CTL media for 21 days and PAVICs cultured in OST+TGF-β1 media for 21 days respectively (scale = 50 μm). F,G - Peroxidase stain with Sirius red staining [brown - αSMA , red – collagen] for PAVICs grown in CTL medium for 21 days and PAVICs grown in OST+TGF-β1 medium for 21 days respectively (scale = 50 μm) H,I - Fluorescence staining [red - αSMA, blue - cell nuclei] of a PAVICs nodule cultured for 21 days in CTL medium and a PAVICs nodule cultured in OST+TGF-β1 medium for 21 days respectively (scale = 50 μm).

3.4.3 OST+TGF-β1 Medium Induces αSMA Expression and Collagen Deposition in PAVICs

PAVICs cultured nodules were cross-sectioned for staining with a graphic showing the selected sectioned plane shown in Figure 3-2C. Modified Verhoeff van Gieson staining and sirius red identified collagen in PAVICs nodules formed in OST+TGF-β1 medium (Figure 3-2E and G, respectively). This was in contrast to nodules spontaneously formed in CTL medium where no collagen deposition was visualized in either the monolayer or nodule cross sections (Figure 3-2D,F). No elastin was observed in PAVICs cultures treated with either CTL or OST+TGF-β1 media. αSMA was present in CTL and OST+TGF-β1 derived nodules and monolayers, however, was not expressed homogeneously throughout the nodules, but rather only in the outermost layers in OST+TGF-β1 nodules (Figure 3-2G,I) and one side of the CTL nodules (Figure 3-2H).

3.4.4 TEM of OST+TGF-β1 PAVICs Nodule Cross Sections Show Abundant ECM and No Evidence of Mineralization

TEM images of PAVICs nodule cross sections showed layered cellular aggregates similar to those identified by histology. PAVICs nodules grown in OST+TGF-β1 medium contained a proteinaceous ECM which was apparent throughout the nodules and surrounding cells (Figure 3-3A). The proteinaceous ECM appeared disorganized and contained fibrous proteins with a banded appearance (approximately 65nm in periodicity) indicative of mammalian collagen, specifically type I collagen [137-139]. PAVICs nodules formed in CTL medium displayed a rough membrane and contained little to no proteinaceous ECM between cells (Figure 3-3B). Electron dense mineral deposits were not evident in any PAVICs cross sections.

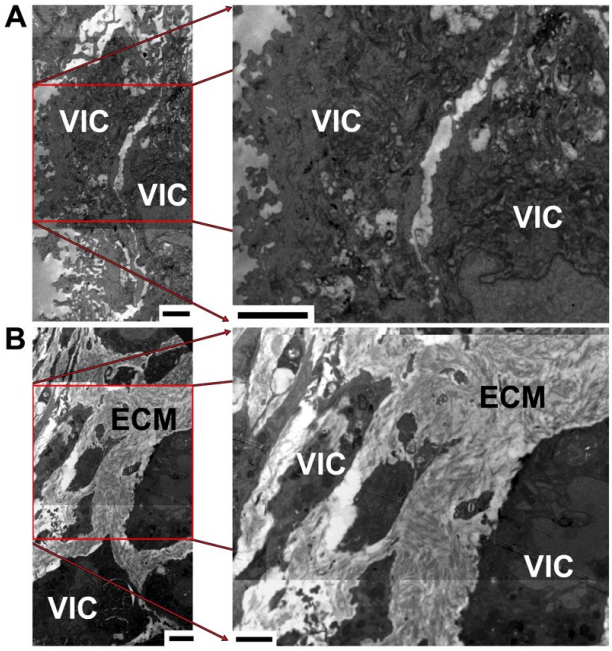

Figure 3-3 Transmission Electron Micrographs of cultured PAVICs grown in A - CTL medium and B - OST+TGF-β1 medium (VIC – valvular interstitial cell, ECM – extracellular matrix) (scale = 2μm).

3.4.5 Raman Spectroscopy Exposes High Protein Content in OST+TGF-β1 PAVICs Nodules Without Any Mineral Presence

Inorganic peaks indicative of mineralization were not present in CTL (day 21), CTL+TGF-β1 (day 14), OST (day 14) or OST+TGF-β1 (day 21) treated PAVIC nodules. In contrast the 960 cm^{-1} and 1070 cm^{-1} mineral peaks identifying the phosphate PO_4 bonds and type B carbonate substitution CO_3 bonds, respectively, are clearly seen in the spectrum collected from an MOB nodule (Figure 3-4A). Raman maps spanning entire PAVICs nodules grown in CTL (day 21), CTL+TGF-β1 (day 14), OST (day 14) or OST+TGF-β1 (day 21) demonstrated a clear absence of mineral throughout the entire area of the nodules imaged as demonstrated in the representative Raman spectrum from each group (Figure 3-5D). The collected Raman maps were successful in imaging the organic area of the nodules through mapping of the phenylalanine peak (Figure 3-5B) when compared to the white light micrograph (Figure 3-5A). No mineral content was visible in maps of these nodules as demonstrated by a representative Raman map in Figure 3-5C. Mineral bands were present in spectra collected from

calcified human aortic valve tissue as seen in the representative mean spectrum (Figure 3-6).

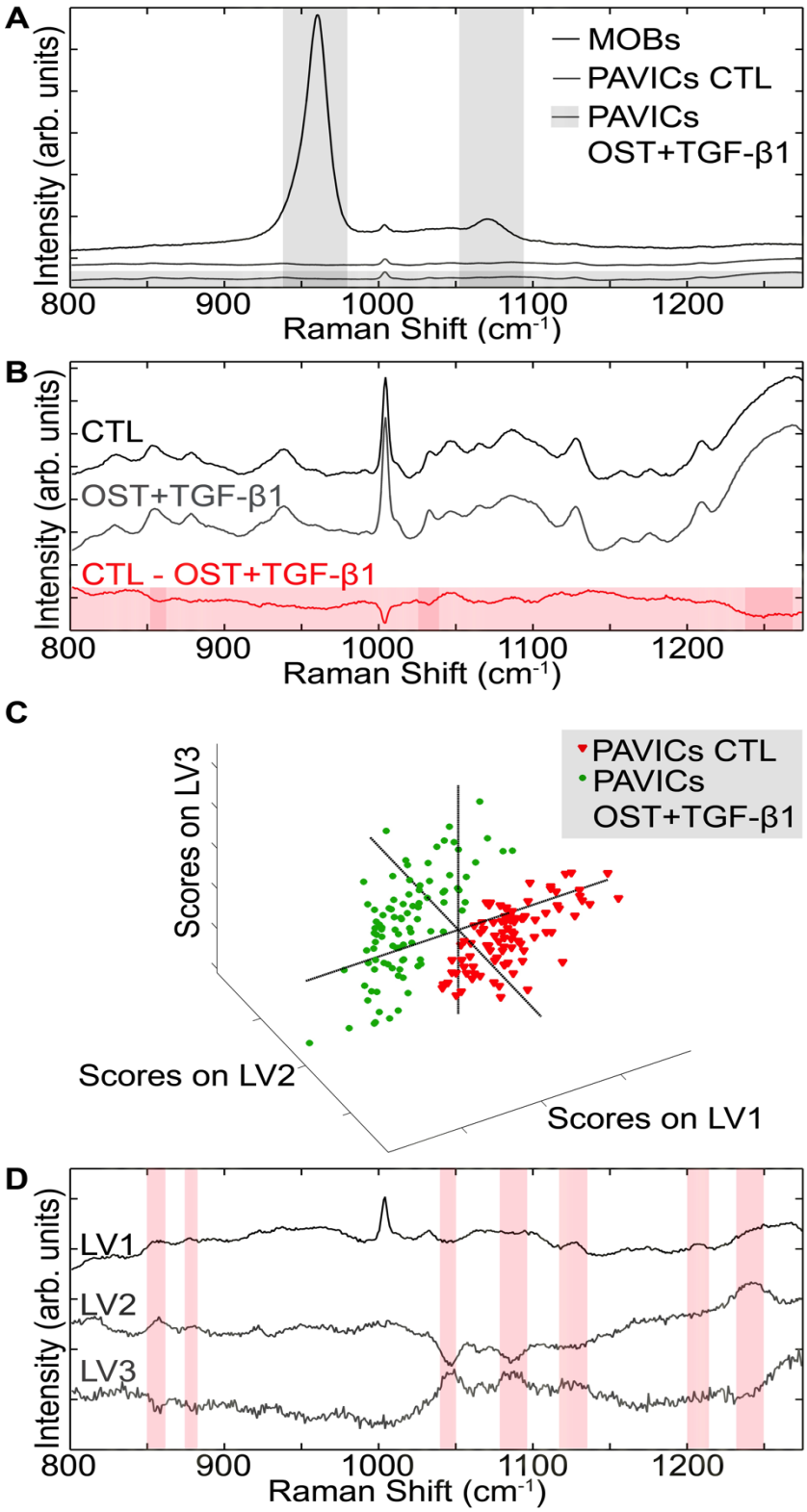

Figure 3-4 Raman spectra and PLS-DA model of cultured PAVICs. A - Raman spectra comparing a representative MOBs mineralized nodule spectrum (black), PAVICs grown in CTL media mean spectrum (dark grey), and PAVICs cultured in

OST+TGF-β1 medium mean spectrum (shaded box over entire spectrum). Vertical shaded areas highlight the 960cm^{-1} apatite peak and the 1070 cm^{-1} carbonate peak spectral range. B - Higher magnification of the PAVICs mean spectrum grown in CTL (dark grey) and in OST+TGF-β1 medium (light grey). The red spectrum is the difference between the two PAVICs mean spectra. Shaded red bands highlight spectral ranges which discriminate between groups. C - Scatter plot showing group separation between PAVICs grown in CTL medium (red triangles) vs. PAVICs grown in OST+TGF-β1 medium (green circles). D - Latent variables loadings used in the interval partial least squares discriminant analysis (iPLS-DA) model, bands highlighted are spectral ranges which contributed to the distinction between groups.

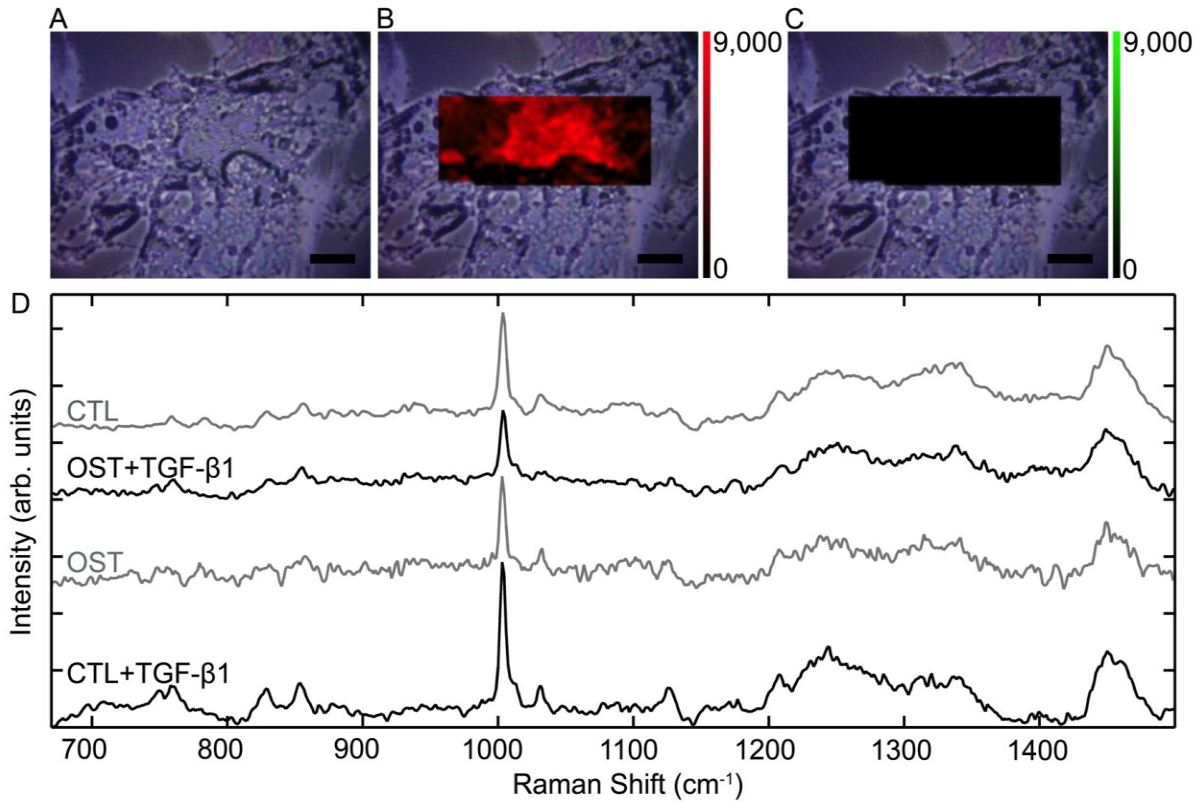

Figure 3-5 Raman mapping of cultured PAVICs nodules. A - White light micrograph of PAVICs grown in CTL+ TGF-β1 (scale = 20μm). B - Overlay of a Raman map (step size 1 μm in the x and y direction) of the phenylalanine peak onto the white light micrograph in A, showing the cellular presence as seen within the collected Raman spectra (scale = 20μm). C - Overlay of the apatite peak Raman map onto the white light micrograph in A showing no mineral was detected in any of the mapped area (scale = 20μm). D - Representative Raman spectra from Raman maps of PAVICs nodules grown CTL medium for 21 days, OST+TGF-β1 medium for 21 days, OST medium for 14 days and CTL+TGF-β1 for 14 days. The phenylalanine (1003cm^{-1}), amide III (1214-1270cm^{-1}), and CH_2 bending (1445cm^{-1}) peaks clearly identified cellular areas within the Raman maps. The absence of mineral peak, including the 960cm^{-1} apatite and 1070cm^{-1} carbonate peak show that there is no mineral presence within these nodules, and mineral associated peaks were not seen in any spectra collected from the PAVICs.

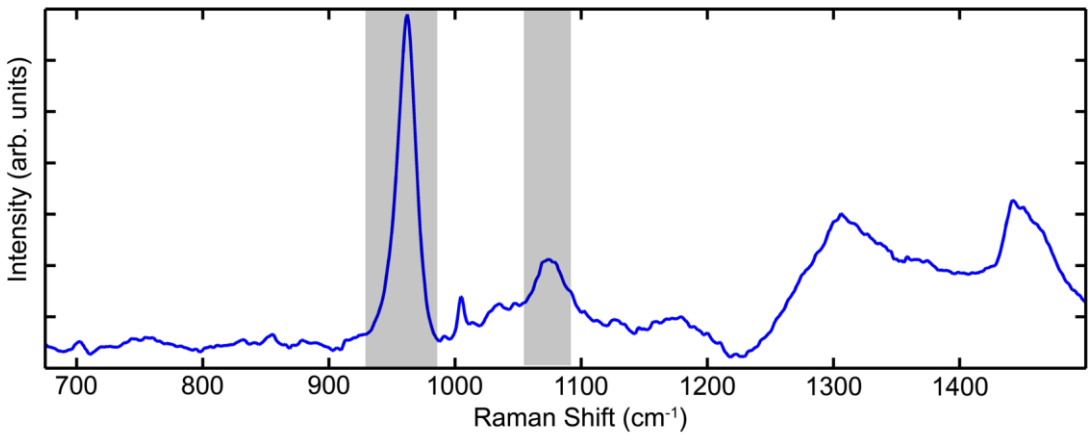

Figure 3-6 Mean Raman spectrum of 128 spectra collected from independent locations within calcified human aortic valve tissue (isolated from 4 separate donors). The grey bands highlight the mineral peaks present within the collected spectra at 960cm^{-1} (apatite) and 1070cm^{-1} (carbonate peak).

The difference spectrum between CTL and OST+TGF-β1 (red spectrum in Figure 3-4B) reveals that protein bonds contributed the majority of the difference between the groups. Specifically, bands at 855, 874, 1043 and 1245-1270 cm^{-1} corresponding to C-C stretch proline, C-C stretch hydroxyproline, proline and Amide III, respectively, are notable. The hydroxyproline and two proline peaks identified in these spectra are specifically Raman collagen assignments [140] confirming a collagen presence within the PAVICs grown in OST+TGF-β1 medium.

The unsupervised technique of principal component analysis (PCA) was performed and although some experimental grouping was observed there was not sufficient information to distinguish experimental groups confidently from one another. For this reason supervised techniques were incorporated to discriminate between the experimental groups.

The iPLS-DA model derived from spectra collected from PAVICs nodules grown in CTL or OST+TGF-β1 media for 21 days identified three latent variables which differentiate between the two groups with an equal sensitivity and specificity of 0.979. A clear division emerged between PAVICs grown in CTL and OST+TGF-β1 media, as is evident in the scatter plot which identifies the loadings of each collected spectra (Figure 3-4C). The latent variables used in the iPLS-DA model are also shown in Figure 3-4D. These variable loadings show spectral regions which varied between the experimental

groups. The latent variables are shown with highlighted bands indicating spectral regions which highly contributed to the differentiation between experimental groups. Specifically, bands at 855, 874, 1032, 1206, 1247 and 1665cm^{-1} are collagen assignment groups. Table 3-1 lists all bands (mineral and organic) highlighted in both the univariate and multivariate Raman analysis with their corresponding assignments.

Table 3-1 Raman bands contributing to univariate and multivariate distinction between PAVICs grown in OST+TGF-β1 media, CTL media and MOBs mineralized nodules. Inorganic peaks are in shaded rows. Stars indicate collagen assignments.

Peak position (cm^{-1})	Major Assignments
855	C-C stretch, proline*
874	C-C stretch, hydroxyproline*
960	Apatite - PO_4^{3-} ν_1 symmetric stretch
1003	Phenylalanine ring breathing mode
1032	Proline *
1043	Proline*
1070	Carbonate - substituted CO_3^{2-} ν_1 in-plane vibrations
1086	C–N stretching mode of proteins (and lipid mode to lesser degree)
1128	C-N
1206	Hydroxyproline , tyrosine*
1247-1270	Protein amide III band
1,595–1,720	Amide I (C=O stretching mode of proteins, a-helix conformation)/C=C lipid stretch

3.5 Discussion

The underlying mechanism of heart valve calcification has been likened to that of bone formation and/or a dystrophic process which includes the deposition of hydroxyapatite mineral [48,115,127,141]; nevertheless the process which mediates the formation of calcified lesions on aortic valve cusps remains uncertain and under investigation. Researchers have speculated that valve calcification involves a transdifferentiation of VICs into osteoblasts, which then mediate bone-like mineral formation within the valve tissue, starting in the collagen rich fibrosa layer [117,141,142]. The implication of such an osteoblast-like mineralization process has prompted the development of calcified *in vitro* models to examine the disease process. Easily cultured and fast-growing PAVICs are often used as a simplified model for aortic valve calcification [82], however, their efficacy in representing the disease and

ability to yield disease like materials has yet to be established. This study aimed to characterize the 'calcified' OST+TGF-β1 PAVICs nodule composition, compare them to those created by a confirmed mineralizing culture model (MOBs), and report any calcium phosphate deposition within the PAVICs nodules.

It was observed that PAVICs grown in OST+TGF-β1 medium formed nodular structures which stained positively for ARS, as has been previously described [124,143]. Such nodules were notable for their distinct three-dimensional morphologies that are reminiscent of nodules formed from MOBs, which also stained positively for ARS. Nevertheless, when examining the ultrastructure of such nodules by TEM, no electron-dense mineral deposits were observed, as were readily identifiable and described in the previously published report of nodules formed from MOBs [12]. Furthermore, Raman spectroscopy measurements clearly showed an absence of mineralization in the OST+TGF-β1 PAVICs, whilst MOBs nodules demonstrated distinct mineral peaks, indicative of phosphate and type-B carbonate-substitution. These results suggest PAVICs 'calcified' nodules do not form mineral deposits when cultured under the conditions tested here and that ARS staining is a poor method to identify and confirm mineral deposits in PAVICs cultures.

Numerous studies have suggested that PAVICs and human aortic VICs may differentiate to osteoblast-like cells during calcified valve disease progression [60,62,76]. A study by Chen *et al*. demonstrated mesenchymal and osteogenic progenitor cells exist within the primary PAVICs mixed cell population. Their results further exposed that PAVICs have the ability to transdifferentiate into myofibrogenic, adipogenic, osteogenic and chodrogenic lineages *in vitro* and thus potentially *in vivo* [76]. To probe PAVICs nodules' potential for osteoblastic differentiation, the expression of two genes: type I collagen (*COL1A1*) and osteocalcin *(BGLAP)* were examined. Calcified human aortic VICs have been reported to show an increase in osteocalcin RNA expression (a late marker for bone differentiation) [123]. This study noted an up regulation of type I collagen in OST+TGF-β1 grown PAVICs, *BGLAP* expression remained stable in PAVICs grown in OST+TGF-β1 and this level of expression was significantly lower than expression levels in CTL PAVICs for the same time points. This suggests that PAVICs grown in OST+TGF-β1 for up to 21 days were not differentiating into osteoblasts. A previous study demonstrated PAVICs grown in mineralization medium for up to eight days did not display the same level of increased alkaline phosphatase (an early mineralization marker) as osteoblasts in culture [144].

The lack of osteoblastic differentiation in this study may be attributed to a wide range of factors including their growth on stiff tissue culture plastic/glass substrates and/or the inclusion of TGF-β1 within some of the tested conditions [62] and is discussed further in the future works section of this chapter. It is important to state this work does not suggest osteoblastic differentiation is not possible in other culture conditions.

In this study the OST media was supplemented with TGF-β1 due to its demonstrated physiological importance in tissue calcification. Studies have shown qualitatively higher levels of TGF-β1 in the ECM that co-localized with areas of calcification in diseased human aortic valves [124,125]. Additionally, the inflammatory response has been implicated as an important contributing factor in disease onset, which suggests a local availability of TGF-β1 [117,145] may increase during the initial stages of disease progression. Nevertheless, the connection between TGF-β1 use in this *in vitro* system and disease progression remains unclear. Osman *et al*. showed that supplementation of human VIC cultures with members of the TGF-β family (including TGF-β1) prompted the cells to adopt a more osteoblast-like phenotype by inducing the secretion of proinflammatory cytokines which may play an important role in pathological valvular calcification [60]. The results found in this study show that PAVICs grown in OST+TGF-β1 medium show no evidence of osteoblastic transdifferentiation and thus these 'calcified nodules' have yet to demonstrate their relationship to calcified aortic valve disease progression. The absence of mineral within PAVICs nodules grown in CTL+TGF-β1 and OST medium suggests the lack of mineralization is not due to solely osteogenic supplementation or the additional TGF-β1 supplementation.

TEM and histological staining demonstrated that PAVICs nodules grown in OST+TGF-β1 were marked by an abundant proteinaceous ECM, which contained collagen without a specific arrangement or orientation. Collagen production is mediated by VICs *in vivo* as part of normal valve maintenance, however, disruption of this carefully regulated process has also been associated with calcified aortic valve disease progression [146]. Valvular fibrosis and over-activated VICs have been implicated in the early stages of calcified valve pathobiology [146], including a suggestion of calcified aortic valve stenosis being more appropriately viewed as a fibrocalcific disease [147]. This study confirms TGF-β1 supplementation likely promotes and/or maintains an activated myofibroblastic phenotype in cultured PAVICs and their

production of ECM components. The relationship, if one exists, between *in vitro* PAVIC-mediated ECM production and the fibrotic stage of aortic valve calcification, however, has yet to be established and described.

PAVICs-mediated production of fibrous ECM was additionally explored using Raman spectroscopy. Like the histological analyses, Raman spectroscopy further identified the abundant proteinaceous content of PAVICs nodules cultured in OST+TGF-β1 medium. The derived PLS-DA model successfully distinguished between the two experimental PAVICs systems based on the ECM produced by PAVICs grown in OST+TGF-β1 medium. This model also clearly indicated the collagen content within the nodules was a heavy contributor to the model variables, and thus suggested collagen as a distinguishing element between the experimental groups. Taken together, these results suggest Raman spectroscopy may be an effective method to successfully and non-invasively monitor ECM production in live PAVIC systems *in vitro*.

Cross sections of OST+TGF-β1 PAVICs nodules presented positive expression of αSMA, as did monolayers of PAVICs grown in CTL medium, implicating a myofibroblastic phenotype [148]. These results show that the cells at the centre of these nodules are not αSMA positive and thus may have a different phenotype or be undergoing apoptosis, as has been previously suggested [143]. TGF-β1 has been suggested to promote myofibroblastic expression particularly when incorporated on stiff substrates [62] and calcification via an apoptosis pathway [124,146], thus suggesting a non-osteoblastic like state [124]. The results presented in this study show that PAVICs cultured in OST+TGF-β1 medium for 21 days, a relatively late time point for in vitro culture [144], do not further transdifferentiate from the activated myofibroblastic phenotype into osteoblast-like cells or contain calcium phosphate deposits within the 'calcified nodules' as seen in MOBs and human valves. Currently it remains uncertain as to whether VICs must pass through an intermediate stage of activated VICs to become osteoblast-like VICs [146,147]. Further investigations are needed to establish if the OST+TGF-β1 PAVICs models have any relationship to early (pre-osteoblastic) stages of calcified aortic valve disease.

Previously the inhibition of nodule formation in cultured VICs has been explored through the addition of statins, pravastatin [149], nitric oxide donors, as well as other cell permeate superoxide scavengers [126]. The response and transformations of VICs

grown *in vitro* to various treatments raise interesting questions regarding the relationship between these cells and the complex *in vivo* environment both in healthy and disease states. As investigations into the pathobiology of aortic valve calcification progress, characterization of both systems using a variety of techniques offers promise of bridging the gap between *in vitro* observations and *in vivo* processes.

3.6 Conclusions

This study combines gold standard biological techniques as well as advanced material characterization techniques including rapid, non-invasive Raman spectroscopy to investigate PAVICs 'calcified' nodules. The results show PAVICs grown in OST+TGF-β1 media for up to 21 days express an activated myofibroblastic phenotype and produce a predominantly collagen ECM, however, demonstrate no evidence of further transdifferentiation into an osteoblastic phenotype and/or calcium phosphate deposition as seen in known mineralizing in vitro systems and calcified human aortic cusps. These findings establish a clear limitation of cultured PAVICs grown in CTL and OST+TGF-β1 media as they do not appear to transdifferentiate into osteoblastic-like cells nor form mineral deposits what have been found indicative of calcified aortic valve disease [150]. This study also provides further information on the collagen-rich ECM produced within PAVICs nodules grown in OST+TGF-β1 medium and the heterogeneous nature of these nodules. The presented characterisation of *in vitro* PAVICs systems is critical in further understanding PAVICs behavior in culture and for comparison to aortic valve calcification.

3.7 Future Work

This study established a clear limitation in the ability of the cultured PAVICs 'calcified nodules' in producing mineral deposits seen in calcified aortic valve cusps and MOBs when grown in the conditions presented. It is critical to note the relationship between this system and the full spectrum of aortic valve pathobiology has yet to be determined. Aortic valve calcification is condition which often progresses over decades and as mentioned previously has proteinaceous changes as well as mineral deposits to consider. A myriad of complications including ECM maladaptation within diseased human aortic tissue cusps have been implicated and suggested to occur before the deposition of any calcified material. Excess fibrosis and collagen remodeling has been related to calcified aortic valve disease [146]. Thus the relationship between disruption of ECM components in the pathobiology of calcific aortic valve disease and the ECM production in these nodules has yet to be fully

explored. It also should be noted that VICs in the native valves are proposed to be very sensitive to their local environment and in response to environmental changes in order to fulfill their role of replenishing the ECM as needed to maintain normal valve structure and function. The difference between VICs activation and matrix production in a disease state and in a healthy repair state must also be clearly demarcated if any connection between a culture system and calcified aortic valve pathology is to be established.

Another consideration is the potential for the promotion or selection of specific cell types within the mixed VICs population via culture conditions such as substrate stiffness, medium, medium supplementation, incubator conditions and others [74]. Culture conditions are known to greatly affect cells isolated and grown *in vitro*. Previously substrate mechanics has been shown to have a direct effect on PAVICs in culture [62]. The relatively stiff nature of the tissue culture plastic and glass slides used in this study may be involved in the continuous activation of the isolated PAVICs and their collagen production. Another factor which may have significantly affected the outcome of this study was the inclusion of TGF- β1 within the medium. Despite being found colocalised with mineralized deposit within calcified aortic valves [124] and know to be connected with pathological valve matrix remodeling [143], it has been suggested that TGF- β signaling is associated with myofibroblast differentiation, not associated with the osteogenic process and may inhibit osteogenic calcification in the valve. These statements are yet to be fully supported through publication [146].

Further studies modifying the PAVICs and human VICs culture conditions will undoubtedly continue and characterizations will be critical in assessing their relationship to the pathology of aortic valve calcification. For any model to gain acceptance, it is also critical to understand the target conditions of the diseased tissue which the model would reproduce albeit in a simplified manner. Thus a more thorough investigation of the material characteristics of the diseased cusps is needed to establish specific model targets. In parallel work, our research group exposed and characterized mineral depositions which may provide new information on and targets of the progression of cardiovascular calcification. This is more fully described in chapter 4 and by Bertazzo et al. [51]. These types of revelations will undoubtedly provide new directions for *in vitro* models.

The focus of chapter 4 turns to characterizing diseased human aortic valve tissue (and surrounding diseased cardiovascular tissue) at various stages of pathology. Information on the proteinaceous environment developing in the ECM colocalised with mineral deposits are of critical and may help address some of the limitations in determining the relationship between simplified models and the cardiovascular calcification they intend to represent.

4 Protein Changes Colocalised with Microscopic Calcium Phosphate Deposition in Cardiovascular Tissues

4.1 Abstract

Cardiovascular calcification is a growing global health concern with much of the pathogenesis still not understood. Recently the description and characterisation of microscopic spherical mineral particles (50nm-200μm) found in vasculature and heart valves in visually undisrupted tissue and at various stages of cardiovascular calcification evolution raised interesting questions regarding the introduction and role of microscopic mineral deposits in the cardiovascular system. Raman micro-spectroscopy was combined with scanning electron microscopy to provide information on the biomolecular environments surrounding these microscopic, spherical mineral deposits in human aortic and aortic valve tissue ranging from healthy, healthy and adjacent to disturbed tissue, plaque and calcified tissue. The protein environments surrounding the microscopic spherical mineral particles in the various states were compared and analysed by comparing Raman spectra in different experimental groups using PLS-DA VIP score plots to highlight the significant bio-molecular differences between them. The results demonstrated a change in the ECM and specifically in the collagen colocalised with the microscopic spherical mineral deposits found within aortic valve and aorta tissues. In both aortic and aortic valve tissue a specific Raman collagen peak at 874 cm^{-1} distinguished between tissues containing microscopic mineral spheres and those without. Lipid rich and protein differences were distinguishing factors in comparing plaque ridden tissue from healthy and neighbouring (samples visually undisturbed yet adjacent to disrupted tissue) tissue samples. This study prompts further investigations into the local environment surrounding the microscopic spherical mineral deposits as distinct protein changes were observed. Additionally this work further supports the ability of Raman spectroscopy to non-invasively compare the wide range of biomolecular environments found in cardiovascular calcification.

4.2 Introduction

Cardiovascular calcification is a global concern and is project to nearly double by 2050 as the population and life expectancy increases [49]. Cardiovascular calcification is currently viewed as an active process which mainly affects the aortic valve and arteries and is associated with an increase risk in cardiovascular and all-cause mortality [151-153]. Currently there are no treatment options proven to reverse vascular or valvular calcification and applied therapies instead often target associated underlying disorders such as atherosclerosis, chronic kidney disease, diabetes mellitus, and osteoporosis [154]. Calcified heart valves can be surgically replaced with mechanical or bio prosthetic implants, each with the associated advantages and disadvantages as reviewed in chapter 1.

Aortic valve calcification was introduced extensively in chapter 1. This paragraph and following figure are a brief introduction into vascular calcification. A large artery consists of three morphologically distinct layers: the intima, media and adventitia (Figure 4-1). The intima is the inner most layer consisting of extracellular connective tissue matrix and bonded by a monolayer of endothelial cells on the luminal side and a sheet of elastic fibres, the internal elastic lamina, on the peripheral side. The media is the middle layer consisting of smooth muscles cells. The adventia is the outer most layer consisting of connective tissues with interspersed fibroblasts and smooth muscle cells [155]. Vascular calcification can be categorized by its location found within an atherosclerotic plaque (in the neointima) or the medial smooth muscle layer (tunica media). The neointima is a new or thickened layer of the arterial intima formed especially on a prosthesis or during atherosclerosis by migration and proliferation of cells from the media. Vascular calcification in both locations may occur in the same patient and even the same arterial site. In cardiac valve leaflets the mineralisation is thought to be similar to neointimal calcification [50,66]. It is important to note that vascular calcification is widespread in atherosclerosis and thus the factors affecting atherosclerosis are also of interest [156].

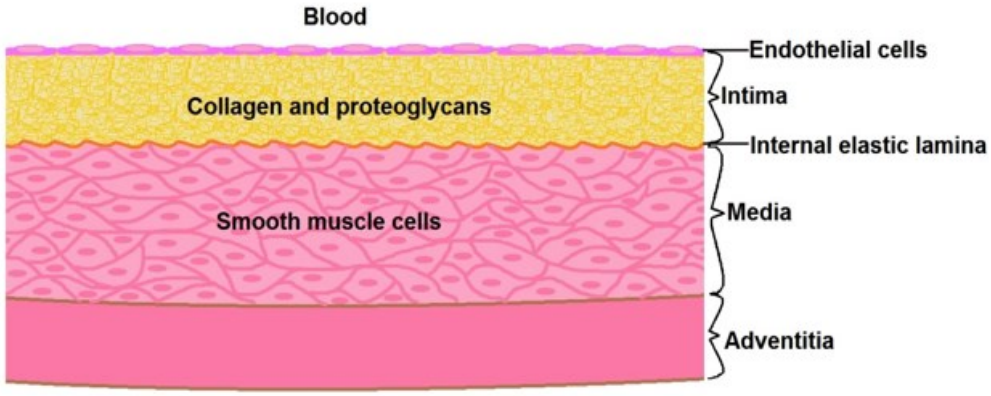

Figure 4-1 Structure of a healthy large artery. The intima's size is exaggerated in this figure and is typically a very thin region.

The extracellular matrix is known to regulate many physiological and pathological processes and is a critical determining factor of both healthy and diseased arteries and valves [156-158]. In the pathological conditions of atherosclerosis, extracellular matrix changes accompany the development of the atherosclerotic lesion and significantly impact the course of the disease[156]. Interstitial collagen types I and III are a critical component of atherosclerotic legions with collagen constitutes up to 60% of the total plaque protein contributing to plaque growth and arterial lumen narrowing [158]. Type I collagen is approximately two-thirds of the total collagen content in human atherosclerotic plaques [157]. There is an overwhelming amount of information regarding the vast role collagen plays in cardiovascular disease however for the purposes of this study, the critical applicable evidence is the disrupted, heterogeneous nature of type I collagen distribution in cardiovascular disease and the co-localisation of this collagen alteration with diseased cardiovascular environments [156-160].

The majority of observed vascular calcification provides evidence of a bone-like mineralization occurring around mineral deposits [154,161]. Cells isolated from arterial walls grown in culture have become osteogenic through the introduction of inflammatory and atherogenic stimuli. Osteoclast-like cells have been found in calcified atherosclerotic plaques [162]. The mineral deposits found in the cardiovascular system have an elemental composition similar to bone mineral and are reported as hydroxyapatite [121]. Calcification is a common feature of atherosclerotic

lesions and has been described to have histologic appearances of fully formed bone tissue including trabeculations suggesting active remodeling [163].

It remains unclear as to whether cardiovascular calcification is a cause or consequence of cardiovascular disease. There is evidence of atherosclerosis inducing cellular osteogenic transdifferentiation suggesting calcification is a consequence . However, calcium deposits may affect plaque stability and introduce compliance mismatches and overall increase the risks of a cardiovascular event [119]. Additionally new insights into microscopic mineral deposits discovered to be present before mature osteoblasts are found again raises the question of what role, if any, inorganic mineral deposits play in the pathology of cardiovascular calcification [44]. Regardless of cardiovascular calcification being a cause or consequence, it is clear extra-skeletal ossification in the cardiovascular system is of extreme importance.

Recently Bertazzo et al. adopted a material science approach to provide insight into the composition and hierarchical architecture of the mineral deposits found in cardiovascular calcification. The study revealed and described three distinct forms of calcific structures: microscopic spherical particles, fibres and a larger compact material. Microscopic, spherical mineral deposits ranging in size from 100 nm to five μm were discovered in the heart valves, aortae and coronary arteries of patients with and without calcific lesions. The spherical particles are composed of highly crystalline hydroxyapatite that is crystallographically and structurally different from bone mineral. The presence of these spherical particles before any macroscopically observable calcific lesions suggests the spherical particles may be the first mineralised structure to appear and this leads to interesting questions on what role, if any, the particles play in disease initiation and/or progression. Additionally the presence of these spherical particles in both valvular and vascular tissue makes them relevant to the wide range of cardiovascular calcification [44].

These spherical particles are of extreme interest and often found in tissues which do not appear to be visually disturbed. This study aimed to determine whether the molecular environments surrounding these microscopic mineral deposits are altered at the micron scale and what those alterations may be in human aortic and aortic valve samples. Raman spectroscopy was applied to determine the biomolecular environment surrounding these microscopic mineralised deposits with a particular emphasis on characterising and comparing the protein environments surrounding

mineralised spheres. The microscopic spherical mineral particles are highly crystalline, 50nm-200μm in diameter, and surrounded in a protein rich organic matrix [51] whereas the sampling volume for the collected Raman spectra is predominately from a focal size of approximately 10 x 20 x 40 μm. The description and investigation of any protein changes colocalised with the microscopic spherical deposits may allude to the contribution these spherical deposits play in cardiovascular disease, if any.

4.3 Methods and Materials

4.3.1 Human Tissue Collection

Human aortic valves and aortae tissue was collected from the Heart Valve Bank at John Radcliffe hospital (Oxford, U.K.). A total of 20 donors were included in this study with a mean age of 59 ± 5 years, nine male and eleven female. The tissue was obtained from patients undergoing aortic valve replacement surgery or was available for research purposes after being rejected for use in homografts. All samples were collected under approved ethical guidelines with informed consent and were anonymously analysed.

Human bone tissue was obtained from Charing Cross Hospital (London, U.K.). Cortical bone samples were collected from the femurs of two patients, one male (73 years old) and one female (72 years old) that were undergoing hip replacements. Raman spectral collection was performed on these bone samples as described in chapter 2.

4.3.2 Cardiovasular Tissue Preparation

The collected human tissue samples were washed three times in phosphate buffered saline (PBS) (Sigma, U.K.) immediately on receipt and subsequently fixed in 4% (w/v) formaldehyde (Sigma, BioReagent, ≥ 36.0%) at 4°C for a minimum of one day.

4.3.3 Sample Dissection

Cardiovascular tissue samples were dissected in regions of interest to isolate small volumes (approximately 8 mm^3) using common dissection tools and were visually categorised into the four following tissue states:

Healthy – the isolated tissue and the surrounding area was visually healthy (in aortic valve samples, the surrounding area was the entire cusp which the isolated tissue was taken from)
Neighbour – the isolated tissue appeared healthy and undisturbed however a neighbouring region appears disturbed (thickened, streaked, etc.)
Plaque – the isolated tissue was visually disturbed (thickened, discoloured, etc.)
Calcified – the isolated tissue contains calcium deposits. The tissue is thickened, discoloured and when isolated, mechanical differences are observed (hard, brittle, off-white depositions found within the tissue)

Each isolated sample was labelled and placed into an eppendorf filled with PBS for transportation to Raman imaging.

4.3.4 Raman Imaging of Aortic Valve and Aortic Tissue

Raman spectra were collected from the isolated tissue samples using the instrument described in chapter 1. Briefly, samples were illuminated with a 785 nm laser and Raman spectra were collected using a modified Renishaw InVia spectrometer connected to a Leica microscope (Renishaw, U.K.) through a water immersion 63× (NA=0.9) objective (Nikon, Netherlands). The fixed tissue samples were imaged while immersed in PBS at room temperature for no more than six hours. Raman spectra were collected from a minimum of 10 independent regions within each isolated tissue sample using the motorized stage coordinates to ensure no overlapping occurred. Each spectrum consisted of three accumulations of ten seconds over the Raman shift range of 400 to 3200 cm^{-1}.

The collected spectra were divided into three environments independent of their visual tissue state and directly related to the biomolecular signatures found within them namely: Protein rich, Lipid rich, and Mineral rich.

Raman spectra were pre-processed for multivariate analysis including smoothing (order: 0, window: 9pts), background removal (baseline subtraction using weighted least squares and multiplicative scattering correction) and mean centring. Partial Least Squares – Discriminate Analysis (PLS-DA) was used for classification and the Variable In Projection (VIP) heat maps were used to highlight spectral bands which describe the molecular features that distinguish the compared experimental groups from each other as described in chapter 2. The sensitivity and specificity was

recorded for each model used and determined by the cross validated leave out random subsets method. The number of latent variables selected for the model was also noted and reported. All data analysis was performed in MatLab R2011a (The Mathworks, U.S.A.) using a combination of in house written scripts, some written by Dr. Martin AB Hedegaard, and the PLS_toolbox 7.0 (Eigenvector Research, U.S.A.).

The peak labels found in the Raman spectra presented in this chapter are representative of the peaks found in literature and may be slightly shifted from the precise peak positions found in the spectral means displayed.

The following study utilized an edge filter in the Raman instrumentation replacing the notch filter originally described in the introduction before the study began. The instrumentation did not change during the course of this study.

4.3.5 Uni-variate Statistical Analysis

All data are presented as mean ± standard deviation. All data were compared using the Kruskal-Wallis one way analysis of variance test for statistical significance. P-values < 0.05 were considered significant.

4.3.6 Scanning Electron Microscopy

Scanning Electron Microscopy (SEM) sample preparation, imagining and image processing was performed as previously described in Bertazzo et. al. and by Dr. Sergio Bertazzo. Briefly after Raman imaging each isolated tissue sample was cut in half and dehydrated through a graded ethanol (Sigma, ACS reagent 99.5%, U.K.) series of 20, 30, 40, 50, 70, 80, 90, 100, and 100% (v/v) for 1 hour in each solution and air dried. Dehydrated samples were secured to an aluminium sample holder with carbon tape and silver paint was applied to the area immediately surrounding each sample which was then coated with 5nm carbon (Quorum Technologies Turbo-Pumped Thermal Evaporators model K975X) and 5nm chromium in a sputter coater (Quorum Technologies Sputter Coater model K575X).

Following the coating procedure, samples were imaged by the SEM (Gemini 1525 FEGSEM) operated at 10 kV. The instrument was equipped with both an inlens detector that recorded secondary electrons and a backscatter electron detector. Sample regions were imaged in inlens mode and subsequently in backscatter mode over the same area and the resulting images were stacked. The green channel was

assigned to the inlens image and red channel to the backscatter channel. Energy-dispersive X-ray spectroscopy (EDS) spectra were obtained using point and shoot mode to ensure the dense regions were mineralised.

4.4 Results

The Raman spectra collected from the aortic valve and aortic samples displayed three biomolecular environments namely protein, lipid, and mineral rich as shown in Figure 4-2. Raman spectral peaks
representative of and used to identify each environment are highlighted in Figure 4-2 and listed in Table 4-1. Raman spectral features found in the 1800-2500 cm^{-1} were due to background and were not considered in any of the following analyses. Additionally, the collected Raman spectra were not corrected for detector or instrument responses therefore the CH stretches found surrounding 2940 cm^{-1} may appear relatively less intense than Raman spectra found in literature.

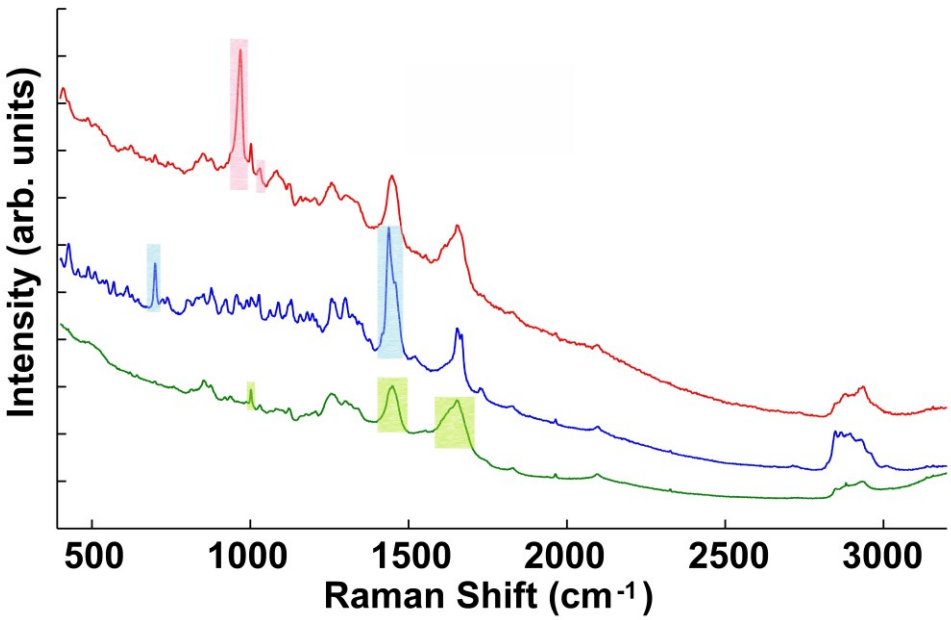

Figure 4-2 Raman spectra showing the three distinct environments collected from the human cardiovascular samples. Red – mineral rich with the 960 cm^{-1} and 1070 cm^{-1} peaks highlighted corresponding to PO_4^{3-} and CO_3^{2-} respectively. Blue – lipid rich spectrum with the 702 cm^{-1} and 1437 cm^{-1} peaks highlighted corresponding to cholesterol and CH_2 (lipids) respectively. Green – protein rich spectrum with the 1003 cm^{-1} and 1595-1720 cm^{-1} peaks highlighted corresponding to phenylalanine and amide III respectively.

Table 4-1 Raman spectral peak assignments for peaks used to identify the biomolecular environments in Raman spectra collected from human aortic and aortic valve tissue. No shading – protein assignments, light gray – lipid assignments, gray – mineral assignments.

Peak position (cm^{-1})	Major Assignments
702	Cholesterol, cholesterol ester
960	Apatite - PO_4^{3-} ν_1 symmetric stretch
1003	Phenylalanine ring breathing mode
1070	Carbonate - substituted CO_3^{2-} ν_1 in-plane vibrations
1437	CH_2 (lipids) and CH_2 deformation (lipid)
[redacted]	Amide I (C=O stretching mode of proteins, a-helix conformation)/C=C lipid stretch

Protein rich environments were found in all visible tissue states (healthy, neighbour, plaque and calcified). Lipid Raman spectra were collected from sphere containing plaque and calcified tissue. Mineral spectra were only collected from calcified tissue.

After Raman imaging, all samples were immediately prepared for SEM imaging where the samples were thoroughly scanned for any evidence of microscopic calcification. Figure 4-3 is a representative image of the identified mineral inclusion showing a spherical mineral deposit found in an aortic valve sample. Both spherical and compact mineral deposits were first identified by morphology and density discrepancies and further confirmed using EDS spectral elemental analysis [51].

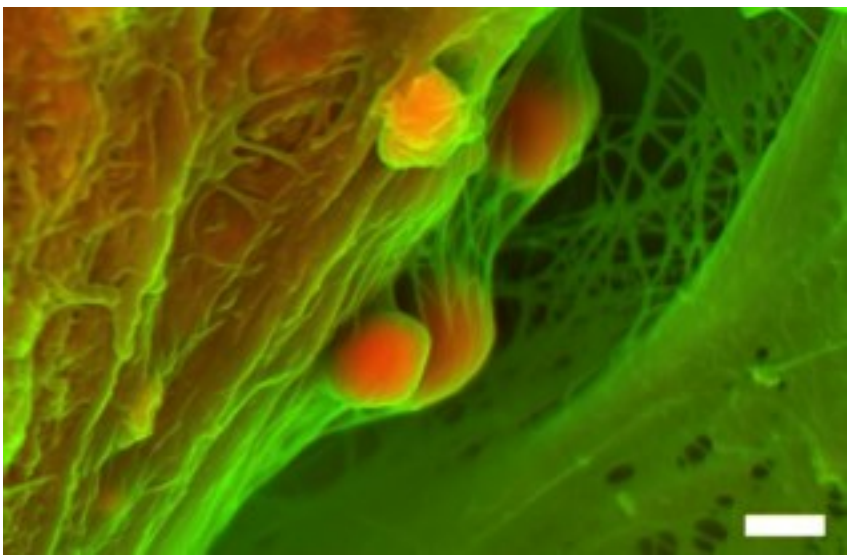

Figure 4-3 Density-dependent colour SEM micrograph of human aortic valve tissue showing mineralised microscopic spheres. Scale bar = 1µm.

Tissue samples were then divided by their visually determined tissue states (healthy, neighbour, plaque, and calcified), Raman spectral environments (protein, lipid, and mineral rich), and any inclusion of mineral deposits (organic – no mineral inclusion, spherical mineral deposits, large compact mineral deposits). Table 4-2 gives the number of spectra collected in each sample group for the aortic valve samples tested.

Table 4-2 Total number of Raman spectra collected from the aortic valve as divided into each sample group. The table shows the division of Raman spectra collected from human aortic valve tissue into their respective sample groups, columns being micro-mineral inclusion, rows being Raman spectral environments and the shading of the cells referring to the visual tissue state. Each number within the table shows the number of Raman spectra collected.

Micro-mineral inclusion / Raman spectral features	Organic (No Spheres)	Spheres	Compact
Protein Rich	12	220 112	20
Lipid Rich		39	5
Mineral Rich			4

Healthy
Neighbour
Plaque
Calcified

Protein rich Raman spectral environments were found in all tissue states (healthy, neighbour, plaque, calcified) and in tissue with and without spheres and in compact calcification within aortic tissue samples. Lipid rich Raman spectra were collected from neighbour tissue containing spheres, plaque tissue containing spheres and calcified aortic tissue containing compact mineral deposits. Mineral rich Raman spectra were only collected from calcified tissue containing compact mineral deposits. A Chi-squared test resulted with a two-tailed p-value less than 0.005 when comparing samples in which mineral deposits were expected (calcified samples) to samples found to contain mineral deposits and samples not expected to contain mineral inclusions (healthy, neighbour and plaque) compared to samples without found mineral inclusions.

Table 4-3 gives the number of spectra collected in each sample group for the aortic samples imaged.

Table 4-3 Total number of Raman spectra collected from the aorta as divided into each sample group. The table shows the division of Raman spectra collected from human aortic tissue into their respective sample groups, columns being micro-mineral inclusion, rows being Raman spectral environments and the shading of the cells referring to the visual tissue state. Each number within the table shows the number of Raman spectra collected.

Micro-mineral inclusion / Raman spectral features	Organic (No Spheres)	Spheres	Compact
Protein Rich	12	32	39
		57	61
		26	
Lipid Rich		24	31
		28	35
		23	
Mineral Rich			34

Healthy
Neighbour
Plaque
Calcified

Only protein rich spectra were included in the comparisons shown in this study as the proteinaceous differences (if any) were of the most interest. The unsupervised technique of principal component analysis (PCA) was performed and although some experimental grouping was observed there was not sufficient information to distinguish experimental groups confidently from one another. For this reason supervised techniques were incorporated to discriminate between the experimental groups. A Chi-squared test resulted with a two-tailed p-value less than 0.005 when comparing samples in which mineral deposits were expected (calcified samples) to samples found to contain mineral deposits and samples not expected to contain mineral inclusions (healthy, neighbour and plaque) compared to samples without found mineral inclusions. PLS-DA VIP plots were constructed by first plotting the mean spectrum of the two experimental groups compared (with one being intensity shifted so the spectra were not overlapping). A VIP heat-map is then overlaid onto the mean spectra so that the more intensely green a Raman spectral band, the more significant that spectral region was in discriminating between the sample groups in the PLS-DA model. For each of the following PLS-DA VIP plots, the mean spectrum from each group is shown after the pre-processing steps used in the PLS-DA analysis excluding mean centring. Mean centring was withheld so the resulting mean spectra would show spectral features as widely recognised and comparable to literature. Each

PLS-DA plot compares two sample groups and an independent model was constructed for every comparison.

Three experimental groups from the aortic valve samples were compared in the following comparisons:

healthy tissue without spheres vs. neighbour tissue containing spheres (Figure 4-4).
neighbour tissue containing spheres vs. plaque tissue containing spheres (Figure 4-5).
healthy tissue without spheres vs. plaque tissue containing spheres (Figure 4-6).

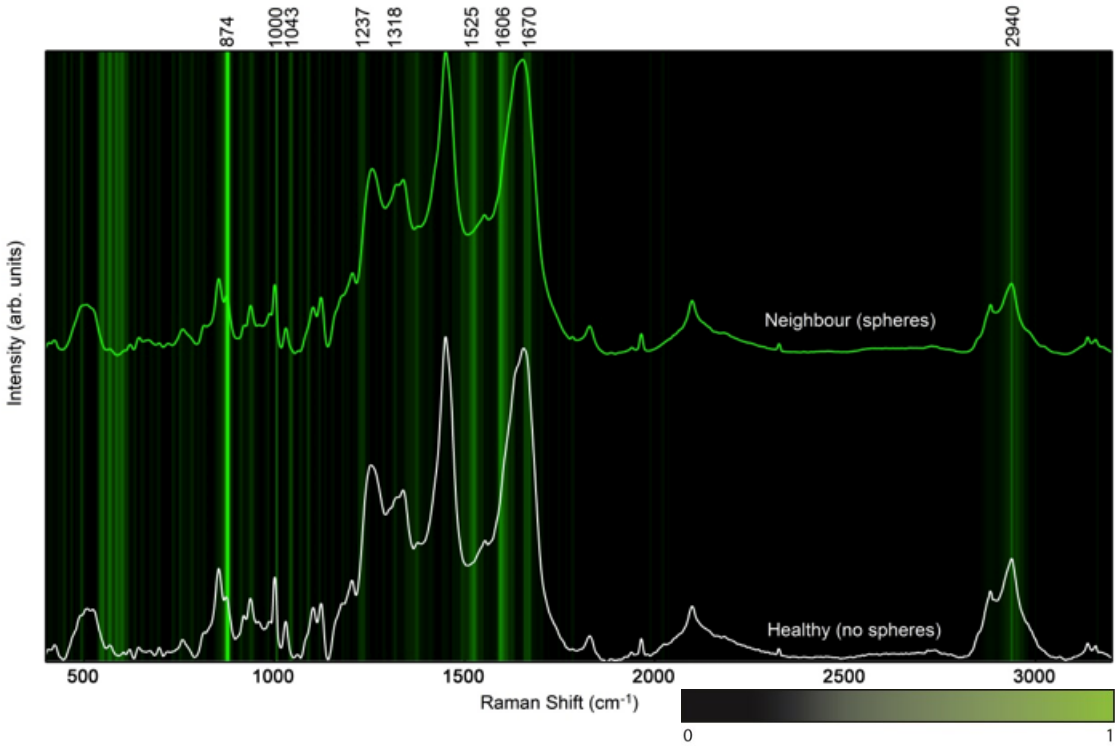

Figure 4-4 PLS-DA VIP scores plot displaying Raman bands from the aortic valve which distinguished between healthy tissue samples without mineral inclusions and neighboring tissue samples with microscopic, mineral, spherical inclusions. The more intense the green band, the more significant the Raman shift range in the PLS-DA models ability to distinguish between the two groups. Selected band's wavenumbers are shown at the top of the figure.

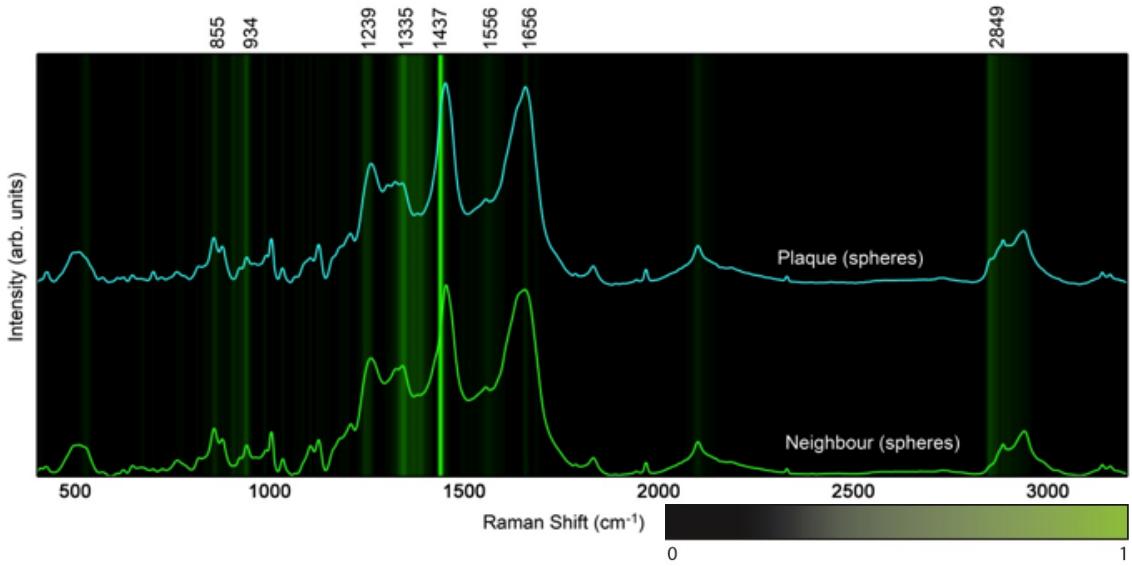

Figure 4-5 PLS-DA VIP scores plot displaying Raman bands which distinguished between aortic valve neighboring tissue samples with microscopic, mineral, spherical inclusions and plaque tissue with microscopic, mineral, spherical inclusions. The more intense the green band, the more significant the Raman shift range in the PLS-DA models ability to distinguish between the two groups. Selected band's wavenumbers are shown at the top of the figure.

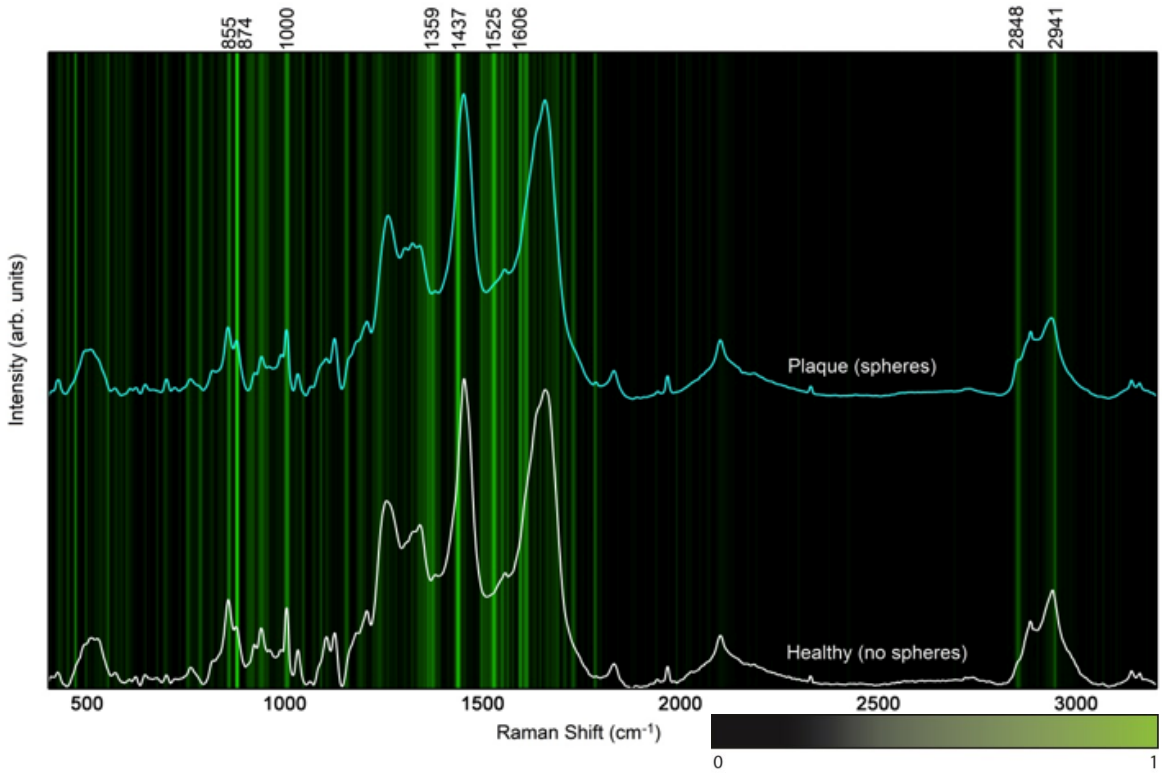

Figure 4-6 PLS-DA VIP scores plot collected from the aortic valve displaying Raman bands which distinguished between healthy tissue samples without mineral inclusions and plaque tissue containing microscopic, mineral, spherical

inclusions. The more intense the green band, the more significant the Raman shift range in the PLS-DA models ability to distinguish between the two groups. Selected band's wavenumbers are shown at the top of the figure.

The PLS-DA model constructed from the comparison of healthy tissue without mineral inclusions vs. neighbour tissue with microscopic spherical mineral inclusions resulted in an 80% sensitivity and specificity using four latent variables. Raman spectral band assignments for the bands highlighted and labelled in the VIP heat map in Figure 4-4 are shown in Table 4-4. The highlighted wavenumbers found in this comparison are all protein peaks/bands including 874 and 1043 cm^{-1} which are specifically collagen assignments.

The PLS-DA model constructed from comparing neighbour tissue containing mineral spherical deposits vs. plaque tissue containing mineral spherical deposits resulted with a 74% sensitivity and specificity using three latent variables. Bands assignments for the Raman bands highlighted and labelled in the VIP plot shown in Figure 4-4 are described in Table 4-4. These highlighted wavenumbers contain protein and lipid peaks/bands including the collagen assignments found at 855, 934 and 1335 cm^{-1} and lipid assignments at 1437 and 2849 cm^{-1} with 2849 cm^{-1} specifically indicating a change in the amount of lipids between the compared groups.

The PLS-DA model comparing healthy tissue without mineral inclusions to plaque tissue containing sphere mineral inclusions resulted with an 80% sensitivity and specificity using four latent variables. Raman spectral bands assignments for the bands highlighted and labelled in the VIP heat map (Figure 4-6) are shown in Table 4-2. The highlighted wavenumbers include protein and lipid peaks/bands. Specifically collagen assignments were found (855, 874 cm^{-1}) and lipid assignments (1437 and 2848 cm^{-1}) with 2848 cm^{-1} specifically indicating a change in the amount of lipids between the two compared sample groups.

PLS-DA VIP plots were constructed for the comparison of aortic tissue sample groups. Four sample groups were included in the following comparisons:

healthy tissue without mineral inclusions vs. healthy tissue containing spherical inclusions (Figure 4-7A).

healthy tissue containing spherical inclusions vs. neighbour tissue containing spherical inclusions (Figure 4-7B).
healthy tissue containing spherical inclusions vs. plaque tissue containing spherical inclusions (Figure 4-7C).
neighbour tissue containing spherical inclusions vs. plaque tissue containing spherical inclusions (Figure 4-7D).

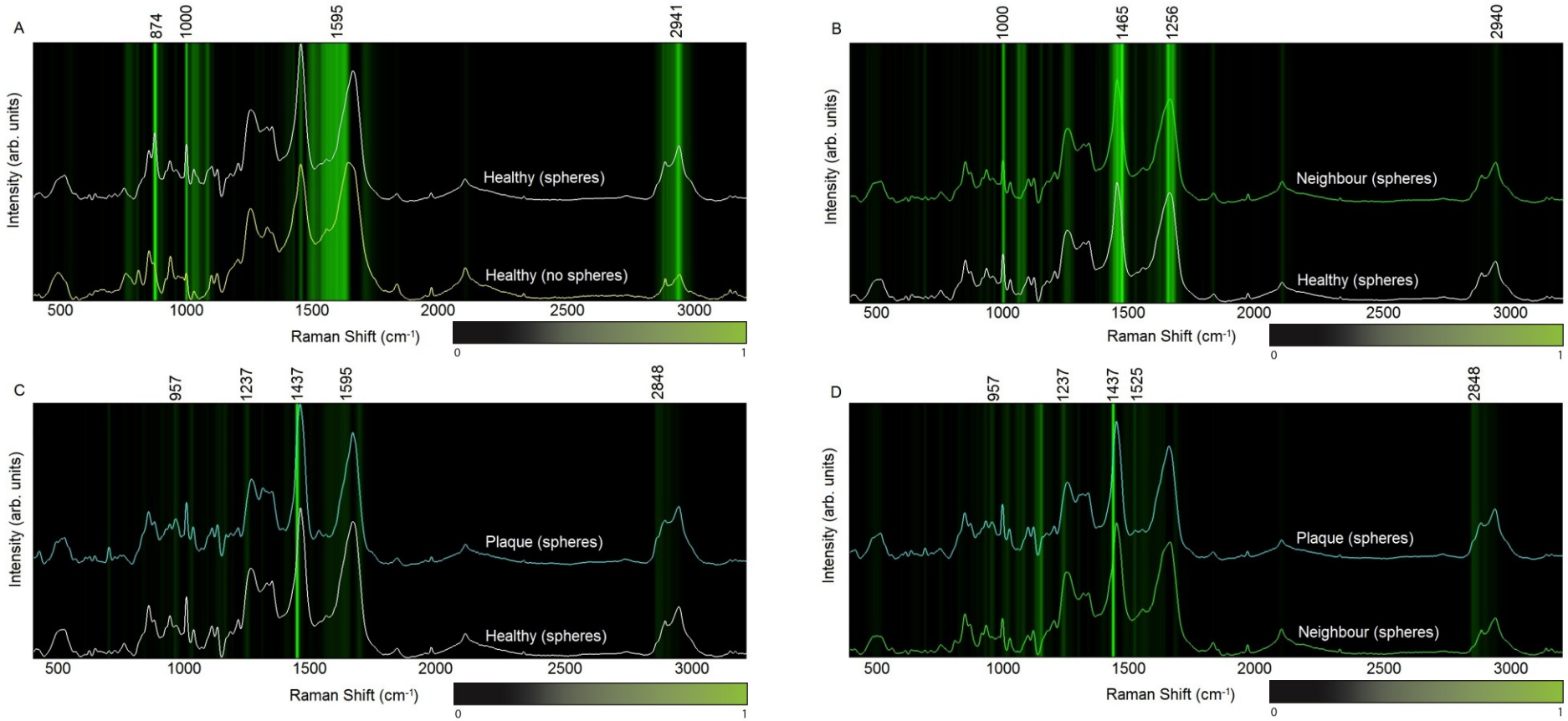

Figure 4-7 PLS-DA VIP heat maps highlighting spectral bands distinguishing healthy tissue without spheres (yellow mean spectrum), healthy tissue with spheres (white mean spectrum), neighbouring tissue with spheres (green mean spectrum) and plaque tissue with spheres (blue mean spectrum) from the aorta. The more intense the green band, the more significant the Raman shift range in the PLS-DA models ability to distinguish between the two groups. Selected band's wavenumbers are shown at the top of the figure.

The PLS-DA model used in the comparison of healthy tissue without spheres to healthy tissue with spheres had a sensitivity and specificity of 81% with one latent variable. The labelled bands highlighted through the VIP heat maps (Figure 4-7A) consisted of protein assignments with 874 cm^{-1} being a collagen assignment with assignments shown in Table 4-4).

Table 4-4 Band Assignments for bands highlighted in the PLS-DA VIP heatmaps comparing tissue groups from the aortic valve and aorta. *collagen assignment

Peak position (cm^{-1})	Major Assignments
855	C-C stretch, proline *
874	C-C stretch, hydroxyproline *
934	C-C backbone *
957	Cholesterol
1000-1003	Phenylalanine
1043	Proline *
1235-1239	Amide III (ref Raman in bio tissue review paper)
1318	Amide III (α-helix)
1335	CH3CH2 wagging, *
1359	Tryptophan
1437	Lipids in normal, lipid deformation
1465	Lipids
1480-1575	Protein amide II band
1525	In-plane vibrations of the conjugated -C=C-
[redacted]	Amide I (C=O stretching mode of proteins, a-helix conformation)/C=C lipid stretch
2817-2849	CH2 symmetric stretch of lipids (suggests change in the amount of lipids)
2940-2941	C-H vibrations in lipids & proteins

The PLS-DA model used in the comparison of healthy tissue with mineral spheres to neighbour tissue with mineral spheres had a sensitivity and specificity of 67% with three latent variables. The Raman spectral bands highlighted through the VIP heatmaps are protein assignments (Figure 4-7B) with assignments shown in Table 4-4.

The PLS-DA model used in the comparison of healthy tissue with mineral spheres to plaque tissue with mineral spheres resulted in a sensitivity and specificity of 79% with two latent variables. The labelled bands highlighted through the VIP heat maps (Figure 4-7C) included protein and lipid assignments. The 2848 cm^{-1} highlighted peak indicates a change in the amount of lipids between the sample groups. Corresponding Raman spectral band assignments are shown in Table 4-4.

The PLS-DA model used in the comparison of neighbour tissue containing mineral spheres to plaque tissue containing mineral spheres resulted in a sensitivity and specificity of 79% using three latent variables. The labelled bands highlighted through the VIP heat maps (Figure 4-7D) include protein and lipid assignments with the 2848 cm^{-1} highlighted band indicating a change in the amount of lipids between the compared sample groups. Corresponding Raman spectral assignments are shown in Table 4-4.

Spectra collected from human aortic valves calcified samples and human bone samples contained several identifiable mineral peaks including the 960 cm^{-1} apatite (PO_4) peak and the 1070 cm^{-1} type B carbonate (CO_3) peak. Bone samples demonstrated a lower full width at half maximum of the 960 cm^{-1} apatite (PO_4) peak when compared to calcified valve samples suggesting bone is more crystalline ($p<0.05$) when compared to compact calcification (Table 4-5).

Table 4-5 Raman phosphate peak area and FWHM comparison between human bone and mineralized aortic valve cusps. *significantly different from bone ($p<0.005$)

	Phosphate Peak	
	Area (arbitrary units)	FWHM (cm^{-1})
Mineralized Human Aortic Valve Cusps	3.0616±0.9880*	17.5387±14.4641*
Human Bone	5.8613±0.3428	16.1122±0.4079

4.5 Discussion

Cardiovascular calcification is a growing global concern projected to increase with longer life expectancies. It is highly correlated with cardiovascular disease and is a significant predictor of cardiovascular events [46]. Cardiovascular calcification disease pathogenesis is still unclear and under intense investigation. Microscopic mineral

spheres found in all stages of cardiovascular calcification disease progression have been identified and characterised by Bertazzo et al [51]. These spherical mineral deposits are a common mineral inclusion in valvular and vascular calcification with their role, if any, in disease progression yet to be determined. Important questions remain on the introduction, influence and impact of such microscopic spherical inorganic deposits as they exist embedded in an organic matrix within cardiovascular tissue before macroscopic mineral deposits are observed. This study investigated the biomolecular environments surrounding these spherical microscopic mineral inclusions in the human aortae and aortic valve cusps through the use of Raman micro-spectroscopy aiming to expose any protein differences colocalised with these spherical deposits.

Raman spectra were collected from microscopic regions of human aortic valves and aortae ranging in visual tissue states (healthy, neighbouring, plaque, or calcified) and microscopic mineral inclusion (no mineral, microscopic spherical, or compact calcification). The resulting Raman spectra were classified as protein rich, lipid rich or mineral rich based on their molecular signatures. Raman spectra including mineral signatures were only found in samples which contained compact calcification. This suggests only compact calcification was above the sensitivity limit of the Raman spectroscopy as applied in this study. Samples containing microscopic mineral spheres without compact calcification showed no identifiable mineral peaks in the resulting Raman spectra. Tissue samples without spherical mineral deposits did not produce any lipid or mineral rich Raman spectra. Protein rich Raman spectra were found in all visibly determined tissue states (healthy, neighbour, plaque, calcified) which contained spheres in both the aortic valve and aorta samples. Protein rich and lipid rich spectra were found in more visual tissue states in the aortic samples than the aortic valve. Difference between the Raman spectral environments collected between aortic and aortic valve samples may be due to their distinct structural difference or the possible divergence in the evolution of vascular and valvular calcification. Protein rich Raman spectra were collected from healthy tissue without mineral inclusions, healthy tissue with microscopic spherical mineral inclusions, neighbouring tissue with mineral spheres and plaque tissue with mineral spheres. These protein rich spectra were then compared to examine any changes in the biomolecular environment surrounding the spherical microscopic mineral presence in aortae and aortic valves.

Aortic valve calcification disease progression includes the abnormal distribution and organization of extracellular matrix (ECM) proteins. Inflammation, ECM remodelling, and cellular transdifferentiation have all been implicated as potential precursors to the osteoblast like cellular mineralisation found in the late stages of the disease. Distinct protein differences were found when comparing healthy aortic cusp tissue without mineral inclusions to neighbour tissue (being visually healthy however adjacent to diseased tissue) with microscopic spherical mineral inclusions. The Raman spectral bands distinguishing between these experimental groups include collagen specific assignments (874 and 1043 cm^{-1}) implying collagen alterations between the two groups. The fibrosa is the tissue layer of the aortic valve in which aortic valve calcification is thought to initiate. It is a collagen rich layer closest to the aorta and early stages of aortic valve calcification have been reported to include a collagen disruption in valvular tissue undergoing microscopic abnormal processes. Fibrosis is increasingly implicated as a possible contributor to pathogenesis of calcified aortic valve disease [147]. The results here suggest a possible ECM modification and specifically collagen differences between healthy aortic cusp tissue without mineral inclusions and visually healthy tissue with microscopic spherical mineral inclusions.

Healthy aortic valve tissue without mineral inclusions and neighbour tissue containing mineral spheres displayed proteinaceous and lipid differences when compared to plaque tissue containing the mineral spherical deposits. Analysis comparing healthy aortic cusp tissue to plaque tissue highlighted collagen alterations in bands 855, 934 and 1335 cm^{-1}. Interestingly, these bands differ from the bands highlighted in comparing healthy (without mineral inclusions) and neighbouring tissue (with mineral spheres) suggesting perhaps a molecularly different type of collagen alteration and or collagen environmental alteration. Lipid differences were found to be significant in discriminating between the healthy and neighbour tissue from plaque tissue. The introduction of lipid differences is likely due to the known lipid inclusions found in plaques formed in cardiovascular disease and are heavily associated with fatty streaks and plaque architecture. Spectral band differences found to distinguish plaque tissue from healthy and neighbouring tissue also included the 2848 and 2849 cm^{-1} peaks signifying a change in the amount of lipids. These differences echo the widely reported environmental lipid constituents of plaques found in cardiovascular tissues.

Protein differences were found surrounding the microscopic spherical mineral deposits within visually undisturbed tissue when compared to tissue without mineral deposits proposing a colocalised change in the ECM around these microscopic spherical mineral deposits. However, this does not implicate any causality or relationship between mineral sphere inclusion and early fibrotic stages of cardiovascular calcification. In the aortic cusp, microscopic mineral spheres were found in almost all samples as the donors for this particular study consisted of many individuals past their fourth decade of life and thus mostly with some form of cardiovascular disruption (thickened aortic valve cusps, fatty streaks in vasculature, etc.). It is important to note however, although there is an increase in cardiovascular events with age, cardiovascular calcification is an active regulated process cannot be considered an inevitable, irreversible senile disorder. With larger scale (compact) calcification being a known implication of higher risks of a cardiovascular events [153], it remains to be determined if microscopic mineral deposits play a role in or are could be an early sign of a disruption in cardiovascular tissue. The results of this study suggest a change in proteins and specifically collagen in the aortic cusp accompanying the mineral deposits. Further investigations should be performed to determine if a relationship exists between a deviation from 'healthy' ECM production and maintenance and the mineral spheres inclusion surrounding protein changes described here.

The aortic tissue micro-mineral environment characterisation exposed many tissue areas which were healthy in appearance, not adjacent to any regions visually disturbed and contained microscopic mineral sphere inclusions. The comparison of healthy aortic tissue with and without spheres suggests protein changes with the 874 cm^{-1} band specifically identifying a collagen change. This is same Raman band and thus type of collagen bond change seen to distinguish healthy aortic cusp tissue without mineral inclusions and neighbouring tissue containing mineral spheres. This suggests the mineral spheres may be colocalised with a protein and particularly a specific type of collagen change in both tissues types. Protein changes were observed between healthy aortic tissue with mineral spheres and neighbouring tissue with mineral spheres. The protein differences found between these two groups showed with a distinct lack of collagen assignment specific changes. This lack of collagen assignment differences leads to an interesting observation of collagen specific changes being identified between tissues without sphere and tissue with spheres, however when the spheres are present, there appears to be protein changes which are not

specifically collagen induced. With the known role of collagen disruption in atherosclerosis and cardiovascular calcification [146,157-159], the possible distinction of collagen changes accompanying these microscopic mineral spherical deposits is critical as this suggests an alteration from the normal healthy state.

Aortic plaque tissue with mineral spheres compared to both healthy tissues and neighbouring tissue with mineral spheres exposed changes in protein, lipid, and the amount of lipids as expected with the known lipid inclusions in vascular plaques[154,157].

Previously Bertazzo et al. applied immunogold-labelling of cardiovascular tissue for early and late stage osteoblastic transcription factors in cardiovascular tissues containing these microscopic mineral spherical inclusions. The results suggested the presence of spherical particles may precede the appearance of mature osteoblastic cells and the localization of spherical particles may contribute to early osteoblastic transdifferentiation or alternatively, the expression of early osteoblastic markers may lead to the localization of these spherical particles. The protein and specifically collagen changes observed in this study are local to the spheres in an environment shown to contain cells with early osteoblastic markers. It is well reported that collagen alteration is associated with initial stages of bone mineralisation [164]. Compact calcified deposits are found colocalised with mature osteoblasts and display mineral Raman peaks. Raman spectroscopic identification of mineral produced by mature osteoblasts is has been previously demonstrated and even seen in mineralized nodules formed from osteoblasts in culture [12,30,165].

Not all Raman spectral bands highlighted in the PLS-DA VIP score plots were highlighted and extracted for classification and comparison between the sample groups. Often these spectral bands highlighted did not correspond to Raman peaks or bands found in the collected spectra. Bands highlighted in regions where a strong signal was not present may be exposing differences in background and more susceptible to noise. Although pre-processing techniques were applied to reduce the influence of background signals in the spectral analysis some fluorescence from the tissue remains. Raman peaks/bands highlighted in the PLS-DA VIP score plots which were not well described or observed in biological tissue Raman spectra literature were not included in the discussed comparisons between groups. The biological finger print region of Raman spectra is very well described and reported on and therefore

more confidence was placed into peaks and bands which are well supported in literature. The multitude of bonds, molecular environments and various vibrational frequencies associated with those molecular bonds can hinder analysis due to overlaps, multiple bond assignments and peak shifting. The selected VIP highlighted bands discussed in this study were well reported in literature, components found in cardiovascular tissue, and displayed a peak/band intensity suggesting the signal was from the excited sample.

The SEM micrographs collected in this investigation from the aortic valve and aorta further echo the discoveries stated in Bertazzo et al.'s paper regarding the presence of these spheres in unremarkable cardiovascular tissue [51]. The application of Raman spectroscopy here further supports the initiative to apply materials science techniques to provide insight into the calcified environments in cardiovascular disease. Raman spectroscopy has been extensively used in bone mineralisation studies and is a useful tool for the rapid and non-invasive characterisation and comparison of mineralised tissues. As applied here the sensitivity of Raman spectroscopy may be exploited to give a biomolecular fingerprint of tissue regions of interest surrounding the microscopic mineral sphere inclusions without being overrun by the sharp mineral peaks found in compact calcification.

Raman spectroscopy confirms a mineral presence in the aortic valve cusps with inorganic mineral peaks clearly present in compact calcification. Human aortic cusp mineralization does however vary from human bone as shown by a significant difference in their crystallinity. Calcified aortic valve spectra showed a greater variation in the apatite peak area and shape in comparison to bone, suggesting a heterogeneous mineral environment is present. Comparison of the mineral environment detected by Raman spectroscopy and that observed by electron microscopy confirm only 'compact' mineralisation is within the sensitivity limits of Raman spectroscopy as applied here. The spheres are below the sensitivity limit of the Raman spectroscopy in this study and therefore the Raman spectra show their encapsulation in fibrous and or lipid rich tissue. The mineralised Raman spectra therefore do not reflect the highly crystalline nature of the spheres but instead demonstrate that compact calcification is more amorphous than human bone. This is may be a result of the difference between ectopic cellular mineralisation in cardiovascular calcification and the highly regulated and organised bone matrix mineralisation.

4.6 Conclusions

Raman spectroscopy was combined with SEM to provide information on the biomolecular environment surrounding microscopic, spherical mineral deposits found within aortic valve and aortic tissue. The protein environments surrounding microscopic spherical mineral particles were compared and analysed using PLS-DA VIP score plots. The results demonstrated a change in the ECM and particularly in the collagen colocalised with the tissue containing microscopic spherical mineral deposits. A specific collagen alteration highlighted at 874 cm^{-1} was found in both aortic and aortic valve tissue to distinguish between tissues containing microscopic mineral spheres and those without. Lipid rich and protein differences were observed as distinguishing factors in comparing plaques tissue from healthy and neighbor tissue samples. This study warrants further investigations into the local environment surrounding these microscopic mineral deposits and the inclusion of Raman spectroscopy to better identify and compare the wide range of biomolecular environments found in cardiovascular calcification.

4.7 Future Work

The donor population presented in this study included a range of ages and both sexes however, the population distribution included in these studies needs to be expanded to fully understand the range of environments which may exist colocalised with the spherical mineral deposits of interest. The patients included in this study were all from a relatively small geographical area and thus a myriad of associated confounders such as culture, diet, access to healthcare, etc. could affect a study like the one present here comparing broad spectrum diseases like cardiovascular calcification. Strict access to tissue further limits the populations available for study. An initial step in any further studies should attempt to secure tissue donors from a wider array of locations, ages and conditions.

This study suggests the spherical mineralised particles may be colocalised with collagen and protein changes deviating from healthy tissue without these mineral inclusions. This does somewhat assume cardiovascular tissue containing these mineral spheres are not ‘healthy’. Additionally neighbour tissue may be assumed to be more susceptible to alteration due to its proximity to disturbed lesions however this is not always the case. If the completely healthy tissue contains spheres which are not associated with any disruptive or pathological processes, the comparisons found here

may allude to variations in healthy protein environments. There remains intensive literature support suggesting fibrosis, changes in the ECM, and collagen environments specifically occur at early stages of the cardiovascular disease leading to calcification [157-159]. At a minimum the results shown in this study call for further investigation as to the significance of these protein changes and any relationships they may have with pathological protein changes.

In future studies it would be interesting to investigate the presence of these microscopic spherical mineral inclusions in cellular or animal models associated with cardiovascular calcification. Chapter 3 investigated a PAVICs 'calcified' model and found no mineralisation present within the cultured nodules. The TEM applied in the PAVICs study found no spherical mineral inclusions however there were distinctly less images taken than in this study and by Bertazzo et al. in which entire tissue areas were scanned. Ultimately animal models showing vascular and valvular disruption could also be analysed using the material science techniques described in these studies to learn more about the microscopic mineral inclusions and their associated consequences.

5 Raman Spectroscopic Evidence of Tissue Restructuring in Heat-Induced Tissue Fusion

5.1 Abstract

Heat-induced tissue fusion via radio-frequency (RF) energy has gained wide acceptance clinically for blood vessel fusion and is being considered for bowel anastomosis. This is the first optical-Raman-spectroscopy study on tissue fusion samples *in vitro*. This study provides direct insights into tissue constituent and structural changes on the molecular level, exposing spectroscopic evidence for the loss of distinct collagen fibres rich tissue layers as well as the denaturing and restructuring of collagen crosslinks due to RF fusion. Raman spectroscopic maps of the cross section tissue of RF fused tissue is compared to adjacent histological sections and gives further insight into the distinct collagen environment changes between health and fused tissue within the same sample. Multivariate analytical methods were used to determine the collagen spectral fingerprint in each reason to allow for direct comparison of the collagen in each mapped region. Raman spectral changes indicative of collagen thermal denaturing were observed in RF fused tissues including the shift of the 1252-1261 cm^{-1} peak to lower frequencies in RF fused tissues demonstrated a collagen crosslink disruptions and the significant shift of the amide I, 1660cm^{-1} band to higher wavenumbers in RF fused tissues indicative of the increase in reducible crosslinks and a decrease in non-reducible crosslinks within collagen. These findings additionally open the door for more advanced optical feedback-control methods and characterization during heat-induced tissue fusion, which may lead to new clinical applications of this promising technology.

5.2 Introduction

Tissue sealing and reconnection are routine surgical procedures. Among other technologies, heat-induced tissue fusion using radio-frequency (RF) energy has attained wide acceptance. In surgery, RF based blood vessel sealing has been clinically approved [166,167], e.g., the RF bipolar vessel sealer (LigaSure™, Covidien, USA). More recently, significant research efforts have been made to develop new fusion instruments for other tissue types, e.g. intestinal tissues during bowel anastomosis to replace traditional hand suturing or stapling [168-170]. This technology exploits the

heat-induced fusion of native tissues to achieve high-quality rapid tissue sealing without introducing foreign materials (i.e., sutures, staples, clips, or glue) and is expected to greatly reduce morbidity, mortality and cost.

Anastomotic leaks are some of the most dreaded complication after colorectal surgery. Consequences for patients include agonizing abdominal pain, tachycardia, high fevers and a rigid abdomen often accompanying hemodynamic instability. In these cases the patent is urgently returned to the operation theatre for peritoneal washout and faecal diversion with prolonged stays in the intensive care unit. Additionally these complications are not always found early in the postoperative period and can be diagnosed late in the postoperative period [171]. Considering these concerns, RF fusion technology provides the advantage of a fast, technically undemanding, haemostatic procedure which could dramatically reduce the resulting trauma and complications for the patient [169].

The mechanism for heat-induced tissue fusion, particularly for blood vessel sealing, has been discussed in many studies [167,169,170,172]. The RF tissue fusion here consists of clamping tissue ends between two electrodes while holding the opposing faces under a compression pressure (CP). A controlled RF voltage is then applied so an induced current generates heat via the Joule effect. Heat-induced tissue fusion is believed to be the result of the simultaneously applied heat and CP. Changes in collagen bonds within the fused tissue are thought to be pivotal to the strength of the resulting fusion. It is widely accepted that heat denatures collagen to a gel-like amalgam, which then forms strong bonds between neighbouring tissues[167,172]. The existing characterization and analysis, however, have been mainly made on either direct microscopic observation or mechanical strength testing. The lack of understanding at the molecular and cellular levels has left several important questions in this field unresolved. Critically it is still unclear as how the collagen changes within the fused tissue during heat-induced RF tissue fusion and the precise mechanism for the formation of the strong seal. Answering these questions will provide a better understanding and knowledge of the intrinsic mechanisms for RF tissue fusion and also help to develop more effective control methods for RF fusion procedures. Furthermore, the main challenge in intestinal tissue anastomosis is achieving effective control over the delivered energy to form a successful fusion without causing excessive thermal tissue damage. This requires a better understanding of the fusion mechanism and more importantly, the development of effective feedback technologies

to control the fusion procedure. Therefore, more advanced techniques are in great demand to study RF tissue fusion on the cellular and molecular levels.

Raman spectroscopy provides an attractive way of rapidly capturing the molecular environment of tissues without destroying or altering the samples [173-176]. Raman micro-spectroscopy generates information-rich spectra which, when combined with chemometrics, provides powerful insight into the molecular diversity within heterogeneous biological samples [87,177]. Proteins have been studied extensively using Raman spectroscopy as information regarding the amino acids, amide bonds between them and their tertiary structure can be extracted and analysed [178,179]. In particular, Raman spectroscopy has been used to identify changes within isolated animal collagen during thermal and chemical denaturing [180,181]. These studies provide a molecular fingerprint to identify collagen and demonstrate the powerful ability of Raman spectroscopy to expose specific molecular changes within collagen. Additionally, it is possible to deconstruct individual contributors, such as collagen, from an overall tissue sample for characterisation and comparison [182]. By scanning across an area of interest, the individual Raman spectrum at each acquisition point can be combined to form a Raman map, which is similar to a microscopic image but with the ability to focus on certain chemical markers within the imaged area. The Raman map provides a direct observation of molecular distributions, such as that of collagen fibres, within a sampled area.

In this current study, for the first time, is demonstrated the use of Raman spectroscopy to characterize RF tissue fusion *in vitro*. Tissue fusion was performed with two tissue types, namely porcine blood vessels and small intestines, and assessed the seal quality based on the mechanical strength of the seal given by burst pressure (BP) testing. Porcine blood vessels were used as RF tissue fusion of blood vessels is established and clinically approved. The Raman spectra were acquired from fusion samples characterized as either having a strong seals or weak seals, and conducted Raman mapping across fusion regions. Correlation between the Raman results and the mechanical strength of the seals was investigated, and the differences at the molecular level examined. The Raman maps were compared with conventional histopathology microscopic results to assess whether they were superior in characterizing RF tissue fusion due to the rich molecular information contained in fused tissue Raman spectra.

5.3 Materials and Methods

5.3.1 Animal Tissue Preparation

Fresh porcine small bowels were obtained from a local abattoir, cut into 20-30 cm long segments, moistened with physiological saline and refrigerated at 4°C for up to 30 hours (from the time of slaughter) until needed for fusion experiments. Prior to the fusion experiment, sufficiently long tissue samples were selected and immediately dissected into 5 cm long pieces for tissue fusion experiment. Prepared 5 cm samples were kept hydrated in sealed plastic sample bags with saline and used within 30 minutes. Porcine blood vessels were cleaned, cut into 6 cm long pieces, and then immediately frozen in liquid nitrogen within 4 hours from the time the animal was slaughtered. The frozen tissues were kept at -70°C. Frozen blood vessel samples were only thawed at room temperature immediately before the tissue fusion experiment. Sample preparation was carried out by Dr. Lei Su.

5.3.2 Radio Frequency Tissue Fusion

RF energy was used as the source for tissue heating in this study. The RF generator was an energy research tool prototype developed by Covidien (Boulder, Colorado), capable of delivering a programmable sinusoidal current from 0-7 A and a power from 0-350 W. An operating RF frequency of 472 kHz was chosen to avoid neuromuscular stimulation and electrocution. Two tissue sealing devices were used: a commercially available LigaSure™ Impact (Covidien) for blood vessel sealing and an anastomosis prototype for small bowel sealing (Figure 5-1). Pre-written RF energy control algorithms were loaded into the RF generator using fusion software written in LabVIEW (National Instruments) so that the entire procedure could be automated. The algorithm was designed to control RF energy delivery to achieve tissue heating and the applied energy was controlled using feedback from the measured tissue impedance to maintain a specific variation in impedance with time. RF fusion device modification and tissue fusion was performed by Dr. Lei Su.

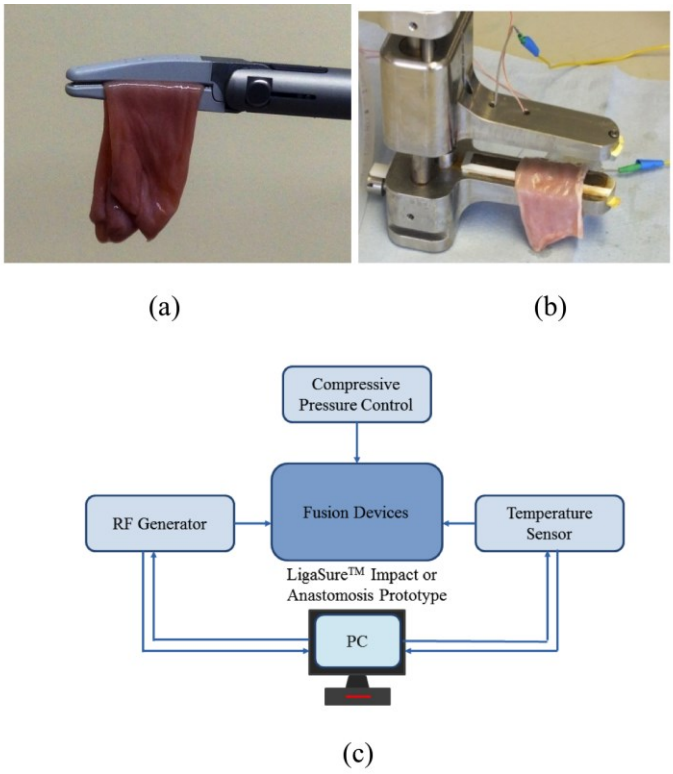

Figure 5-1 Radio frequency tissue fusion prototype. (a) LigaSure™ Impact fusion device for blood vessel sealing, (b) anastomosis prototype fusion device for small bowel sealing, and (c) RF tissue fusion setup.

During fusion, the tissue samples were clamped between the jaws of the fusion device. RF energy was supplied by the RF generator and applied to tissue samples via electrodes in jaws. The RF generator also continuously monitored both voltage and current delivered to the tissue. The varying tissue impedance was then obtained by using real-time voltage and current readouts. A compression spring in the handle of the LigaSure™ Impact device provided a constant pressure of ~0.3 MPa, and an air compressor was connected to the prototype, supplying a variable CP from 0–0.5 MPa. More than 200 tissue fusions were performed in the experiment.

5.3.3 Temperature Measurements

Tissue temperature was measured using a fine (0.005 inch) tip Teflon-insulated J-type thermocouple (5TC-TT-J-36-36, Omega Engineering, Bridgeport, New Jersey). The thermocouple was inserted through slits present on the sealing device jaws and glued in place so that its tip protruded 0.25 mm above the electrode surface. In this way the thermocouple was in contact with the tissue surface without piercing it whilst remaining insulated from the electrode. The communication between the

thermocouple and the computer was achieved through a National Instruments (NI) PXI-6289 DAQ board and a NI SCC-68 terminal block. The latter hosted four NI SCC-TC02 Thermocouple Signal Conditioning Modules. Each SCC-TC02 could drive one thermocouple and had individual signal conditioning modules with a 2 Hz low-pass filter, which filtered out the RF signal and eliminated the RF interference from the thermocouple readout.

There were in total more than 200 porcine small-bowel fusion temperature profiles recorded and only a few of these samples were provided for the investigation described here. The embedded thermocouple recorded a two stage evolution in tissue temperature evolution during fusion: a rapid increase in tissue temperature within a few seconds followed by a relatively stable plateau where the tissue temperature variation was within the range of ± 5°C. The tissue temperature was determined by the impedance control algorithm. A steep rising slope significantly reduces the duration of the whole procedure and a higher plateau temperature in the range between 60°C to 90°C ensures the necessary collagen denaturation in the tissue [167,172], which is believed to be essential for a strong fusion. Plateau temperatures below 60°C may not lead to the denaturation of collagens, while excessive temperatures need to be avoided as they lead to permanent damage of the tissue or necrosis. Temperature measurements were performed by Dr. Lei Su.

5.3.4 Sample Preparation and Imaging

Tissue samples were stored at -80°C, following fusion. Thawed samples were trimmed and embedded in optimal cutting temperature medium (OCT, Tissue-Tek, Sakura, Torrance, California) by flash freezing in isopentane at -160°C. The OCT blocks were sectioned on a cryostat at -20°C, cutting 15 μm sections for histology and Raman spectroscopy. Sections for histology were mounted on glass, washed with water to remove the OCT, and stained with haematoxylin and eosin (H&E). Sections for Raman analysis were mounted on MgF_2 slides, stored at 4°C, and imaged without further processing. Visualisation of the H&E-stained sections was performed under 4x magnification on an Olympus IX51 inverted light microscope, captured digitally and spliced together to allow visualisation of the entire field. Sample preparation for imaging was performed by Joseph Steele.

5.3.5 Raman Micro-spectroscopy

Tissue Raman maps were collected with a 785 nm laser, using a Renishaw InVia spectrometer connected to a Leica microscope as previously described [183]. A 100x (NA = 0.9) objective (Leica, U.K.) was used. Raman maps were collected over selected regions of interest with a step size of 75 μm in the x and y direction. At each point a spectrum was collected using five accumulations of five second scans covering the Raman shifts range of 620-1700 cm^{-1}. Samples were tested for no longer than 1 hour at room temperature and kept hydrated using saline.

Raman spectra were pre-processed for background removal (baseline subtraction using weighted least squares) [184] and multiplicative scattering correction [185,186]. The N-FINDR spectral unmixing algorithm was used as it searches the original input spectra, from the non-dimension reduced input matrix, for the most extreme spectra present and exposes these as endmembers. These endmembers were then identified based on their spectral features as pure contributing component of the tissue (in this study, the endmember corresponding to the collagen within the tissue was of interest). After the identification of each relevant endmember a Raman map was constructed with each pixel represented as a linear combination of the endmembers as previously described [44]. Each pixel thus contains an abundance value between 0 and 1 for the presence of each endmember within the pixel's spectrum [44].

Raman peak shift univariate comparisons are shown as mean ± standard deviation. A two-sided Wilcoxon rank sum test with a p-value < 0.05 was used to determine statistical significance.

The peak labels found in the Raman spectra presented in this chapter are representative of the peaks found in literature and may be slightly shifted from the precise peak positions found in the spectral means displayed. The following study utilized an edge filter in the Raman instrumentation replacing the notch filter originally described in the introduction before the study began. The instrumentation did not change during the course of this study.

5.3.6 Burst Pressure Measurements

The mechanical strength of the fused tissue was evaluated by a burst pressure (BP) testing system. This system consisted of a syringe pump, a pressure gauge, a sample

injection needle and a surgical clamp to close the small bowel tissue. The main arm of a Y-splitter tubing system was connected to a water-filled syringe controlled by the syringe pump. The other two split arms were connected to the pressure gauge and the sample injection needle, respectively. The surgical clamp sealed the other end of the piece of fused small bowel. The sample injection needle pierced the small bowel tissue to allow water to be injected into the sealed bowel without damaging the seal. After the initiation of the BP test, the syringe pump drove the water filled syringe to provide a flow rate of 20 mL/min, which constantly increased the pressure in the tubing system as well as in the fused tissue. Eventually the fused tissue burst at the fusion line, and the peak pressure was recorded as the BP.

More than 200 porcine small bowel segments were fused for BP testing in a parallel study. As reported elsewhere [187], the BP, as an indication of the fusion mechanical strength, varied significantly with the change of CP during fusion. Tissue samples fused at CPs lower than 0.10 MPa displayed an average BP of ~10 mmHg, while samples fused at higher CPs (>0.10 MPa) showed an average BP of more than 20 mmHg. Increased burst pressures were observed at all CP values above 0.10 MPa. These BP results served as a guideline for planning the Raman experiments carried out in this work with samples fused at three CPs (0, 0.2 and 0.3 MPa) selected for analysis in order to understand the resulting differences in fusion strength. For blood vessel samples, a commercial LigaSure™ Impact fusion device was employed with a fixed value of ~0.3 MPa. The average BP for the blood vessels was above 100 mmHg, higher than for small bowel samples due to differences in the tissue and devices used. Burst pressure measurements were performed by Dr. Lei Su and colleagues.

5.4 Results

5.4.1 Raman Micro-spectroscopy Results

RF fused blood vessels and small bowel samples fused at different CPs were imaged using Raman spectroscopy. Raman maps were collected from selected regions within the tissue cross-sections including fused areas, undisturbed and thus considered 'healthy' areas, and the interface between them. Raman maps of selected regions are shown for a fused porcine blood vessel at 0.3 MPa compression (Figure 5-2) and porcine blood vessels (Figure 5-3) fused (a) without compression, (b) with 0.2 MPa compression and (c) with 0.3 MPa compression. A white light micrograph showing the

cross section of each tissue sample is shown in each figure (Figure 5-2 and Figure 5-3, top left of the figure) with rectangular boxes highlighting the areas that were mapped by Raman. The three areas which were selected for mapping included (Figure 5-2 and Figure 5-3A) healthy tissue, (Figure 5-2 and Figure 5-3B) the interface between healthy and fused tissues and (Figure 5-3 and Figure 5-3C) fused tissues. The resulting Raman map and the endmember spectra identified in the sample and used to construct the Raman map are shown in Figure 5-2 and Figure 5-3A-C. All Raman maps shown were reconstructed from the two endmember as shown in spectra in each panel.

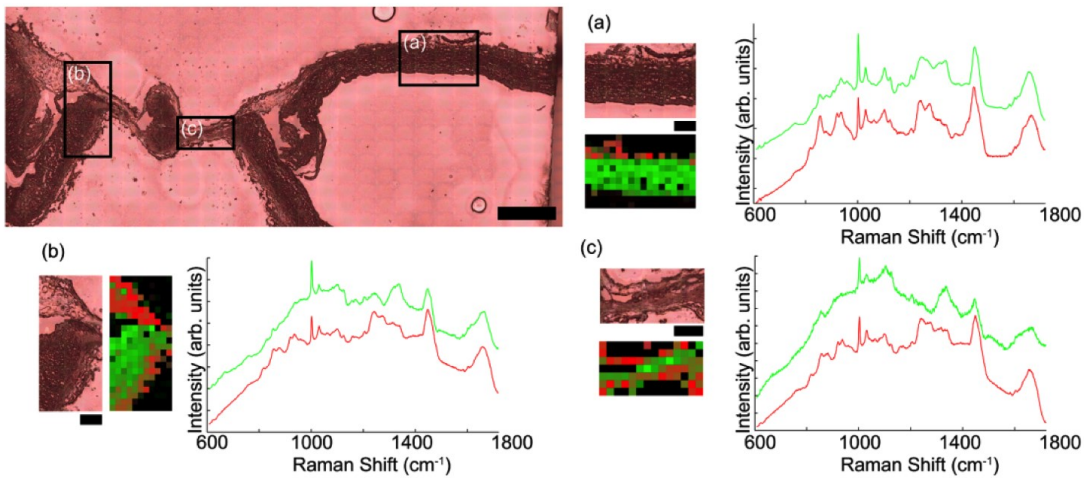

Figure 5-2 Raman spectroscopy maps collected from within a porcine blood vessel tissue at the locations indicated in the white light micrograph (shown in the top left, scale bar = 1 mm). Mapped regions included (a) healthy tissue, (b) interface between fused and healthy tissues and (c) fused tissue. White light images of each area selected for Raman mapping are shown in sections [a-c] (scale bar = 250 µm) together with their corresponding Raman map shown in the red, green and black images. The spectra included in [a-c] shows the collagen endmember spectrum in red with the intensity of the red colouring in the Raman maps corresponding to the presence of collagen within that pixel. The non-collagen rich tissue endmember spectrum is shown in green and the intensity of the colour green in the Raman map corresponds to the presence of non-collagen rich tissue within that pixel.

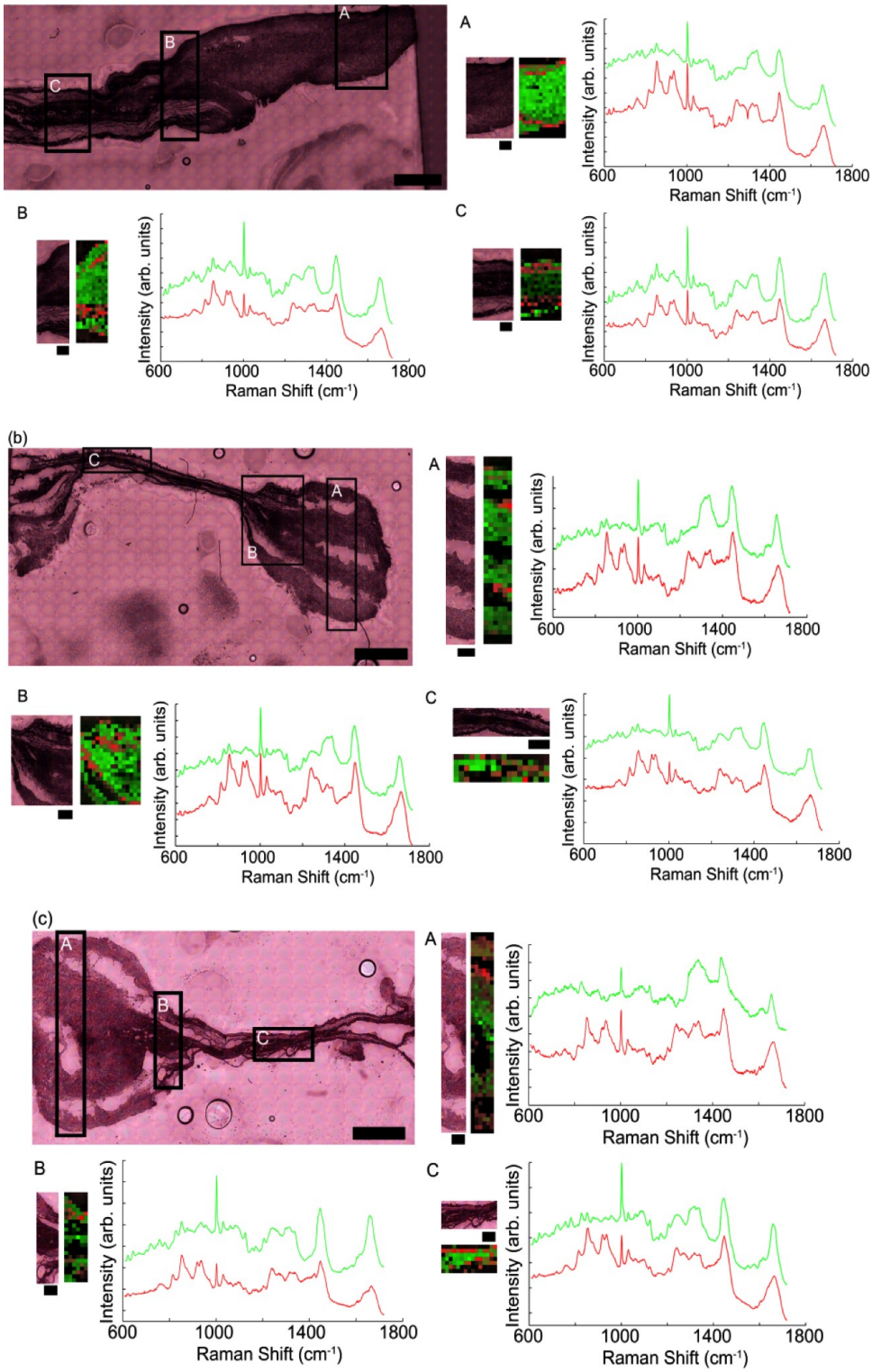

Figure 5-3 Raman maps collected over porcine bowel tissue selections (each shown in the top left white light micrograph, scale bar = 1 mm) with (a) no compression (b) compression at 0.2 MPa and (c) compression at 0.3 MPa. In each case mapped regions included [A] healthy, [B] interface between fused and healthy and [C] fused tissue. For each sub-region white light images of the area selected for Raman mapping are presented [A-C] (scale bar = 250 µm) together with their corresponding Raman maps shown in the red, green and black

images. The spectra show the collagen endmember spectrum in red and the non-collagen rich endmember spectrum is shown in green, and the intensities of red and green within the Raman maps are proportional to these signals.

The bottom spectrum (in red) representing the identified collagen endmember spectrum within the sample and the top spectrum (in green) presents the non-collagen rich tissue constituent. The collagen endmember spectrum identified by the N-finder algorithm in each map includes all the characteristic features previously reported in Raman spectroscopy studies of collagen and collagen rich tissues [188]. Specifically, Raman bands corresponding to C-C stretch of proline (855 cm^{-1}), C-C stretch of hydroxyproline (874 cm^{-1}), C-N stretch of proline (919 cm^{-1}), proline (1043 cm^{-1}), and Amide III (1245-1270 cm^{-1}) are notable [188]. The hydroxyproline and two proline peaks identified in these spectra are specifically Raman collagen assignments [188] confirming a collagen presence. The endmember spectrum which was identified to be non-collagen rich tissue included spectral features indicative of biological tissue including bands corresponding to cholesterols (699 cm^{-1}), phenylalanine (1003 cm^{-1}), C-H deformation of proteins (1262 cm^{-1}) and carbohydrates (1342 cm^{-1}), and amide I (1660 cm^{-1}) [24].

The mean of all spectra collected from the healthy and fused areas of the blood vessel which underwent RF fusion and the bowel tissues which underwent RF fusion at 0 MPa, 0.2 MPa and 0.3MPa CP are shown in Figure 5-4. In both the blood vessel and the bowel tissues a shift in the peak maximum occurred in the 1660 cm^{-1} Amide I band and a change in band shape was observed in the 1443 cm^{-1} C-H_2 wag band compared with the fused mean spectrum from the healthy mean spectrum in each sample. Many peaks, including the 940 cm^{-1} peak representing the protein alpha helix did not appear to change peak position or shape. Fused bowel tissue demonstrated a significant shift in the Amide I band to higher wavenumbers in all CPs and corresponding burst pressures as shown in Figure 5-5.

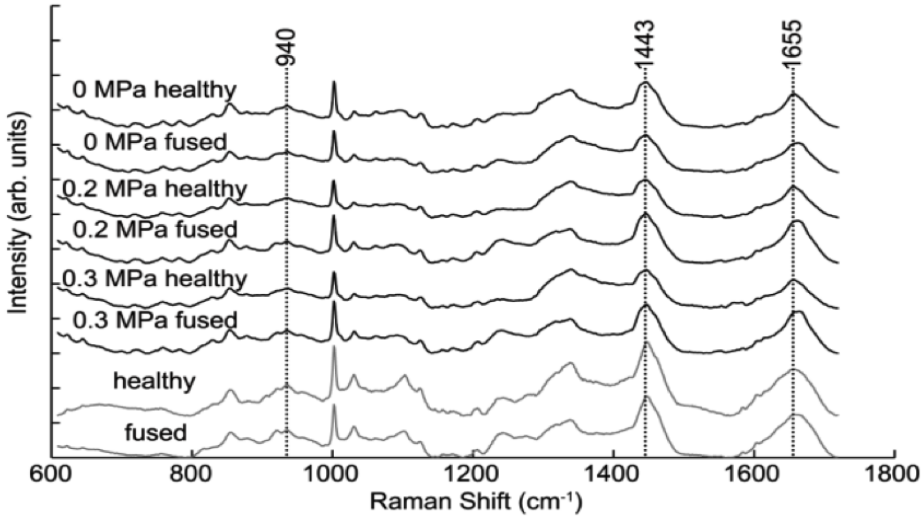

Figure 5-4 Mean Raman spectra of healthy and fused tissue areas mapped in porcine blood vessel and bowel tissue. Each spectrum labelled 'healthy' represents the mean of all collected spectra from an undisturbed cross section of the tissue. Each spectrum labelled 'fused' represents the mean of all collected spectra from the fused cross section of the tissue. Grey spectra were collected from porcine blood vessel tissue with and without radio frequency fusion as labeled. Spectra shown in black were collected from porcine bowel tissue with the corresponding compression pressure labelled (in the healthy spectrum, the pressure of the adjacent fused tissue is indicated in the label). Raman 940 cm^{-1}, 1443 cm^{-1} and 1655 cm^{-1} peaks are highlighted corresponding to the protein alpha helix, CH_2 wag, and the Amide I C-N-H stretch respectively.

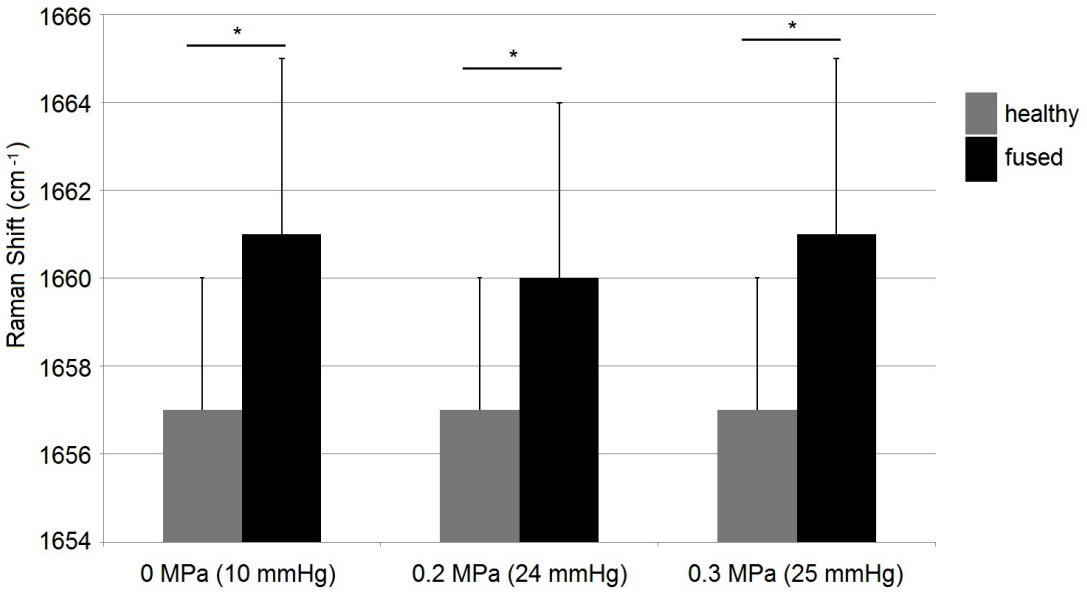

Figure 5-5 Amide I peak maximum Raman shift (cm^{-1}) location in bowel tissue samples comparing healthy and fused tissue. Samples were fused with 0, 0.2, and 0.3 MPa compression pressure and the corresponding burst pressure is in parenthesis. *p-value < 0.05.

Changes specifically in the collagen rich environments were investigated through a threshold analysis using the endmembers identified with the N-FINDR algorithm. Spectra showing an abundance value greater than 0.6 of the collagen rich endmember were selected and the means of these spectra were then calculated for each map. These means were then compared between healthy and fused areas to identify changes in the collagen environment due to fusion via a difference spectrum (Figure 5-6). Fused porcine blood vessel tissue showed the changes in the 1252-1261 cm^{-1} peaks and a shift to lower wavenumbers in the 1447 cm^{-1} peak. The 1600-1650 cm^{-1} Amide I band showed a shift to higher wavenumbers. For the bowel tissues, different changes were noted corresponding to different fusion CPs, however, only the samples which were fused with no compression and at 0.2 MPa compression were used for comparison as only these sample maps included more than three spectra which met the threshold requirements. The changes in the collagen rich spectra between fused and healthy areas were less pronounced in the porcine bowel tissue samples when compared to fused blood vessels. Bowel tissue fused at 0.2 MPa CP demonstrated similar but less distinct trends in the protein band shifts to the blood vessel results, specifically in the three broad protein bands, 1245-1270, 1445, and 1660 cm^{-1} corresponding to the Amide III, CH_2 bending and Amide I bands respectively. In bowel

tissue fused without compression band shift trends included the 1245 and 1660 cm^{-1} Amide III and Amide I band, respectively, however less dramatic shifts were seen in other protein bands (Figure 5-6).

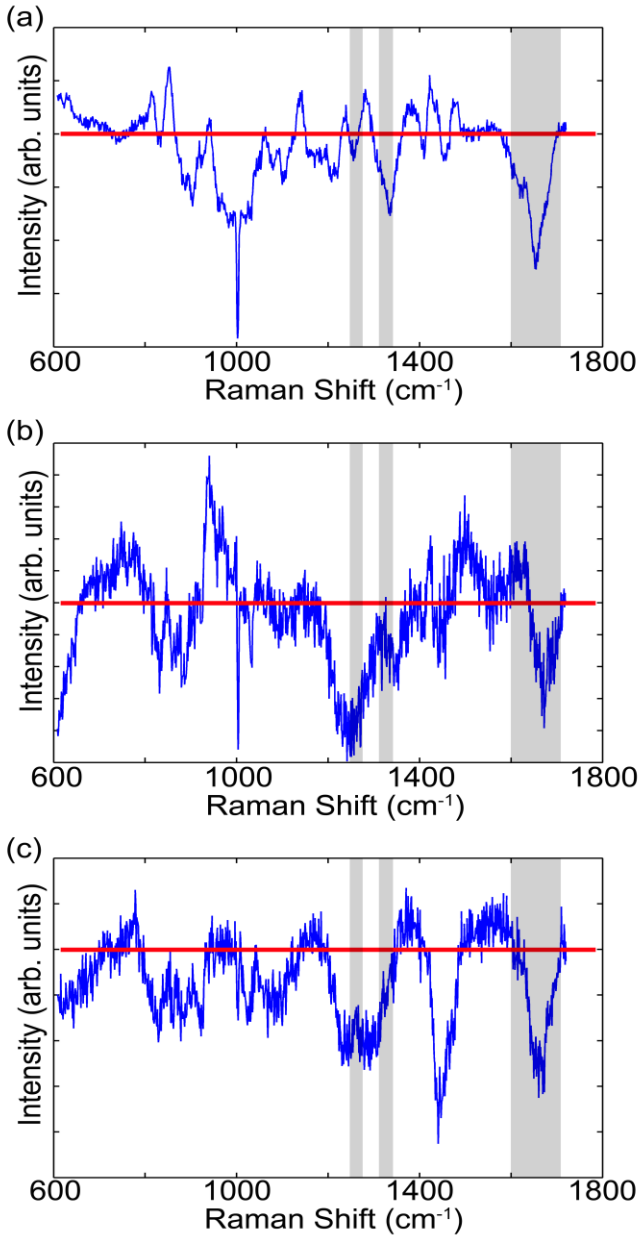

Figure 5-6 Difference Raman spectra of healthy - fused collagen rich tissue areas from (a) RF fused porcine blood vessel and (b) RF fused porcine bowel tissue without compression and (c) 0.20 MPa compression pressure. The red line indicates a zero difference. The 1313 cm^{-1}, 1324 cm^{-1}, 1252-1261 cm^{-1} and 1600-1690 cm^{-1} peaks are highlighted corresponding to the CH_3CH_2 twisting and wagging mode of collagen (respectively), amide III, and amide I (non-reducible collagen crosslinks at lower wavenumbers and reducible collagen crosslinks at higher wavenumbers) respectively.

5.4.2 Histopathology Results

In Figure 5-7, the histopathology results are presented for a porcine blood vessel and porcine small bowels fused at different CPs. A reduction in the thickness and the loss of distinct tissue layering is observed in the fused porcine blood vessels as expected (Figure 5-7 (a)). A seal appears to have formed between the upper and lower small-bowel pieces for the porcine small bowel tissue sample fused at no compression pressure, as shown in Figure 5-7(b) although the boundary between these two layers can still be seen. The three layers of small bowel tissue: serosa, submucosa and mucosa layers can be clearly identified and the delimitations between different layers are apparent. Although the tissue thickness was reduced at the mucosa layer, the tissue structure remains similar to the native tissue. Figure 5-7(c) and (d) show porcine small-bowel samples fused at CPs of 0.2 and 0.3 MPa. Relative to Figure 5-7(b), Figure 5-7(c) and (d) display significant changes in the tissue structure resulting from the applied CP. The delimitation between submucosa and mucosa layers is less clear and the thickness of the mucosa layer has reduced considerably. Most important, a more homogeneous amalgam was formed by the upper and the lower mucosa layers in the centre of the fusion region, and the boundary between the upper and the lower mucosa layers has completely disappeared.

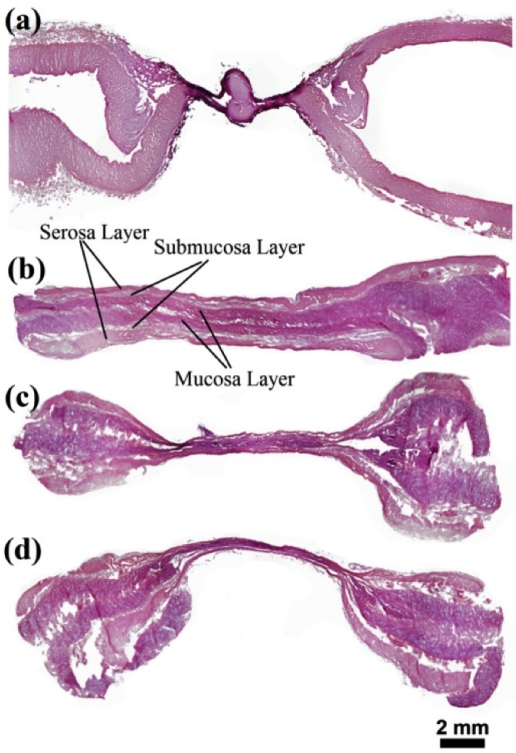

Figure 5-7 H&E staining of a fused porcine blood vessel and bowel tissues. (a) porcine blood vessel; (b) porcine small-bowel sample fused at 0 MPa; (c) porcine small-bowel sample fused at 0.2 MPa; and (d) porcine small-bowel sample fused at 0.3 MPa CP.

5.5 Discussion

RF tissue fusion is a mature technology for blood-vessel sealing in modern surgery which holds great promise to reduce some of the critical complications in existing bowel anastomosis procedures including post-operative bleeding and leakage. Here we investigated the use of Raman spectroscopy to provide biomolecular insights into the restructuring which occurs during tissue fusion. Raman results were linked to optimal fusion parameters (CP in particular) obtained by comparing to the BP test results and histological sections.

Raman spectroscopy was conducted in order to explain the observed changes in mechanical strength shown in the BP measurement of fusions when CP was changed. Raman spectroscopy was applied to non-invasively image cross sections of healthy and fused tissue as shown in Figure 5-2 and Figure 5-3. Applying N-FINDR spectral unmixing allowed for visualisation of the various bowel tissue layers by identification of the endmember spectra which are defined by the most extreme spectra present

within the map [189]. The tissue layers identifiable through Raman spectroscopy correspond to those layers seen in the white light micrographs and in the histological sections by utilizing only two endmember spectra, one corresponding to a high collagen contribution and the other to non-collagen rich tissue. Raman spectroscopic maps were reconstructed from the two endmembers with endmember abundance plots overlaid and converted to red-green colour images based of the contribution of each endmember to each collected spectrum. The submucosal layer is clearly distinguished in each small intestinal cross section by its increased collagen content. During sectioning of the intestinal tissue, the shear force caused some separation of the healthy tissue sublayers (serosa, submucosa and mucosa). In Figure 5-3(a) A, the loss of the serosa is clearly visible in the white light micrograph and the corresponding Raman map. The collagen rich submucosa is located between the mucosa and serosa. The mucosa and serosa are shown to include many of the Raman spectral signatures of biological tissues including cells (DNA peaks included) and the extracellular matrix. Collagen Raman signature bands are found in the mucosa and serosa layers as well, however these layers appear to be less collagen rich with a greater cellular contribution corresponding to the known constituents of these tissue layers.

Previous reports have suggested that changes in collagen were significant in RF fusion [190,191]. To further explore this we compared the collagen rich spectra from healthy and fused tissue. In order to perform this analysis the collagen rich spectra were identified as those having an abundance value greater than 0.6 for the collagen endmember spectrum found in each Raman map. The mean of all spectra which were identified to be predominantly collagen was then calculated and the healthy and fused tissue collagen was compared through the difference spectra of these collagen means as shown in Figure 5-6. This analysis was performed on both fused porcine blood vessels as well as fused porcine bowel tissue. The difference spectrum comparing areas of fusion to healthy tissue in blood vessels showed similar band shifts and thus biomolecular bond changes in two independent samples. These trends included the denaturing of collagen shown through the significant shift of the peak maximum in the 1655 cm^{-1} Amide I band to higher wavenumbers in the fused tissue area, also suggesting an increase in reducible crosslinks and a decrease of non-reducible cross links within the collagen [192]. Additionally a shift in the 1302 cm^{-1} peak to higher wavenumbers has been previously reported in collagen thermal denaturing [181]. Changes in the 1313 cm^{-1} and 1324 cm^{-1} peaks signifying changes in the CH_3CH_2

twisting and wagging modes of collagen also demonstrated a disruption to the native collagen [193,194]. Lastly the apparent shift of the 1252-1261 cm^{-1} peaks to lower frequencies also implicate that crosslinks may have been reduced or broken [165]. RF fusion of the porcine bowel tissue demonstrated less pronounced differences however fusion performed at 0.2 MPa compression pressure demonstrated many of the same changes, including shifts in the 1252-1261, 1313, 1324, 1443, and 1655 cm^{-1} bands, as seen in the fused blood vessels, again indicating a denaturing of collagen and more specifically a decrease in non-reducible cross links and an increase in reducible cross links as seen in Figure 5-6(c).

Histopathology results show the fused tissue area to be thinner and lacking the tissue layers visible in healthy tissue. The merging and restructuring of the biochemical constituents of the tissue layers in the bowel tissue during RF tissue fusion with CP is also demonstrated in the Raman maps. At 0 MPa CP, the fused area is visibly thicker, and the tissue layers are still distinct as shown with the white light images and histology. The Raman map shows this again with the collagen rich layers remaining very distinct and encased by non-collagen rich layers as seen in Figure 5-3(b and c). As the CP was increased to 0.2 MPa, the greatly reduced thickness of the fused area made it hard to visually distinguish whether the native tissue layers were still preserved post RF fusion. The Raman map indicated a collagen rich upper and lower layer in some areas of the fused region and less distinguishable collagen layering in other areas (Figure 5-3(b)). Furthermore at 0.3 MPa CP there was no distinct layering of collagen rich and non-collagen rich regions within the fused tissue and collagen rich areas are found throughout the thin fused area. The collagen within the fused region of samples which underwent compression also demonstrated collagen cross linking modification and collagen amide bond modification which were not detected in tissue fused without compression as seen in the Raman results. When comparing these results to the burst pressure measurements, it is notable that both the 0.2 MPa and 0.3 MPa CP fused tissues showed median burst pressures of more than 20 mmHg. The correlation of higher burst pressures in the compressed fused tissue samples with less distinct tissue layering and a change in collagen crosslinking supports the hypothesis that collagen crosslinking modification via RF fusion plays an important role in the overall quality of the tissue fusion.

H&E histological stains of the porcine small intestinal tissue showed that fusion without compression produced a decrease in the tissue cross sectional thickness

however the tissue layers and band structures appeared to remain much like that of the native state and produced a median burst pressure of less than 10 mmHg. RF fusion performed with accompanying compression showed a dramatic reduction in fused tissue thickness and significant changes in the tissue layers with the delimitation between the submucosa and mucosa layers becoming less distinguishable as seen in Figure 5-3 and Figure 5-7. Additionally, the upper and lower mucosa of the fused tissue became indistinguishable from one another in the histological sections, white light micrographs and Raman maps. Fusion is therefore demonstrated by the unification of the mucosa during fusion along with the increase in burst pressure.

Tissue fused without compression appears to undergo some molecular restructuring as indicated in the mean plots (Figure 5-4) and shown in the Amide I maximum peak shift in Figure 5-5 may be expected due to exposure to higher temperatures. This molecular restructuring appears to be less collagen dependent as shown in the Raman difference plots in Figure 5-6(b) with the collagen difference spectrum highlighting fewer distinct band shifts in compressed tissue versus non-compressed tissue. This may be attributed to more collagen bond restructuring with the additional mechanical pressure during fusion introduced with tissue compression.

Particular consideration to Raman spectral background changes was taken during the analysis of the Raman tissue maps as fibre and water content may alter the Raman background signal. A polynomial fit was used to remove the background and spectra were normalised before comparing means directly or through difference spectra. Changes within the Raman spectral backgrounds were in line with expectations with the fused regions being denser, less hydrated and less organised into distinct tissue layers. Some of the difference spectra were not considered (namely 0.3 MPa CP) as those tissue areas showed less than three spectra with an abundance value greater than 0.6 for the collagen rich endmembers. When comparing difference spectra it is also important to note that the collected Raman spectra are semi-quantitative thus general trends (peak shifts and shape changes) are important rather than absolute intensity differences. Future studies using a smaller mapping step sizes and/or a larger tissue section may be considered to improve upon these challenges.

5.6 Conclusions

For the first time the use of Raman spectroscopy to characterize fused tissues in RF heat-induced tissue fusion was proposed and demonstrated. It was discovered that

tissue restructuring, or more specifically tissue layer and collagen molecular restructuring in the fusion areas, seems to be a contributing mechanism for a strong fusion. These results suggest a decrease in non-reducible collagen crosslinks and an increase in reducible collagen crosslinks occur during fusion. These changes are associated with collagen undergoing heat treatment and this restructuring provides new insight into the effects of RF fusion on the biochemical changes in the native collagen. Additionally, the presence of compression pressure during fusion produced a difference in collagen restructuring. Tissues fused with compression showed an increase in collagen transformation while tissues fused without compression showed collagen changes associated with a heat treatment.

The correlation between the Raman maps and the histological maps supports the utilisation of Raman spectroscopy in the investigation of RF fusion quality and tissue restructuring. Raman spectroscopy allowed for highly spatially resolved mapping which provided biochemical information without suffering from hydration and tissue density changes between the healthy and fused tissue. The information rich nature of the collected Raman spectra combined with multivariate statistical analysis allowed the selection and comparison of the collagen content between tissue sections of interest. These high resolution maps were collected from four independent samples and further studies are required to fully describe the molecular changes occurring during fusion. The abilities of Raman mapping are of further interest when investigations of RF fusion and comparable techniques are compared in situ and in vivo. Raman microscopy has been demonstrated to be translatable into the clinical setting [195-197]. Thus the rapid, non-destructive, hydration and dehydration-compatible technique utilised in this study holds promise to further elicit information in the translation of the technique to bowel anastomoses.

Overall these insights are the first to demonstrate the previously suspected involvement of collagen in RF tissue fusion, both with and without concurrent compression, using Raman spectroscopy. These molecular insights help provide information on the transformation occurring due to RF fusion as well as inspiration for future investigations into optical feedback methods.

5.7 Future Works

The work presented in this study demonstrates the ability of Raman spectroscopy to be non-invasively applied to tissues of interest and deliver biomolecular insights

through multivariate analysis. The potential of the regular use of Raman spectroscopy in a clinical and more specifically surgical setting increases with technological advancements serving to improve the collection and analytical power of Raman spectroscopy. There are many factors to consider when applying this technology to the clinical arena including the confidence of the results and the ease in translation of the high dimensional datasets into medically relevant information. Raman spectroscopic probes have already shown demonstrated ability to collect information in vivo in studies including intravascular atherosclerosis testing [16], gastrointestinal tissues during routine clinical endoscopy [17], cervical normal and abnormal cells [18], and intraoperative margin assessment of breast tissue during partial mastectomy procedures [198] to highlight a few.

Transferring Raman spectroscopy from a microscopic in vitro environment to in vivo real time diagnostics takes advantage of ability to deliver and collect light via optical fibres which can be incorporated into catheters, endoscopes, cannulas, needles, and in this previous study, the RF fusion device. Raman spectroscopy has a demonstrated ability to image chemical changes in tissues which may be useful in cases where a biopsy cannot be readily performed, such as in coronary artery disease and Alzheimer's. The option of a non-invasive follow up or confirmation technique may reduce the incident of false positive screenings leading to unnecessary medical procedures. Utilizing Raman spectroscopy to analyse tissue during the development and confirmation of this RF tissue fusion device also serves the purpose of building up a dataset, confirming the ability of Raman to analyse fused and healthy tissue, and allows for the consideration of Raman probe in the next generation to device designs.

The Raman spectra in this study were collected over carefully prepared sections of tissue allowing for a microscopic inspection. This aided in the analysis and allowed for a direct comparison to histology. Even with this preparation, each mapped area underwent independent analysis so as to alleviate the potential background influence which may be introduced due to sample thickness variation, focal depth and differences arising from sample preparation and sectioning. The continuation of using Raman spectroscopy on samples undergoing RF fusion would allow for the establishment of a spectral database and the determination of more robust analytical techniques which would help select potential methods for moving forward into *in vivo* imaging.

6 Conclusions and Future Work

Raman micro-spectroscopy is continuing to prove to be a powerful technique in providing molecular insight into biological studies. Throughout this thesis Raman micro-spectroscopy has demonstrated the ability to further expose chemical differences or similarities between experimental groups of interest.

Analytical tools which help researchers visualize critical differences between subject groups were explored in this thesis. Three studies demonstrated how PLS-DA VIP score plots can capture the changes across the entire interrogated spectral range in an 'easy to read' manner. The studies supporting the incorporation of PLS-DA VIP score plots included examining HeLa cells in various states (live, fixed, dehydrated, and rehydrated), osteoportic vs. healthy bone, and human cardiovascular tissue in various conditions. These studies helped to establish PLS-DA VIP score plots are useful to the visualization of spectral ranges which distinguish between groups however these ranges must be further translated into molecular changes which requires a certain degree of interpretation. This suggests this technique may be best accompanied by complimentary techniques to expose which spectral ranges to prioritize for investigation despite the intensity found in these heatmaps. This is demonstrated in the HeLa cells study as spectral regions highlighted between groups included protein, phospholipids, lipids, and DNA changes as expected based on literature however a prioritization of changes beyond an increase or decrease in content were not achieved. When applied to human calcified cardiovascular tissue each highlighted region was further researched and specific (often high intensity on the PLS-DA VIP heatmap) spectral regions thus molecular changes where identified however not immediately using these 'easy to read' plots.

A large part of the work presented here focused specifically on aortic valve calcification with some work on vascular calcification. A PAVICs study provided information on the distinct lack of calcification in a model used previously to represent 'calcified' nodules which is a critical insight for further use of these systems and similar model systems. Additionally this study identified the abundant production of type I collagen within these nodular systems. This study met the aim to characterize the PAVICs cellular system with respects of interrogating the mineral and organic content. The resulting identified components may help future studies determine the

appropriate place, if any, for this cellar system as a model of aortic valve disease progression.

A calcified human cardiovascular tissue study was performed in an effort to determine if changes were occurring in the organic matrix surrounding microscopic mineral inclusions (which were recently discovered and characterized) and if so, aimed to identify some of these changes. Changes were identified in the Raman spectra which distinguished between tissues with and without these microscopic mineral inclusions. This helped to satisfy one objective by suggesting organic changes where occurring colocalised with the microscopic mineral deposits. The second objective of identifying these changes leaves some room for further study. Spectral features were identified suggesting collagen changes are occurring in tissues containing microscopic mineral spheres in comparison to those without. This helps to identify one potential candidate for further study however other candidates and the significance of this potential collagen change was not determined.

Raman microscopic mapping was utilized in different parts of this thesis to provide a more granular perspective to biological systems including the previously mentioned PAVICs *in vitro* nodules and heat induced tissue fusion. In the tissue fusion study, the mapping allowed for the comparison of healthy independent bowel segments and fused tissue sections exposing the collagen restructuring occurring post tissue fusion. The collagen restructuring identified in this study was specifically collagen crosslink changes in the way of increased reducible crosslinks and decreased non-reducible cross links. Further study is required however to fully reach the aim of identifying if these changes are responsible for the integrity of the strong seal which is formed when tissue is fused in this manner.

Some suggestions for future research from each study in this thesis are outlined at the end of each chapter. The following section briefly addresses some general trends and possible future directions for Raman micro-spectroscopy in biological and clinical studies.

6.1 Using accessible tools for the analysis of Raman spectroscopic results

The work presented in this thesis demonstrates the application potential of Raman spectroscopy as well as its ability to test live *in vitro* cellular models, classify human tissue of interest, and determine the biomolecular differences in tissue samples which are diseased or undergoing treatment. Additionally new ways of visualizing and interpreting multivariate analytical results are shown for the ease of determining the biomolecular features which are most important when comparing sample groups. There remain careful considerations when applying this powerful technique to future biological studies including the continuation of the works presented in this thesis.

The challenges of analysing and interpreting the data rich Raman spectra collected from biological samples have been highlighted extensively in this thesis. The techniques and tools used to overcome these challenges differ between researchers. There is an extensive range in the tools used for preprocessing and modelling which often are tailored for the study of interest but also vary for the personal preference and familiarity of the research group. In chapter 2 of this thesis there is a discussion on the way to portray the VIP scores and the heat maps were one of several options including a simple 2D plot alongside the mean spectra or as demonstrated in the Xia and Wishart's paper, a list of spectral component highlighted on the y-axis and the VIP scored on the X-axis [101]. The flexibility in the analysis allows for tailoring to the great range of biological samples however does have drawbacks in the ability to compare, fairly, various studies of similar materials.

The work in this thesis often used commercially available software such as the PLS_toolbox from Eigenvector research. Although at times it was determined necessary to use in-house written scripts and sometimes a hybrid between in house written scripts and commercial toolboxes, there are distinct advantages to using the commercial software. The use of commercial software allows for more ready reproducibility by other research groups interested in a similar type of analysis and also allows for a better discussion on the results with such groups. Additionally the toolboxes used are not used solely for Raman spectral analysis and thus the advancements made in other research arenas can more easily be translated into Raman spectral analysis if incorporating the same platforms. Finally if and when Raman systems are incorporated into surgical or cell culture environments there are

advantages to using commercial software as it has already been applied to studies establishing Raman spectroscopic imaging of tissues as seen in this thesis and other studies using Raman spectroscopic systems in vivo [14,17].

6.2 Raman micro-spectroscopy in monitoring live cells in culture

The advantages of utilizing Raman spectroscopy in biological application include its ability to rapidly, non-invasively collect a wealth of chemical data from hydrated samples. In the studies provided in this thesis Raman spectroscopy was performed before the samples were then taken for further complimentary testing with labelling, altering, or destructive techniques (staining, SEM imaging, FIB, etc.). The advantages to subsequent testing are it offers complimentary information on the same sample and further validation of points of interest. This does however leave time course studies to be performed on independent samples as ultimately Raman testing was conducted in a non-sterile environment leaving the samples exposed to contaminates which disallows for further culture. Additionally there is a substrate consideration as the substrates best used for Raman are less cell compatible as tissue culture plastic and more expensive.

In future studies with various time points or continuous monitoring is necessary, Raman spectroscopy can still be used independently to provide biomolecular feedback in-vitro and in-vivo without a need to sacrifice those samples. A study by Pascut et al. recently demonstrated this by monitoring the cardiac differentiation of human embryonic stem cells in-vitro in purpose-built micro-bioreactors used on the Raman microscope for five days [10]. This study also included time-course mapping of embryoid bodies and ultimately demonstrated the ability of in-situ non-invasive monitoring of cells cultured in vitro. Many researchers from this study also reported dramatically reducing the time it takes to phenotypically identify human embryonic stems cells which would also may aid in the quest for utilizing Raman spectroscopy in cell sorting application [199]. Taken together these studies and others are showcasing another dimension in utilizing Raman spectroscopy as a powerful tool in cell culture [200-202]. Many challenges of robustly incorporating this technology in cell culture environments include maintaining sterile conditions so multiple cultures could be imaged using the same instrument, producing easy-to-read results and the seamless

integration of the Raman system with equipment already used in the lab (microscopes, cell culture hoods, etc.).

6.3 Raman spectroscopic imaging of Rheumatic fever cardiac valves

An opportunity to collaborate with a hospital in Aswan, Egypt to investigate Rheumatic fever samples which would be placed in 4% PFA and transferred to the London, U.K. arose and a few samples were transferred across for initial testing. Within the tissue of these samples a form of precipitation occurred which is still unidentifiable. This precipitation showed distinct peaks in the collected Raman spectra and distinct features in SEM micrographs. There were many factors which could have contributed to such a sample distortion, namely the lack of temperature controlled storage and transportation of both the solutions for fixation and of the samples within the fixative. The potential extreme heat cycling and the transportation delays lead to many possibilities for alteration to occur. The Raman spectral peaks of the unidentified precipitates are shown in Appendix B along with SEM micrographs of those regions as collected by Dr. Sergio Bertazzo. This preliminary investigation served to identify potential conflicts and also served to demonstrate the ability of Raman spectroscopy to expose the content diversity in samples which are not visually detectable.

6.4 Caveat regarding cardiovascular calcification and mechanics

An important caveat within the investigations of cardiovascular calcification presented in this thesis is the absence of monitoring of the biomechanical contributions to disease and model progression. The biomechanical factors including shear stress due to blood flow, radial vessel pressure, alterations due to ECM modifications and mineral deposits, and many more were excluded as they are independently widely studies areas. Although they are not thoroughly mentioned, it is important to make clear their undeniable influence in cardiovascular pathology and almost certain relationship to the diseased processes and possibly specific mechanisms discussed in this thesis. Ultimately the molecular level insight provided within this thesis may help describe and be described by the contributing mechanical factors which are known accompanying players in cardiovascular disease.

6.5 Selection of Raman instrumentation based on application and interest

The microscopic mineral inclusions found within cardiovascular tissues, diseased and visually undisrupted ranged in size from 100nm to 5μm in diameter and were found to be surrounded in a protein rich matrix in visually unperturbed tissues. Using the Raman spectroscopic system described and applied here, the microscopic mineral inclusions were often below the detection limit and sensitivity threshold of the instrumentation. This 'invisibility' was utilised to study the protein rich environment surrounding these mineral deposits and exposed protein changes, and specifically collagen alterations occurring around them. Alternative Raman instrumentation is able to detect such microscopic mineral inclusions as recently reported by Pilarczyk et al. [203]. Pilarczyk et al. utilised a high spatial resolution Raman spectroscopic system with confocal depth profiling for the direct imaging of these microscopic mineral deposits. The collected Raman spectroscopic information was used to identify and classify the mineral deposits found within human aortic valve tissues focusing on the inorganic rather than the organic. Interestingly their study echoed the suggestion of these microscopic spherical mineral inclusions occurring at very early stages of aortic valve calcification. Alternative Raman systems and types of Raman spectroscopy were not described in depth in this text however, it is important to note the application of various systems and adaptations of Raman spectroscopy can provide complimentary molecular level information.

6.6 Applying Raman spectroscopy to Biological Studies

Raman spectroscopy was applied to the imaging of live Hela cells *in vitro*, human bone tissue, PAVICs nodules *in vitro*, human aortic valve and aortic tissue, and porcine blood vessel and bowel tissue. The results demonstrated the rapid, non-invasive, biocompatible nature of Raman spectroscopy, the information rich spectra which are collected, and the sophisticated analysis techniques which are applied to translate those spectral datasets into biologically meaningful information. The inclusion of Raman spectroscopy within each study added a dimension of visualisation exposing protein changes, mineral differences, lipid differences, and distinguishing molecular alterations between seemingly very similar experimental groups. Looking forward, the diversity and range of Raman spectroscopy will undoubtedly expand to meet the many needs of biological research.

Appendix 1

RAMAN PEAKS ASSIGNMENTS

Key:

elastin
collagen assignments
lipids
mineral
protein

vs = very strong
s = strong
m = medium
w = weak

wavenumber (cm^{-1})	strength	peak description / trend observed	assignment	reference
546	w		Cholesterols	12,14
587	m		Phosphate in calcium salts	12,13
606	w		Cholesterols	12,14
699/700	m		Cholesterols	12,14
801/3/4	w		Cholesterols	12,14
814			Protein C-C backbone, proline, hydroxyproline	1,8
841/2	w		Cholesterols	12,14
852-856			hydroxyproline	1
873-879			hydroxyproline	1,11
878/82	w		Cholesterols	
918			C-N proline ring stretch	1
935-938			Protein C-C backbone	1
940			alpha helix	17
957/59	w		Cholesterols	12,14
957/58/60	vs	sharp	Phosphate symmetric stretch in calcium salts	12,13
1003/4			Phenylalanine (of collagen)	1,2,12,15
1067			Proline (collagen assignment)	2
1078			C-C or PO2 stretch (nucleic acid)	3
1071	s		carbonate symmetric and phosphate antisymmetric stretch in calcium salts	12,13
1080			C-C stretching vibrations of fatty acids	12
1084			Phosphodiester groups in nucleic acids	4
1129		sharp	characteristic of all-trans chains (if not present, chains in gauche confirmation)	12
1157	w		Carotenoid	12,16
1240-1280			Amide III band envelope	10
1244/5			Amide III C-N-H stretch - random coil	17
1252/61	m/w		Amide III	12,15,9
1252/61		shift to lower frequencies	spectral signatures of collagen in which crosslinks have been reduced or broken	9
1262/4/7			C-H bending of fatty acids (=C-H)	12
1270			Amide III C-N-H stretch	
1301	m/w		C-H bending of fatty acids (CH_2)	12
1313			CH_3CH_2 collagen twisting mode of collagen	3
1324			CH_3CH_2 wagging mode present in collagen	5
1335		weak band (appears as a shoulder)	specific to elastin	12
1340			elastin	12
1342			CH deformation (proteins and carbohydrates)	6
1440		shifted band from protein peaks, 3x more intense	C-H bending	12
1447		lower freqency shift (by $3cm^{-1}$)	CH_2 wag , shift implicates increased lipid content	12
1441-1447			CH_3, CH_2	8

1450/1	s		Protein	12
1480			Amide II	4
1519	w		Carotenoid	12,16
1544			Amide II	4
1554			Amide II	7
1600-1650		shift to higher frequencies	Amide I C-N-H stretch, shift implicates increase in collagen crosslinks, dehydration ,= spectral signatures of collagen in which crosslinks have been reduced or broken , seen in stretch and damaged collagen	4,12,10
1652-1660			Amide I	8
1655	m		C=C stretch of fatty acids	12
1655		distinguished from amide I by peak frequency and width, FWHM is approx 17cm-1, Amide I FWHM is approx. 60cm^{-1}	stretching C=C groups in unsaturated fatty acid chains	12
1660			nonreducible collagen cross-links	10
1663	m		Amide I	12,15
1678		peak shifted here from lower wavenumbers	deformation of collagen	9
1690			reducible collagen cross-links	10
1746	w		C=O stretching mode of triglyceride ester linkages (indicates lipids are of the triglyceride form)	12

1. Cheng, W.-T., Liu, M.-T., Liu, H.-N. and Lin, S.-Y. 2005. Micro-Raman spectroscopy used to identify and grade human skin pilomatrixoma. *Microscopy Research and Technique*, 68: 75–79

2. Frank, C. J., McCreecy, R. L. and Redd, D. C.B. 1995. Raman spectroscopy of normal and diseased human breast tissues. *Analytical Chemistry*, 67: 777–783.

3. Stone, N., Kendall, C., Smith, J., Crow, P. and Barr, H. 2004. Raman spectroscopy for identification of epithelial cancers. *Faraday Discussion.*, 126: 141–157.

4. Dukor, R. K. 2002. Vibrational spectroscopy in the detection of cancer. *Biomedical Applications*, 5: 3335–3359.

5. Lau, D. P., Huang, Z., Lui, H., Anderson, D. W., Beren, K., Morrison, M. D., Shen, L. and Zeng, H. 2005. Raman spectroscopy for optical diagnosis in the larynx: Preliminary findings. *Lasers in Surgery and Medicine*, 37: 192–200.

6. Notingher, I., Green, C. and Dyer, C. 2004. Discrimination between ricin and sulphur mustard toxicity in vitro using Raman spectroscopy. *Journal of the Royal Society Interface*, 1: 79–90

7. Faolain, E. O., Hunter, M. B., Byrne, J. M., Kelehan, P., McNamer, M., Byrne, H. J. and Lyng, F. M. 2005. A study examining the effects of tissue processing on human tissue sections using vibrational spectroscopy. *Vibrational Spectroscopy*, 38: 121–127.

8. Dong R, Yan X, Pang X,Liu S. Temperature-dependent Raman spectra of collagen and DNA. Spectrochimica Acta Part A: Molecular and Biomolecular Spectroscopy 2004;60:557-561.

9. Carden A, Rajachar RM, Morris MD,Kohn DH. Ultrastructural Changes Accompanying the Mechanical Deformation of Bone Tissue: A Raman Imaging Study. Calcified tissue international 2003;72:166-175.

10. Tarnowski CP, Stewart S, Holder K, Campbell-Clark L, Thoma RJ, Adams AK, et al. Effects of treatment protocols and subcutaneous implantation on bovine pericardium: a Raman spectroscopy study. J Biomed Opt 2003;8:179-184.

11. Frushour BG,Koenig JL. Raman scattering of collagen, gelatin, and elastin. Biopolymers 1975;14:379-391.

12. Baraga JJ, Feld MS,Rava RP. In situ optical histochemistry of human artery using near infrared Fourier transform Raman spectroscopy. Proceedings of the National Academy of Sciences 1992;89:3473-3477.

13. Faiman R. Raman spectroscopic studies of different forms of cholesterol and its derivatives in the crystalline state. Chemistry and physics of lipids 1977;18:84.

14. Sufrà S, Dellepiane G, Masetti G,Zerbi G. Resonance Raman spectrum of β-carotene. Journal of Raman spectroscopy 1977;6:267-272.

15. Carey, P. R. (1982) Biochemical Applications of Raman and Resonance Raman Spectroscopies (Academic, New York).

16. Barnes MJ. COLLAGENS IN ATHEROSCLEROSIS. Collagen and Related Research 1985;5:65-97.

17. Badii F,Howell NK. Elucidation of the Effect of Formaldehyde and Lipids on Frozen Stored Cod Collagen by FT-Raman Spectroscopy and Differential Scanning Calorimetry. Journal of Agricultural and Food Chemistry 2003;51:1440-1446.

Appendix 2

Rheumatic Fever Heart Disease, Calcified Valve Artefacts

Rheumatic fever (RFev) is an inflammatory disease which develops as a complication of inadequately treated infections. RFev can cause permanent damage to heart including damaged heart valves and heart failure. Incidences of RFev have dramatically declined in the developed world partially due accessible medical facilities and anti-biotic treatments. In the developing world RFev remains a major medical and social problem including the complication of heart valve sclerosis and stenosis. The scientific interest on RFev has notably diminished despite its continued prevalence in the developing world [204]. A potential collaboration with an Egyptian hospital was explored to see the feasibility in transporting calcified valves to London for Raman spectroscopic testing. The following information is a brief account of one major consideration of possible precipitates or artefact introduction in such a study and demonstrated the ability of Raman spectroscopy to detect material differences in tissue samples.

Samples preparation:
Human aortic valves surgically removed for replacement were collected for research. Samples were stored in Formalin (time stored uncertain), dehydrated through a graded ethanol series, and lastly stored in desiccators until imaging.

Raman Spectral measurement:
Raman spectra were collected using the Raman system as described in the introduction. Briefly a modified Renishaw InVia Raman dispersive spectrometer system (Renishaw, Wotton-under-Edge, Gloucestershire, UK) connected to a Leica microscope with a 50x objective. The excitation source was a 785 nm diode line focus laser with ~300 mW at source, ~120mW before objective and ~100mW at sample. The sample volume illuminated at the focal plane is roughly elliptical in shape with a minor axis of x≈10 μm, major axis of y≈20 μm and axial resolution of z≈30 μm.

Point Spectral collection:
Each spectrum was collected using 10% laser power, 5 second exposure, 5 accumulations per measurement. Analysis was performed using Matlab R2010b (Mathworks). Spectra were normalized, background subtracted, smoothed and baseline removed.

Results:

Samples from 11 patients were selected for analysis. From visible inspection these ranged in degrees of calcification with many showing no visible calcification. A total of 198 spectra were collected from these 11 samples for comparison. Three spectral environments were identified as shown in figure 1 including protein rich (figure 1A), mineral rich (figure 1B), and a third unidentified material (figure 1C). SEM micrographs were collected from the same tissue samples post Raman imaging. The material producing the unidentified Raman spectral fingerprint is shown in figure 2.

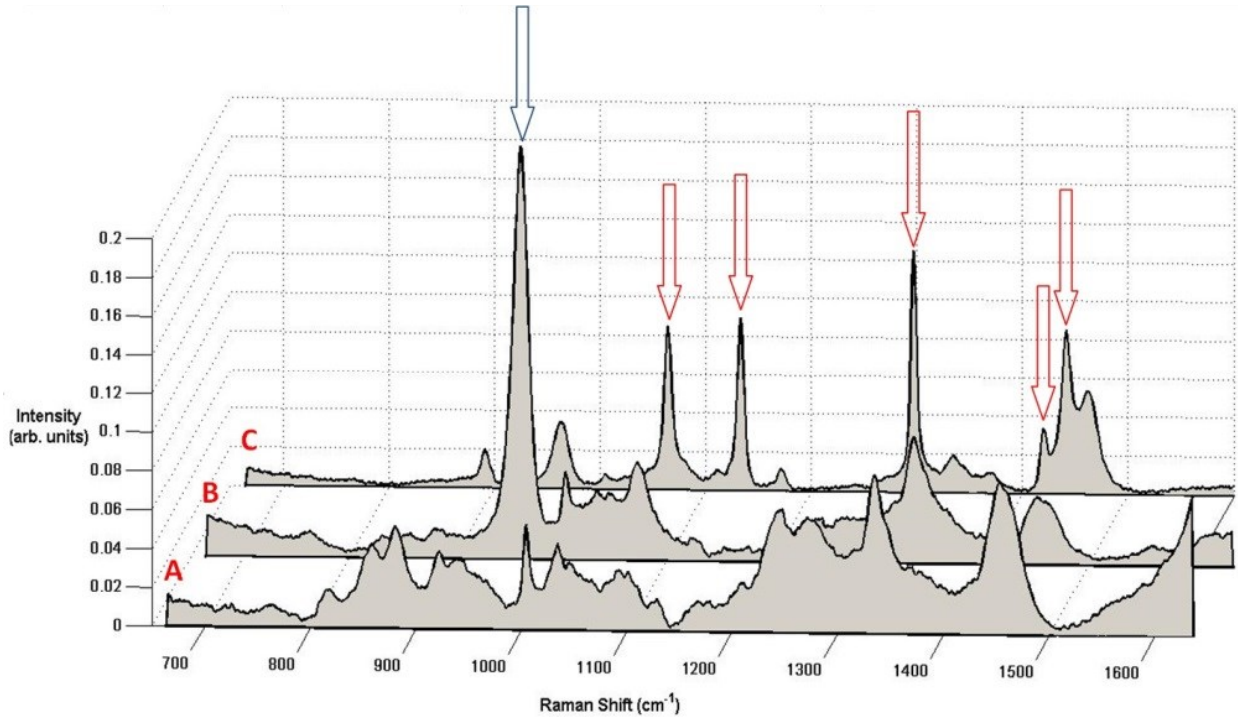

Figure 1: *Mean spectra from three environments present in the Rheumatic fever samples received from Egypt. A. Spectrum displaying typical cellular and extracellular matrix peaks. B. Spectrum displaying strong sharp apatite peak at 960cm^{-1}. Blue arrow in B apatite PO_4 peak C. Spectrum displaying mineral peaks, such as apatite however showing sharp peaks not displayed in A. or B. which corresponds to previously reported peaks found in mineral precipitates. Red arrows in C. indicate peaks which expose possible precipitates.*

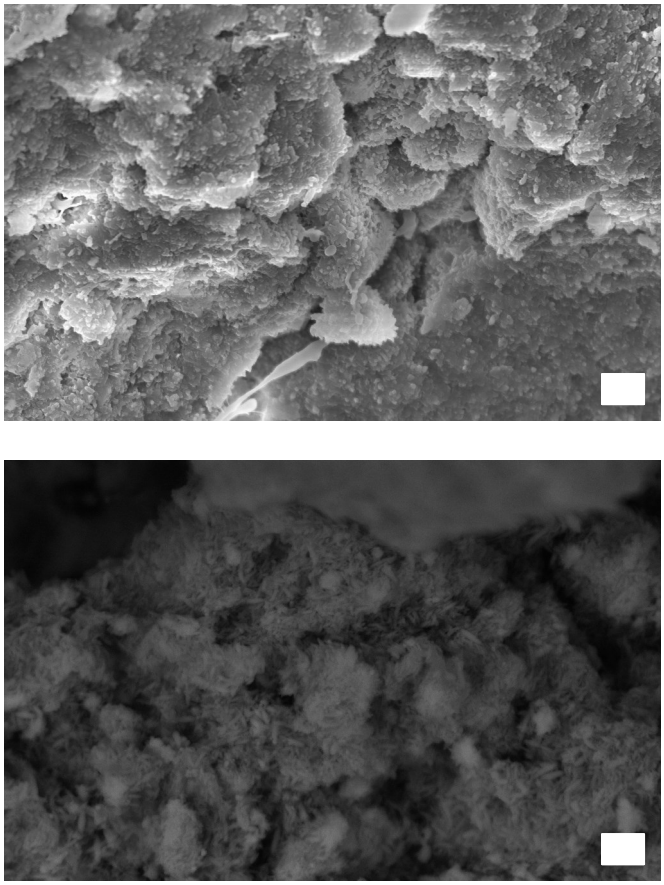

Figure 2: Two SEM micrographs of inorganic crystal deposition found in calcified RF valves as collected and prepared from a hospital in Egypt. Scale bar = 1µm.

Discussion:

Raman spectra collected from the calcified RF valves presented three main biomolecular environments, tissue (rich in protein peaks), apatite (calcium phosphate and calcium phosphate peaks) and an environment not previously associated with soft tissues or phosphate species. The Raman spectra collected from tissue without mineralisation yielded protein rich peaks associated with biological spectra including 855, 874, 1003, 1235-1239, 1480-1575 cm^{-1} corresponding to proline, hydroxyproline, phenylalanine, amide III, and amide I respectively [24] and s seen previously in chapter 4. The 960 and 1070 cm^{-1} apatite and carbonate peaks respectively were found in Raman spectra collected from hard deposits within the tissue of the RF calcified valves and are comparable to those observed in chapter 4. In

contrast to those environments previously identified in cardiac valves with Raman spectroscopy, a third Raman spectral fingerprint appeared showing strong, sharp peaks in location which have been previously identified with calcium carbonates however not collectively with the relative intensities shown [205]. A sharp peak at 1065 cm^{-1} appears which is in range of a peak previously identified as amorphous calcium carbonate [206,207]. The peaks shown in the unidentified material do no correspond to any found PFA peaks.

Conclusions:

The undefined material found in the calcified RF valves compromised all spectra collected from this collection of cardiac valves. Further study using these valves would have to undergo strict chemical, temporal, and temperature controls in order to avoid further artefact introduction. Raman spectra were very useful to determine alterations in the cardiac valve material suggesting it is a useful too not only in the characterisation of material environments but also for the detection of contaminates within biological tissues.

References

1. Raman CV (1928) A new type of secondary radiation. Nature 121: 501.
2. (2013) Nobel Prize in Physics 1930 - Presentation Speech.
3. Notingher I, Jell G, Lohbauer U, Salih V, Hench LL (2004) In situ non‐invasive spectral discrimination between bone cell phenotypes used in tissue engineering. Journal of cellular biochemistry 92: 1180-1192.
4. Notingher I, Verrier S, Romanska H, Bishop A, Polak J, et al. (2002) In situ characterisation of living cells by Raman spectroscopy. Spectroscopy: An International Journal 16: 43-51.
5. Campion A, Kambhampati P (1998) Surface-enhanced Raman scattering. Chemical Society Reviews 27: 241-250.
6. Otto A, Mrozek I, Grabhorn H, Akemann W (1992) Surface-enhanced Raman scattering. Journal of Physics: Condensed Matter 4: 1143.
7. Tolles WM, Nibler J, McDonald J, Harvey A (1977) A review of the theory and application of coherent anti-Stokes Raman spectroscopy (CARS). Applied spectroscopy 31: 253-271.
8. Yuratich M, Hanna D (1977) Coherent anti-Stokes Raman spectroscopy (CARS) Selection rules, depolarization ratios and rotational structure. Molecular Physics 33: 671-682.
9. Cloyd KL, El-Hamamsy I, Boonrungsiman S, Hedegaard M, Gentleman E, et al. (2012) Characterization of Porcine Aortic Valvular Interstitial Cell 'Calcified' Nodules. PLoS ONE 7: e48154.
10. Pascut FC, Kalra S, George V, Welch N, Denning C, et al. (2013) Non-invasive label-free monitoring the cardiac differentiation of human embryonic stem cells in-vitro by Raman spectroscopy. Biochimica et Biophysica Acta (BBA) - General Subjects 1830: 3517-3524.
11. Notingher I, Bisson I, Bishop AE, Randle WL, Polak JMP, et al. (2004) In Situ Spectral Monitoring of mRNA Translation in Embryonic Stem Cells during Differentiation in Vitro. Analytical Chemistry 76: 3185-3193.
12. Gentleman E, Swain RJ, Evans ND, Boonrungsiman S, Jell G, et al. (2009) Comparative materials differences revealed in engineered bone as a function of cell-specific differentiation. Nat Mater 8: 763-770.

13. Shetty G, Kendall C, Shepherd N, Stone N, Barr H (2006) Raman spectroscopy: elucidation of biochemical changes in carcinogenesis of oesophagus. British journal of cancer 94: 1460-1464.
14. Molckovsky A, Song L-MWK, Shim MG, Marcon NE, Wilson BC (2003) Diagnostic potential of near-infrared Raman spectroscopy in the colon: Differentiating adenomatous from hyperplastic polyps. Gastrointestinal Endoscopy 57: 396-402.
15. Shim MG, Wilson BC, Marple E, Wach M (1999) Study of Fiber-Optic Probes for in Vivo Medical Raman Spectroscopy. Appl Spectrosc 53: 619-627.
16. Buschman HP, Marple ET, Wach ML, Bennett B, Bakker Schut TC, et al. (2000) In Vivo Determination of the Molecular Composition of Artery Wall by Intravascular Raman Spectroscopy. Analytical Chemistry 72: 3771-3775.
17. Shim MG, Wong Kee Song L-M, Marcon NE, Wilson BC (2000) In vivo Near-infrared Raman Spectroscopy: Demonstration of Feasibility During Clinical Gastrointestinal Endoscopy Photochemistry and Photobiology 72: 146-150.
18. Utzinger U, Heintzelman DL, Mahadevan-Jansen A, Malpica A, Follen M, et al. (2001) Near-Infrared Raman Spectroscopy for in Vivo Detection of Cervical Precancers. Appl Spectrosc 55: 955-959.
19. Hanlon EB, Manoharan R, Koo TW, Shafer KE, Motz JT, et al. (2000) Prospects for in vivo Raman spectroscopy. Physics in Medicine and Biology 45: R1.
20. Manoharan R, Wang Y, Feld MS (1996) Histochemical analysis of biological tissues using Raman spectroscopy. Spectrochimica Acta Part A: Molecular and Biomolecular Spectroscopy 52: 215-249.
21. Lord RC, Yu N-t (1970) Laser-excited Raman spectroscopy of biomolecules: I. Native lysozyme and its constituent amino acids. Journal of Molecular Biology 50: 509-524.
22. Rothschild KJ, Andrew JR, De Grip WJ, Stanley HE (1976) Opsin structure probed by Raman spectroscopy of photoreceptor membranes. Science 191: 1176-1178.
23. Prescott B, Steinmetz W, Thomas GJ (1984) Characterization of DNA structures by laser Raman spectroscopy. Biopolymers 23: 235-256.
24. Movasaghi Z, Rehman S, Rehman IU (2007) Raman Spectroscopy of Biological Tissues. Applied Spectroscopy Reviews 42: 493-541.
25. Tarnowski CP, Ignelzi MA, Morris MD (2002) Mineralization of developing mouse calvaria as revealed by Raman microspectroscopy. Journal of Bone and Mineral Research 17: 1118-1126.

26. Gough J, Notingher I, Hench L (2004) Osteoblast attachment and mineralized nodule formation on rough and smooth 45S5 bioactive glass monoliths. Journal of Biomedical Materials Research Part A 68: 640-650.
27. Boskey AL, Mendelsohn R (2005) Infrared spectroscopic characterization of mineralized tissues. Vibrational spectroscopy 38: 107-114.
28. Penel G, Leroy G, Rey C, Bres E (1998) MicroRaman spectral study of the PO4 and CO3 vibrational modes in synthetic and biological apatites. Calcified tissue international 63: 475-481.
29. Swain RJ (2008) Non-invasive biochemical analysis of cells, tissues and tissue constructs with Raman micro-spectroscopy [Ph.D.]. London, U.K.: Imperial College London.
30. Carden A, Morris MD (2000) Application of vibrational spectroscopy to the study of mineralized tissues (review). Journal of Biomedical Optics 5: 259-268.
31. Akkus O, Adar F, Schaffler MB (2004) Age-related changes in physicochemical properties of mineral crystals are related to impaired mechanical function of cortical bone. Bone 34: 443-453.
32. Draper ER, Morris MD, Camacho NP, Matousek P, Towrie M, et al. (2005) Novel Assessment of Bone Using Time‐Resolved Transcutaneous Raman Spectroscopy. Journal of Bone and Mineral Research 20: 1968-1972.
33. Awonusi A (2007) Carbonate assignment and calibration in the Raman spectrum of apatite. Calcified tissue international 81: 46.
34. Savitzky A, Golay MJE (1964) Smoothing and Differentiation of Data by Simplified Least Squares Procedures. Analytical Chemistry 36: 1627-1639.
35. Lieber CA, Mahadevan-Jansen A (2003) Automated Method for Subtraction of Fluorescence from Biological Raman Spectra. Appl Spectrosc 57: 1363-1367.
36. Martens H, Nielsen JP, Engelsen SB (2003) Light Scattering and Light Absorbance Separated by Extended Multiplicative Signal Correction. Application to Near-Infrared Transmission Analysis of Powder Mixtures. Analytical Chemistry 75: 394-404.
37. Wold S, Sjöström M, Eriksson L (2001) PLS-regression: a basic tool of chemometrics. Chemometrics and Intelligent Laboratory Systems 58: 109-130.
38. Barker M, Rayens W (2003) Partial least squares for discrimination. Journal of Chemometrics 17: 166-173.

39. Hedegaard M, Krafft C, Ditzel HJ, Johansen LE, Hassing S, et al. (2010) Discriminating isogenic cancer cells and identifying altered unsaturated fatty acid content as associated with metastasis status, using k-means clustering and partial least squares-discriminant analysis of Raman maps. Analytical Chemistry 82: 2797-2802.
40. Heraud P, Wood BR, Beardall J, McNaughton D (2006) Effects of pre-processing of Raman spectra on in vivo classification of nutrient status of microalgal cells. Journal of Chemometrics 20: 193-197.
41. Mello C, Ribeiro D, Novaes F, Poppi RJ (2005) Rapid differentiation among bacteria that cause gastroenteritis by use of low-resolution Raman spectroscopy and PLS discriminant analysis. Analytical and Bioanalytical Chemistry 383: 701-706.
42. Palermo G, Piraino P, Zucht H-D (2009) Performance of PLS regression coefficients in selecting variables for each response of a multivariate PLS for omics-type data. Advances and applications in bioinformatics and chemistry: AABC 2: 57.
43. Matthäus C, Chernenko T, Quintero L, Milan L, Kale A, et al. (2008) Raman microscopic imaging of cells and applications monitoring the uptake of drug delivery systems. 699106-699106.
44. Hedegaard M, Matthäus C, Hassing S, Krafft C, Diem M, et al. (2011) Spectral unmixing and clustering algorithms for assessment of single cells by Raman microscopic imaging. Theoretical Chemistry Accounts 130: 1249-1260.
45. Butler D (2011) UN targets top killers. Nature 477: 260-261.
46. Speer MY, Giachelli CM (2004) Regulation of cardiovascular calcification. Cardiovascular Pathology 13: 63-70.
47. Boström K, Watson K, Horn S, Wortham C, Herman I, et al. (1993) Bone morphogenetic protein expression in human atherosclerotic lesions. Journal of Clinical Investigation 91: 1800.
48. Mohler ER, Gannon F, Reynolds C, Zimmerman R, Keane MG, et al. (2001) Bone Formation and Inflammation in Cardiac Valves. Circulation 103: 1522-1528.
49. Miller JD (2013) Cardiovascular calcification: Orbicular origins. Nature materials 12: 476-478.
50. Demer LL (1995) A Skeleton in the Atherosclerosis Closet. Circulation 92: 2029-2032.
51. Bertazzo S, Gentleman E, Cloyd KL, Chester AH, Yacoub MH, et al. (2013) Nano-analytical electron microscopy reveals fundamental insights into human cardiovascular tissue calcification. Nature materials 12: 576-583.

52. Roberts WC, Ko JM (2005) Frequency by decades of unicuspid, bicuspid, and tricuspid aortic valves in adults having isolated aortic valve replacement for aortic stenosis, with or without associated aortic regurgitation. Circulation 111: 920-925.

53. Otto CM, Burwash IG, Legget ME, Munt BI, Fujioka M, et al. (1997) Prospective study of asymptomatic valvular aortic stenosis clinical, echocardiographic, and exercise predictors of outcome. Circulation 95: 2262-2270.

54. Hakuno D, Fukuda K (2007) Role of anti-angiogenic factor chondromodulin-I for maintaining cardiac valvular function. Clin Calcium 17: 361-372.

55. Schoen FJ, Edwards WD (2001) Cardiovascular Pathology : Valvular heart disease: general principles and stenosis. New York, NY: Churchill Livingtone.

56. images ADAM (accessed : 20-09-2010) Heart Valve Surgery. In: http://www.medhelp.org/medical-information/show/3962/Heart-valve-surgery---series, editor. internet: A.D.A.M. images.

57. Sacks MS, Yoganathan AP (2007) Heart valve function: a biomechanical perspective. Philosophical Transactions of the Royal Society B: Biological Sciences 362: 1369-1391.

58. Mulholland DL, Gotlieb AI (1996) Cell biology of valvular interstitial cells. The Canadian journal of cardiology 12: 231-236.

59. Marron K, Yacoub MH, Polak JM, Sheppard MN, Fagan D, et al. (1996) Innervation of human atrioventricular and arterial valves. Circulation 94: 368-375.

60. Osman L, Yacoub MH, Latif N, Amrani M, Chester AH (2006) Role of Human Valve Interstitial Cells in Valve Calcification and Their Response to Atorvastatin. Circulation 114: I-547-I-552.

61. Tanaka K, Sata M, Fukuda D, Suematsu Y, Motomura N, et al. (2005) Age-associated aortic stenosis in apolipoprotein E-deficient mice. Journal of the American College of Cardiology 46: 134-141.

62. Yip CYY, Chen J-H, Zhao R, Simmons CA (2009) Calcification by Valve Interstitial Cells Is Regulated by the Stiffness of the Extracellular Matrix. Arteriosclerosis, thrombosis, and vascular biology 29: 936-942.

63. El-Hamamsy I, Balachandran K, Yacoub MH, Stevens LM, Sarathchandra P, et al. (2009) Endothelium-dependent regulation of the mechanical properties of aortic valve cusps. Journal of the American College of Cardiology 53: 1448-1455.

64. Lester WM, Damji AA, Gedeon I, Tanaka M (1993) Interstitial cells from the atrial and ventricular sides of the bovine mitral valve respond differently to denuding endocardial injury. In Vitro Cellular & Developmental Biology-Animal 29: 41-50.
65. Otto CM (2008) Calcific Aortic Stenosis — Time to Look More Closely at the Valve. New England Journal of Medicine 359: 1395-1398.
66. Demer LL, Tintut Y (2008) Vascular Calcification: Pathobiology of a Multifaceted Disease. Circulation 117: 2938-2948.
67. Hoffmann G, Lutter G, Cremer J (2008) Durability of bioprosthetic cardiac valves. Deutsches Arzteblatt international 105: 143.
68. Vesely I (2005) Heart valve tissue engineering. Circulation Research 97: 743-755.
69. Taylor PM, Batten P, Brand NJ, Thomas PS, Yacoub MH (2003) The cardiac valve interstitial cell. The International Journal of Biochemistry & Cell Biology 35: 113-118.
70. Kim K. Calcification of matrix vesicles in human aortic valve and aortic media; 1976. pp. 156-162.
71. Walker GA, Guerrero IA, Leinwand LA (2001) Myofibroblasts: molecular crossdressers. Current topics in developmental biology 51: 91-107.
72. Brand NJ, Roy A, Hoare G, Chester A, Yacoub MH (2006) Cultured interstitial cells from human heart valves express both specific skeletal muscle and non-muscle markers. The International Journal of Biochemistry & Cell Biology 38: 30-42.
73. Dreger S, Taylor P, Allen S, Yacoub M (2002) Profile and localization of matrix metalloproteinases (MMPs) and their tissue inhibitors (TIMPs) in human heart valves. The Journal of heart valve disease 11: 875.
74. Liu AC, Joag VR, Gotlieb AI (2007) The Emerging Role of Valve Interstitial Cell Phenotypes in Regulating Heart Valve Pathobiology. The American journal of pathology 171: 1407-1418.
75. Paruchuri S, Yang J-H, Aikawa E, Melero-Martin JM, Khan ZA, et al. (2006) Human pulmonary valve progenitor cells exhibit endothelial/mesenchymal plasticity in response to vascular endothelial growth factor-A and transforming growth factor-β2. Circulation Research 99: 861-869.
76. Chen J-H, Yip CYY, Sone ED, Simmons CA (2009) Identification and Characterization of Aortic Valve Mesenchymal Progenitor Cells with Robust Osteogenic Calcification Potential. The American journal of pathology 174: 1109-1119.

77. Chalajour F, Treede H, Gehling UM, Ebrahimnejad A, Boehm DH, et al. (2007) Identification and characterization of cells with high angiogenic potential and transitional phenotype in calcific aortic valve. Experimental cell research 313: 2326-2335.

78. Kershaw J, Misfeld M, Sievers H-H, Yacoub MH, Chester AH (2004) Specific regional and directional contractile responses of aortic cusp tissue. The Journal of heart valve disease 13: 798-803.

79. Filip D, Radu A, Simionescu M (1986) Interstitial cells of the heart valves possess characteristics similar to smooth muscle cells. Circulation Research 59: 310-320.

80. Messier RH, Bass BL, Aly HM, Jones JL, Domkowski PW, et al. (1994) Dual structural and functional phenotypes of the porcine aortic valve interstitial population: characteristics of the leaflet myofibroblast. Journal of Surgical Research 57: 1-21.

81. Masters KS, Shah DN, Leinwand LA, Anseth KS (2005) Crosslinked hyaluronan scaffolds as a biologically active carrier for valvular interstitial cells. Biomaterials 26: 2517-2525.

82. Johnson CM, Hanson MN, Helgeson SC (1987) Porcine cardiac valvular subendothelial cells in culture: Cell isolation and growth characteristics. Journal of Molecular and Cellular Cardiology 19: 1185-1193.

83. Lester W, Rosenthal A, Granton B, Gotlieb A (1988) Porcine mitral valve interstitial cells in culture. Laboratory investigation; a journal of technical methods and pathology 59: 710-719.

84. Gotlieb A, Spector W (1981) Migration into an in vitro experimental wound: a comparison of porcine aortic endothelial and smooth muscle cells and the effect of culture irradiation. The American journal of pathology 103: 271.

85. Zacks S, Rosenthal A, Granton B, Havenith M, Opas M, et al. (1991) Characterization of Cobblestone mitral valve interstitial cells. Archives of pathology & laboratory medicine 115: 774.

86. Rajamannan NM, Subramaniam M, Caira F, Stock SR, Spelsberg TC (2005) Atorvastatin inhibits hypercholesterolemia-induced calcification in the aortic valves via the Lrp5 receptor pathway. Circulation 112: I-229-I-234.

87. Krafft C, Dietzek B, Popp J (2009) Raman and CARS microspectroscopy of cells and tissues. Analyst 134: 1046-1057.

88. Krafft C, Belay B, Bergner N, Romeike BF, Reichart R, et al. (2012) Advances in optical biopsy–correlation of malignancy and cell density of primary brain tumors using Raman microspectroscopic imaging. Analyst 137: 5533-5537.
89. Bergholt MS, Zheng W, Huang Z (2012) Characterizing variability in in vivo Raman spectroscopic properties of different anatomical sites of normal tissue in the oral cavity. Journal of Raman spectroscopy 43: 255-262.
90. Neugebauer U, Bocklitz T, Clement J, Krafft C, Popp J (2010) Towards detection and identification of circulating tumour cells using Raman spectroscopy. Analyst 135: 3178-3182.
91. Swain RJ, Kemp SJ, Goldstraw P, Tetley TD, Stevens MM (2008) Spectral monitoring of surfactant clearance during alveolar epithelial type II cell differentiation. Biophysical journal 95: 5978-5987.
92. Notingher I, Jell G, Notingher PL, Bisson I, Tsigkou O, et al. (2005) Multivariate analysis of Raman spectra for in vitro non-invasive studies of living cells. Journal of Molecular Structure 744–747: 179-185.
93. Swain R, Stevens M (2007) Raman microspectroscopy for non-invasive biochemical analysis of single cells. Biochemical Society Transactions 35: 544-550.
94. Swain RJ, Kemp SJ, Goldstraw P, Tetley TD, Stevens MM (2010) Assessment of cell line models of primary human cells by Raman spectral phenotyping. Biophysical journal 98: 1703-1711.
95. Bocklitz T, Putsche M, Stüber C, Käs J, Niendorf A, et al. (2009) A comprehensive study of classification methods for medical diagnosis. Journal of Raman spectroscopy 40: 1759-1765.
96. Sattlecker M, Baker R, Stone N, Bessant C (2011) Support vector machine ensembles for breast cancer type prediction from mid-FTIR micro-calcification spectra. Chemometrics and Intelligent Laboratory Systems 107: 363-370.
97. Sattlecker M, Stone N, Smith J, Bessant C (2011) Assessment of robustness and transferability of classification models built for cancer diagnostics using Raman spectroscopy. Journal of Raman spectroscopy 42: 897-903.
98. Krafft C, Salzer R, Seitz S, Ern C, Schieker M (2007) Differentiation of individual human mesenchymal stem cells probed by FTIR microscopic imaging. Analyst 132: 647-653.

99. Lasch P, Haensch W, Naumann D, Diem M (2004) Imaging of colorectal adenocarcinoma using FT-IR microspectroscopy and cluster analysis. Biochimica et Biophysica Acta (BBA)-Molecular Basis of Disease 1688: 176-186.

100. Bryan K, Brennan L, Cunningham P (2008) MetaFIND: A feature analysis tool for metabolomics data. BMC Bioinformatics 9: 470.

101. Xia J, Wishart DS (2011) Web-based inference of biological patterns, functions and pathways from metabolomic data using MetaboAnalyst. Nature Protocols 6: 743-760.

102. Kohler A, Kirschner C, Oust A, Martens H (2005) Extended multiplicative signal correction as a tool for separation and characterization of physical and chemical information in Fourier transform infrared microscopy images of cryo-sections of beef loin. Applied spectroscopy 59: 707-716.

103. Chong I-G, Jun C-H (2005) Performance of some variable selection methods when multicollinearity is present. Chemometrics and Intelligent Laboratory Systems 78: 103-112.

104. Kvalheim OM (2010) Interpretation of partial least squares regression models by means of target projection and selectivity ratio plots. Journal of Chemometrics 24: 496-504.

105. Rajalahti T, Arneberg R, Berven FS, Myhr K-M, Ulvik RJ, et al. (2009) Biomarker discovery in mass spectral profiles by means of selectivity ratio plot. Chemometrics and Intelligent Laboratory Systems 95: 35-48.

106. Wold S, Johansson E, Cocchi M (1993) PLS—partial least squares projections to latent structures. 3D QSAR in drug design 1: 523-550.

107. Meade AD, Clarke C, Draux F, Sockalingum GD, Manfait M, et al. (2010) Studies of chemical fixation effects in human cell lines using Raman microspectroscopy. Analytical and Bioanalytical Chemistry 396: 1781-1791.

108. Mariani MM, Lampen P, Popp J, Wood BR, Deckert V (2009) Impact of fixation on in vitro cell culture lines monitored with Raman spectroscopy. Analyst 134: 1154-1161.

109. Oxlund H, Sekilde L, Ørtoft G (1996) Reduced concentration of collagen reducible cross links in human trabecular bone with respect to age and osteoporosis. Bone 19: 479-484.

110. Khosla S, Melton LJ, Atkinson EJ, O'fallon W, Klee GG, et al. (1998) Relationship of serum sex steroid levels and bone turnover markers with bone mineral density in

men and women: a key role for bioavailable estrogen. Journal of Clinical Endocrinology & Metabolism 83: 2266-2274.

111. Beck TJ, Ruff CB, Scott Jr WW, Plato CC, Tobin JD, et al. (1992) Sex differences in geometry of the femoral neck with aging: a structural analysis of bone mineral data. Calcified tissue international 50: 24-29.

112. Yacoub MH, Kilner PJ, Birks EJ, Misfeld M (1999) The aortic outflow and root: a tale of dynamism and crosstalk. The Annals of Thoracic Surgery 68: S37-S43.

113. El Hamamsy I (2010) Long-term outcomes after autograft versus homograft aortic root replacement in adults with aortic valve disease: a randomised controlled trial. Lancet 376: 524-531.

114. Chester AH (2011) Molecular and cellular mechanisms of valve calcification. Aswan Heart Centre Science & Practice Series 2011: 4.

115. Frederick J S Cardiac valves and valvular pathology: Update on function, disease, repair, and replacement. Cardiovascular Pathology 14: 189-194.

116. Yacoub MH, Takkenberg JJM (2005) Will heart valve tissue engineering change the world? Nature clinical practice cardiovascular medicine 2: 60-61.

117. Freeman RV, Otto CM (2005) Spectrum of Calcific Aortic Valve Disease. Circulation 111: 3316-3326.

118. O'Brien KD (2006) Pathogenesis of Calcific Aortic Valve Disease. Arteriosclerosis, thrombosis, and vascular biology 26: 1721-1728.

119. Schoen FJ (2008) Evolving Concepts of Cardiac Valve Dynamics. Circulation 118: 1864-1880.

120. Cawley PJ (2009) Prevention of calcific aortic valve stenosis-fact or fiction? Annals of medicine (Helsinki) 41: 100-108.

121. Elmariah S (2010) The Pathogenesis and treatment of the valvulopathy of aortic stenosis: Beyond the SEAS. Current Cardiology Reports 12: 125-132.

122. Durbin AD, Gotlieb AI Advances towards understanding heart valve response to injury. Cardiovascular Pathology 11: 69-77.

123. Rajamannan NM (2003) Human aortic valve calcification is associated with an osteoblast phenotype. Circulation 107: 2181-2184.

124. Jian B, Narula N, Li Q-y, Mohler ER, III, Levy RJ (2003) Progression of aortic valve stenosis: TGF-{beta}1 is present in calcified aortic valve cusps and promotes aortic valve interstitial cell calcification via apoptosis. Ann Thorac Surg 75: 457-465.

125. Clark-Greuel JN, Connolly JM, Sorichillo E, Narula NR, Rapoport HS, et al. (2007) Transforming Growth Factor-{beta}1 Mechanisms in Aortic Valve Calcification: Increased Alkaline Phosphatase and Related Events. Ann Thorac Surg 83: 946-953.
126. Kennedy JA, Hua X, Mishra K, Murphy GA, Rosenkranz AC, et al. (2009) Inhibition of calcifying nodule formation in cultured porcine aortic valve cells by nitric oxide donors. European Journal of Pharmacology 602: 28-35.
127. Mikroulis D (2002) Physicochemical and microscopical study of calcific deposits from natural and bioprosthetic heart valves. Comparison and implications for mineralization mechanism. Journal of materials science Materials in medicine 13: 885-889.
128. Dorfmuller P, Bazin D, Aubert S, Weil R, Brisset F, et al. (2010) Crystalline Ultrastructures, Inflammatory Elements, and Neoangiogenesis Are Present in Inconspicuous Aortic Valve Tissue. Cardiology Research and Practice 2010.
129. Weska RF, Aimoli CG, Nogueira GM, Leirner AA, Maizato MJS, et al. (2010) Natural and Prosthetic Heart Valve Calcification: Morphology and Chemical Composition Characterization. Artificial Organs 34: 311-318.
130. Delogne C, Lawford PV, Habesch SM, Carolan VA (2007) Characterization of the calcification of cardiac valve bioprostheses by environmental scanning electron microscopy and vibrational spectroscopy. Journal of Microscopy 228: 62-77.
131. Cheng W-T, Liu M-T, Liu H-N, Lin S-Y (2005) Micro-Raman spectroscopy used to identify and grade human skin pilomatrixoma. Microscopy Research and Technique 68: 75-79.
132. Wong GL (1975) Target cells in bone for parathormone and calcitonin are different: enrichment for each cell type by sequential digestion of mouse calvaria and selective adhesion to polymeric surfaces. Proceedings of the National Academy of Sciences of the United States of America 72: 3167-3171.
133. Gruber HE, Ingram J, Zinchenko N, Hanley EN (2010) Practical histological methods for use with cultured cells Biotechnic & Histochemistry 84: 283-286.
134. Geladi P (1985) Linearization and scatter-correction for near-infrared reflectance spectra of meat. Applied spectroscopy 39: 491-500.
135. Hancewicz TM, Petty C (1995) Quantitative analysis of vitamin A using Fourier transform Raman spectroscopy. Spectrochimica Acta Part A: Molecular and Biomolecular Spectroscopy 51: 2193-2198.

136. Norgaard L, Saudland A, Wagner J, Nielsen JP, Munck L, et al. (2000) Interval Partial Least-Squares Regression (iPLS): A Comparative Chemometric Study with an Example from Near-Infrared Spectroscopy. Appl Spectrosc 54: 413-419.
137. Barragan Adjemian C (2006) Mechanism by which MLO-A5 Late Osteoblasts/Early Osteocytes Mineralize in Culture: Similarities with Mineralization of Lamellar Bone. Calcified tissue international 79: 340-353.
138. Starborg T (2008) Electron microscopy in cell-matrix research. Methods 45: 53-64.
139. Hodge AJ, Petruska JA (1963) Aspect of Protein Structure; Ramachandran GN, editor. New York: Academic Press.
140. Frushour BG, Koenig JL (1975) Raman scattering of collagen, gelatin, and elastin. Biopolymers 14: 379-391.
141. Rajamannan NM (2009) Calcific aortic stenosis: lessons learned from experimental and clinical studies. Arteriosclerosis, thrombosis, and vascular biology 29: 162-168.
142. Rodriguez KJ, Masters KS (2009) Regulation of valvular interstitial cell calcification by components of the extracellular matrix. Journal of Biomedical Materials Research Part A 90A: 1043-1053.
143. Walker GA, Masters KS, Shah DN, Anseth KS, Leinwand LA (2004) Valvular Myofibroblast Activation by Transforming Growth Factor-β. Circulation Research 95: 253-260.
144. Monzack EL, Masters KS (2011) Can Valvular Interstitial Cells Become True Osteoblasts? A Side-by-Side Comparison. The Journal of Heart Valve Disease 20: 449-463.
145. Aikawa E, Nahrendorf M, Sosnovik D, Lok VM, Jaffer FA, et al. (2007) Multimodality Molecular Imaging Identifies Proteolytic and Osteogenic Activities in Early Aortic Valve Disease. Circulation 115: 377-386.
146. Chen J-H, Simmons CA (2011) Cell–Matrix Interactions in the Pathobiology of Calcific Aortic Valve Disease. Circulation Research 108: 1510-1524.
147. Miller JD, Weiss RM, Heistad DD (2011) Calcific Aortic Valve Stenosis: Methods, Models, and Mechanisms. Circulation Research 108: 1392-1412.
148. Sappino AP (1990) Differentiation repertoire of fibroblastic cells: expression of cytoskeletal proteins as marker of phenotypic modulations. Laboratory Investigation 63: 144.

149. Monzack EL, Gu X, Masters KS (2009) Efficacy of simvastatin treatment of valvular interstitial cells varies with the extracellular environment. Arteriosclerosis, thrombosis, and vascular biology 29: 246-253.

150. Rocha R (2007) Identification of calcifications in cardiac valves by near infrared Raman spectroscopy. Photomedicine and laser surgery 25: 287-290.

151. Keelan PC, Bielak LF, Ashai K, Jamjoum LS, Denktas AE, et al. (2001) Long-term prognostic value of coronary calcification detected by electron-beam computed tomography in patients undergoing coronary angiography. Circulation 104: 412-417.

152. Hjortnaes J, New SEP, Aikawa E (2013) Visualizing novel concepts of cardiovascular calcification. Trends in Cardiovascular Medicine 23: 71-79.

153. Rennenberg R, Kessels A, Schurgers L, Van Engelshoven J, De Leeuw P, et al. (2009) Vascular calcifications as a marker of increased cardiovascular risk: a meta-analysis. Vascular health and risk management 5: 185.

154. Sage AP, Tintut Y, Demer LL (2010) Regulatory mechanisms in vascular calcification. Nature Reviews Cardiology 7: 528-536.

155. Lusis AJ (2000) Atherosclerosis. Nature 407: 233-241.

156. Watson KE, Parhami F, Shin V, Demer LL (1998) Fibronectin and Collagen I Matrixes Promote Calcification of Vascular Cells in Vitro, Whereas Collagen IV Matrix Is Inhibitory. Arteriosclerosis, thrombosis, and vascular biology 18: 1964-1971.

157. Rekhter MD (1999) Collagen synthesis in atherosclerosis: too much and not enough. Cardiovascular Research 41: 376-384.

158. Rekhter M, Zhang K, Narayanan A, Phan S, Schork M, et al. (1993) Type I collagen gene expression in human atherosclerosis. Localization to specific plaque regions. The American journal of pathology 143: 1634.

159. Adiguzel E, Ahmad PJ, Franco C, Bendeck MP (2009) Collagens in the progression and complications of atherosclerosis. Vascular Medicine 14: 73-89.

160. Stary HC, Chandler AB, Dinsmore RE, Fuster V, Glagov S, et al. (1995) A definition of advanced types of atherosclerotic lesions and a histological classification of atherosclerosis A report from the Committee on Vascular Lesions of the Council on Arteriosclerosis, American Heart Association. Arteriosclerosis, thrombosis, and vascular biology 15: 1512-1531.

161. Vattikuti R, Towler DA (2004) Osteogenic regulation of vascular calcification: an early perspective. American Journal of Physiology - Endocrinology And Metabolism 286: E686-E696.

162. Jeziorska M, McCollum C, Woolley D (1998) Observations on bone formation and remodelling in advanced atherosclerotic lesions of human carotid arteries. Virchows Archiv 433: 559-565.

163. Hunt JL, Fairman R, Mitchell ME, Carpenter JP, Golden M, et al. (2002) Bone formation in carotid plaques a clinicopathological study. stroke 33: 1214-1219.

164. Cowles E, DeRome M, Pastizzo G, Brailey L, Gronowicz G (1998) Mineralization and the expression of matrix proteins during in vivo bone development. Calcified tissue international 62: 74-82.

165. Carden A, Rajachar RM, Morris MD, Kohn DH (2003) Ultrastructural Changes Accompanying the Mechanical Deformation of Bone Tissue: A Raman Imaging Study. Calcified tissue international 72: 166-175.

166. Newcomb WL, Hope WW, Schmelzer TM, Heath JJ, Norton HJ, et al. (2009) Comparison of blood vessel sealing among new electrosurgical and ultrasonic devices. Surgical Endoscopy and Other Interventional Techniques 23: 90-96.

167. Sigel B, Dunn MR (1965) MECHANISM OF BLOOD VESSEL CLOSURE BY HIGH FREQUENCY ELECTROCOAGULATION. Surgery Gynecology and Obstetrics with International Abstracts of Surgery 121: 823-&.

168. Winter H, Holmer C, Buhr HJ, Lindner G, Lauster R, et al. (2010) Pilot study of bipolar radiofrequency-induced anastomotic thermofusion-exploration of therapy parameters ex vivo. Int J Colorectal Dis 25: 129-133.

169. Floume T, Syms RR, Darzi AW, Hanna GB (2008) Real-time optical monitoring of radio-frequency tissue fusion by continuous wave transmission spectroscopy. J Biomed Opt 13: 064006.

170. Floume T, Syms RR, Darzi AW, Hanna GB (2010) Optical, thermal, and electrical monitoring of radio-frequency tissue modification. J Biomed Opt 15: 018003.

171. Hyman N (2007) Anastomotic leaks after intestinal anastomosis: it's later than you think. Annals of surgery 245: 254.

172. Foschi D, Cellerino P, Corsi F, Taidelli T, Morandi E, et al. (2002) The mechanisms of blood vessel closure in humans by the application of ultrasonic energy. Surgical Endoscopy and Other Interventional Techniques 16: 814-819.

173. Lieber CA, Mahadevan-Jansen A (2007) Development of a handheld Raman microspectrometer for clinical dermatologic applications. Optics Express 15: 11874-11882.

174. Patil CA, Bosschaart N, Keller MD, van Leeuwen TG, Mahadevan-Jansen A (2008) Combined Raman spectroscopy and optical coherence tomography device for tissue characterization. Optics Letters 33: 1135-1137.

175. Jhan J-W, Chang W-T, Chen H-C, Lee Y-T, Wu M-F, et al. (2008) Integrated multiple multi-photon imaging and Raman spectroscopy for characterizing structure-constituent correlation of tissues. Optics Express 16: 16431-16441.

176. Srinivasan S, Schulmerich M, Cole JH, Dooley KA, Kreider JM, et al. (2008) Image-guided Raman spectroscopic recovery of canine cortical bone contrast in situ. Optics Express 16: 12190-12200.

177. Moreira LM, Silveira L, Jr., Santos FV, Lyon JP, Rocha R, et al. (2008) Raman spectroscopy: A powerful technique for biochemical analysis and diagnosis. Spectroscopy-an International Journal 22: 1-19.

178. Thomas GJ (1999) Raman spectroscopy of protein and nucleic acid assemblies. Annual Review of Biophysics and Biomolecular Structure 28: 1-+.

179. Lippert JL, Tyminski D, Desmeules PJ (1976) DETERMINATION OF SECONDARY STRUCTURE OF PROTEINS BY LASER RAMAN-SPECTROSCOPY. Journal of the American Chemical Society 98: 7075-7080.

180. Alimova A, Chakraverty R, Muthukattil R, Elder S, Katz A, et al. (2009) In vivo molecular evaluation of guinea pig skin incisions healing after surgical suture and laser tissue welding using Raman spectroscopy. Journal of Photochemistry and Photobiology B-Biology 96: 178-183.

181. Dong RX, Yan XL, Pang XF, Liu SG (2004) Temperature-dependent Raman spectra of collagen and DNA. Spectrochimica Acta Part a-Molecular and Biomolecular Spectroscopy 60: 557-561.

182. Bergner N, Krafft C, Geiger KD, Kirsch M, Schackert G, et al. (2012) Unsupervised unmixing of Raman microspectroscopic images for morphochemical analysis of non-dried brain tumor specimens. Analytical and Bioanalytical Chemistry 403: 719-725.

183. Gentleman E, Swain RJ, Evans ND, Boonrungsiman S, Jell G, et al. (2009) Comparative materials differences revealed in engineered bone as a function of cell-specific differentiation. Nature Materials 8: 763-770.

184. Lieber CA, Mahadevan-Jansen A (2003) Automated method for subtraction of fluorescence from biological Raman spectra. Applied Spectroscopy 57: 1363-1367.

185. Geladi P, Macdougall D, Martens H (1985) LINEARIZATION AND SCATTER-CORRECTION FOR NEAR-INFRARED REFLECTANCE SPECTRA OF MEAT. Applied Spectroscopy 39: 491-500.

186. Hancewicz TM, Petty C (1995) Quantitative analysis of vitamin A using Fourier transform Raman spectroscopy. Spectrochimica Acta Part a-Molecular and Biomolecular Spectroscopy 51: 2193-2198.

187. Shobhit A, Hadjievangelou N, Su L, Kudo H, Goldin RD, et al. (2013) Radiofrequency induced small bowel thermofusion: An ex vivo study of intestinal seal adequacy using mechanical and imaging modalities. Surg Endosc Accepted.

188. Frushour BG, Koenig JL (1975) RAMAN-SCATTERING OF COLLAGEN, GELATIN, AND ELASTIN. Biopolymers 14: 379-391.

189. Hedegaard M, Matthaeus C, Hassing S, Krafft C, Diem M, et al. (2011) Spectral unmixing and clustering algorithms for assessment of single cells by Raman microscopic imaging. Theoretical Chemistry Accounts 130: 1249-1260.

190. Salameh JR, Schwartz JH, Hildebrandt DA (2006) Can LigaSure seal and divide the small bowel? American Journal of Surgery 191: 791-793.

191. Shields CA, Schechter DA, Tetzlaff P, Baily AL, Dycus S, et al. (2004) Method for creating ideal tissue fusion in soft-tissue structures using radio frequency (RF) energy. Surg Technol Int 13: 49-55.

192. Tarnowski CP, Stewart S, Holder K, Campbell-Clark L, Thoma RJ, et al. (2003) Effects of treatment protocols and subcutaneous implantation on bovine pericardium: a Raman spectroscopy study. J Biomed Opt 8: 179-184.

193. Stone N, Kendall C, Smith J, Crow P, Barr H (2004) Raman spectroscopy for identification of epithelial cancers. Faraday Discussions 126: 141-157.

194. Lau DP, Huang ZW, Lui H, Anderson DW, Berean K, et al. (2005) Raman spectroscopy for optical diagnosis in the larynx: Preliminary findings. Lasers Surg Med 37: 192-200.

195. Hanlon EB, Manoharan R, Koo TW, Shafer KE, Motz JT, et al. (2000) Prospects for in vivo Raman spectroscopy. Physics in Medicine and Biology 45: R1-R59.

196. Kaminaka S, Ito T, Yamazaki H, Kohda E, Hamaguchi H (2002) Near-infrared multichannel Raman spectroscopy toward real-time in vivo cancer diagnosis. Journal of Raman Spectroscopy 33: 498-502.

197. Shim MG, Song L, Marcon NE, Wilson BC (2000) In vivo near-infrared Raman spectroscopy: Demonstration of feasibility during clinical gastrointestinal endoscopy. Photochem Photobiol 72: 146-150.

198. Haka AS, Volynskaya Z, Gardecki JA, Nazemi J, Lyons J, et al. (2006) In vivo Margin Assessment during Partial Mastectomy Breast Surgery Using Raman Spectroscopy[?Q1: Running head: Raman Margin Assessment at Partial Mastectomy. Short title OK?Q1]. Cancer Research 66: 3317-3322.

199. Pascut FC, Goh HT, George V, Denning C, Notingher I (2011) Toward label-free Raman-activated cell sorting of cardiomyocytes derived from human embryonic stem cells. Journal of Biomedical Optics 16: 045002-045002-045004.

200. Schulze HG, Konorov SO, Caron NJ, Piret JM, Blades MW, et al. (2010) Assessing differentiation status of human embryonic stem cells noninvasively using Raman microspectroscopy. Analytical Chemistry 82: 5020-5027.

201. Chan JW, Lieu DK, Huser T, Li RA (2009) Label-Free Separation of Human Embryonic Stem Cells and Their Cardiac Derivatives Using Raman Spectroscopy. Analytical Chemistry 81: 1324-1331.

202. Ramm Sander P, Hau P, Koch S, Schütze K, Bogdahn U, et al. (2013) Stem cell metabolic and spectroscopic profiling. Trends in Biotechnology 31: 204-213.

203. Pilarczyk M, Czamara K, Baranska M, Natorska J, Kapusta P, et al. (2013) Calcification of aortic human valves studied in situ by Raman microimaging: following mineralization from small grains to big deposits. Journal of Raman spectroscopy 44: 1222-1229.

204. Azevedo P, Pereira R, Guilherme L (2012) Understanding rheumatic fever. Rheumatology International 32: 1113-1120.

205. Antonakos A, Liarokapis E, Leventouri T (2007) Micro-Raman and FTIR studies of synthetic and natural apatites. Biomaterials 28: 3043-3054.

206. Raz S, Testeniere O, Hecker A, Weiner S, Luquet G (2002) Stable Amorphous Calcium Carbonate Is the Main Component of the Calcium Storage Structures of the Crustacean Orchestia cavimana. The Biological Bulletin 203: 269-274.

207. Addadi L, Raz S, Weiner S (2003) Taking Advantage of Disorder: Amorphous Calcium Carbonate and Its Roles in Biomineralization. Advanced Materials 15: 959-970.